1994

Unsteady boundary-layer separation on a pitching airfoil

Michael P. Johnson
Lehigh University

AUTHOR:

Johnson, Michael P.

TITLE:

Unsteady Boundary-Layer Separation on a Pitching Airfoil

DATE: May 29, 1994

UNSTEADY BOUNDARY-LAYER SEPARATION ON A PITCHING AIRFOIL

by

Michael P. Johnson

A Thesis

Presented to the Graduate and Research Committee

of Lehigh University

in Candidacy for the Degree of

Master of Science

in

Mechanical Engineering

Lehigh University

May 1994

CERTIFICATE OF APPROVAL

This thesis is accepted and approved in partial fulfillment of the requirements for the degree of Master of Science.

May 12, 1994
Date

Professor J.D.A. Walker
Thesis Advisor

Professor Robert P. Wei
Chairman of Department

ACKNOWLEDGEMENTS

I wish to extend special thanks to the following people: Dr. J.D.A. Walker, my thesis advisor, for his guidance and support; Dr. A.T. Degani for his computational work on an airfoil at a constant angle of attack; Dr. V.J. Peridier for her vortex-induced boundary-layer separation study; and Dr. David J. Wells, my undergraduate advisor, for his genuine interest in my educational and professional careers. Also, I wish to acknowledge Dr. William Yurkewicz, my high school physics teacher, for his never-ending enthusiasm and quintessential teaching.

Finally, my research would not have been possible without the financial support from the Department of Mechanical Engineering and Applied Mechanics and the Graduate School of Lehigh University.

TABLE OF CONTENTS

TABLE OF FIGURES

ABSTRACT

This research is a theoretical and computational study of unsteady boundary-layer separation from a two-dimensional thin airfoil immersed in a uniform flow stream when the angle of attack is varied as a function of time. The flow is considered to be high speed in the sense that the Reynolds number is large; limiting situations corresponding to the case $\mathrm{Re} \to \infty$ are considered. As the angle of attack is suddenly changed beyond a critical angle, unsteady processes initiate in the boundary layer in the leading edge region of the airfoil that eventually lead to a phenomenon known as dynamic stall. As these processes develop, a recirculating eddy is first formed in the boundary layer , and soon the flow near the top surface of the airfoil is focused into a region that progressively narrows in the streamwise direction. This leads to the eventual development of a separation singularity in the solution of the boundary-layer equations and a strong viscous-inviscid interaction wherein the boundary layer erupts into the outer inviscid flow. Computational results are obtained for the angle of attack increasing linearly with time, and these illustrate the events leading up to the ejection of boundary-layer vorticity into the upstream external flow at a finite time. Separation develops as a thin "spike" extending from the upper surface of the airfoil on the upstream side of the recirculating zone. The time required to reach separation, starting from an altitude of zero incidence, is evaluated as a function of pitching rate. The effect of reversing the pitching rate is considered; it is found that under certain circumstances, leading edge separation can be delayed.

CHAPTER 1
INTRODUCTION

1.1 SIGNIFICANT ISSUES AND OBJECTIVES

As an airfoil (such as an airplane wing) is pitched up from zero incidence to some finite angle of attack in a uniform stream, there is virtually a linear increase in aerodynamic lift. However, if the airfoil is pitched to a large enough angle with respect to the oncoming mainstream, the lift levels off and beyond this stage, any increase in the angle of attack leads to airfoil stall (Wegener 1991, p.111). Stall occurs when the lift force that is mainly produced by the airfoil suddenly decreases as a result of the flow detaching (separating) from the upper surface of the airfoil.

The events associated with such phenomena are intriguing and continue to attract intense interest. "Dynamic stall is a term describing a sequence of events that develop in the flow field near an airfoil undergoing a pitching motion, thereby increasing the effective angle of attack of the oncoming stream" (Doligalski et al. 1994, p.589). As the angle of attack is increased beyond a critical angle (Werle & Davis 1972), an unsteady boundary-layer separation process develops which leads to the development of a primary dynamic stall vortex on the upper surface of the airfoil. When the airfoil is pitched rapidly beyond its static stall angle, this vortex is torn from the upper surface resulting in full stall. There is, however, a potential benefit associated with having the primary dynamic stall vortex reside above the airfoil, and this is the substantial increase in aerodynamic lift during the short time interval

when the vortex is near the surface of the airfoil. Control of this entire unsteady process may possibly improve the maneuverability and performance of certain aircraft, such as mobile attack planes. A challenging task is to find a way to keep the vortex attached to the airfoil during an entire maneuver (Doligalski et al, 1994).

The main disadvantage associated with the presence of the primary stall vortex occurs when the vortex detaches from the airfoil and thereby initiates full stall. This occurs when the vortex interacts with the boundary layer on the surface of the airfoil. The result of this process is an abrupt decrease in lift with a sudden pitching moment. This event can lead to control problems as well as significant stresses on the airframe. The aircraft may then plummet if its weight exceeds the now dangerously decreased lift force.

Dynamic stall has been studied for decades because of its importance in helicopter flight. Generally, the rotor blades experience the influence of unsteady flow processes. For instance, when a helicopter is in forward flight, the blades traveling in the opposite direction of flight (the retreating blades) experience a relatively lower-speed external flow in contrast to the advancing blades (those moving in the direction of flight). To achieve the lift that occurs on the advancing blades, the retreating blades are pitched to a relatively higher angle of attack (Doligalski et al, 1994). When dynamic stall occurs near helicopter blades, the consequences are dangerous and potentially disastrous (McCroskey, 1982). Therefore, the design goal in the rotocraft industry is usually to try to suppress the initial formation of the primary stall vortex.

To understand the development (as well as the possible control) of dynamic stall, it is necessary to investigate the unsteady flow structure around

an airfoil as its angle of attack is continuously changing with time. The main objective of this thesis is to determine how unsteady boundary-layer separation near the leading edge of the airfoil that leads to dynamic stall takes place in a high Reynolds number flow. A further objective is to find a way to control, prevent, or at least delay the onset of the unsteady viscous-inviscid interaction that occurs with boundary-layer separation. The effect of reversing the pitching rate of the airfoil is investigated in this study.

Past research and experiments indicate that the critical events of unsteady separation take place in the leading edge region of an airfoil for flows at high Reynolds numbers. A possible explanation is that the upper side of the airfoil in the nose region experiences an increasingly adverse pressure gradient as the angle of attack increases (Doligalski et al, 1994), while the point of maximum velocity around the airfoil moves closer to the leading edge as described in chapter 2.

The beginning of the dynamic stall process occurs deep within a thin, viscous boundary layer surrounding the airfoil. Therefore, it is extremely difficult to view the initial stages of the relevant events through experimental means. At the same time, experiments are useful in revealing the later stages of the process. In a theoretical study, it is possible to closely examine the details of the boundary-layer development in the leading-edge region and to isolate the onset of separation. The onset of the eventual viscous-inviscid interaction that occurs with boundary-layer separation is characterized by a rapid local thickening of the boundary layer; the process culminates with the ejection of vorticity into the outer inviscid region above the airfoil.

In summary, the main objectives of this study are as follows: (1) to study

the boundary layer on a thin airfoil at a variable angle of attack in an incompressible flow field in the limit of high Reynolds number; (2) to calculate the solution of the boundary-layer problem numerically and determine the time when separation occurs; and (3) to study the influence of varying the pitching rate of the airfoil as a possible control measure for preventing or delaying boundary-layer separation.

1.2 GOVERNING EQUATIONS

The general equations used in this study are outlined in this section. All equations are written in nondimensional form. The vector form of the Navier-Stokes equations for incompressible flow is

$$\frac{\partial \vec{v}}{\partial t} + \vec{\nabla}(\frac{1}{2}\vec{v} \bullet \vec{v}) - \vec{v} \times (\vec{\nabla} \times \vec{v}) = -\vec{\nabla}p - \frac{1}{Re}\vec{\nabla} \times (\vec{\nabla} \times \vec{v}), \qquad (1.1)$$

and the associated continuity equation is

$$\vec{\nabla} \bullet \vec{v} = 0. \qquad (1.2)$$

Here, the Reynolds number is defined by

$$Re = \frac{U_0 L_c}{\nu}, \qquad (1.3)$$

where U_0 is a representative fluid speed, L_c is a characteristic length of the body immersed in the flow, and ν is the kinematic viscosity of the fluid. The Reynolds number is indicative of the relative importance of inertial to viscous forces in equation (1.1). The nondimensional velocity vector is denoted by $\vec{v}$.

The coordinate system is dimensionless with respect to L_c, the time t with respect to L_c/U_0, and the dynamic pressure p with respect to $\frac{1}{2}\rho {U_0}^2$, where ρ is the fluid density.

The no-slip and solid boundary conditions constitute the boundary conditions associated with this system,

$$\vec{v} = 0, \tag{1.4}$$

which must be satisfied at the body surface.

In principle, the study of high Reynolds number flows involves a two stage process involving a sequential solution of the inviscid and boundary-layer equations. In the limit Re$\rightarrow\infty$, the viscous terms are negligible in the momentum equations (1.1) and the Euler equations for inviscid flow are obtained according to

$$\frac{\partial \vec{v}}{\partial t} + \vec{\nabla}(\frac{1}{2}\,\vec{v} \bullet \vec{v}) - \vec{v} \times (\vec{\nabla} \times \vec{v}) = -\vec{\nabla}p. \tag{1.5}$$

However, solutions of the Euler equations cannot satisfy the no-slip condition at the surface. Without the presence of the viscous term in equations (1.5), fewer boundary conditions may be enforced at the surface than for the full viscous equations (1.1), and experience indicates the boundary condition to enforce in the Euler equations is that the flow velocity normal to a solid surface should vanish (Panton 1984, p.432). Let x and Y be streamwise and normal dimensionless coordinates, respectively, in a two-dimensional Cartesian system fixed at some point on the body; the condition of vanishing normal velocity is then

$$V=0 \ \text{ at } \ Y=0. \tag{1.6}$$

In general a solution of the Euler equations produces a slip velocity along the surface denoted here by

$$U \to U_\infty(x,t) \quad \text{as} \quad Y \to 0. \tag{1.7}$$

Near the surface, the viscous shear stresses in equation (1.1) become important in the boundary layer. No matter how large Re becomes, a thin boundary layer must exist to satisfy the no-slip condition; this corrects the inviscid solution at a solid surface (Panton 1984, p.439). The boundary-layer thickness is $O(Re^{-1\backslash 2})$ and both y and V are small here. Therefore, scaled variables are introduced in order to magnify the small spatial and velocity scales in the direction normal to the surface, viz.

$$y = Re^{1/2}\, Y, \quad v = Re^{1/2}\, V. \tag{1.8}$$

It is easily shown from equations (1.1) and (1.2) that the general form of the two-dimensional streamwise boundary-layer equations in Eulerian coordinates is

$$\frac{\partial u}{\partial t} + u\frac{\partial u}{\partial x} + v\frac{\partial u}{\partial y} = -\frac{\partial p}{\partial x} + \frac{\partial^2 u}{\partial y^2}, \tag{1.9}$$

$$\frac{\partial u}{\partial x} + \frac{\partial v}{\partial y} = 0, \tag{1.10}$$

where u and v are the velocities in the x and y directions, respectively. The boundary conditions are zero flow along or normal to the surface according to

$$u = v = 0 \quad \text{at} \quad y=0. \tag{1.11}$$

Due to their complementary relationship, the inviscid and boundary-layer solutions must be matched as $Y \to 0$; and matching to the mainstream flow requires that

$$\lim_{y \to \infty} u(x,y,t) = U_\infty(x,t). \tag{1.12}$$

In summary, the conventional Eulerian formulation of the boundary-layer problem is described by equations (1.9) through (1.12).

An expression for the pressure gradient $\partial p/\partial x$ is obtained by taking the limit $y \to \infty$ in the boundary-layer equation (1.9). In this limit, the velocity $u(x,y,t)$ is given by equation (1.12), while the derivative terms with respect to y have

$$\frac{\partial u}{\partial y} \to 0, \quad \frac{\partial^2 u}{\partial y^2} \to 0. \tag{1.13}$$

These conditions indicate that the viscous stresses must vanish as the inviscid region is approached. Thus the pressure gradient in equation (1.9) can be expressed in the alternate form

$$-\frac{\partial p}{\partial x} = \frac{\partial U_\infty}{\partial t} + U_\infty \frac{\partial U_\infty}{\partial x}. \tag{1.14}$$

In the present study, the Eulerian formulation was used to start the numerical computations at the initiation of motion at t=0 because it is generally the most efficient method of evaluating the boundary-layer development when the flow solution is relatively smooth. However, in regions where the imposed pressure gradient is adverse, boundary-layer separation eventually initiates and conventional numerical algorithms for the Eulerian formulation experience severe problems in obtaining good numerical resolution and convergence. When this occurred in the present formulation, the Eulerian integrations were terminated at some time, say $t=t_{end}$. Then, at a chosen time

$t=t_0 < t_{end}$, an integration in Lagrangian coordinates was started with initial conditions taken from the results of the Eulerian calculation at $t=t_0$. The Lagrangian approach computes individual fluid particle positions, x, and their streamwise (tangential) velocities, u, as functions of time. The boundary-layer equations in Lagrangian variables are derived in Appendix B and are

$$\frac{\partial u}{\partial t} = \frac{\partial U_\infty}{\partial x} + U_\infty \frac{\partial U_\infty}{\partial x} + \left(\frac{\partial x}{\partial \xi}\frac{\partial}{\partial \eta} - \frac{\partial x}{\partial \eta}\frac{\partial}{\partial \xi}\right)^2 u, \tag{1.15}$$

$$\frac{\partial x}{\partial t} = u, \tag{1.16}$$

where x and u are the dependent variables with

$$x = x(\xi,\eta,t), \quad u = u(\xi,\eta,t). \tag{1.17}$$

The independent variables, ξ and η, are defined as the initial positions of the fluid particles at some time t_0 when the Lagrangian method is started, viz.

$$x(\xi,\eta,t) = \xi, \quad y(\xi,\eta,t) = \eta \quad \text{at } t=t_0. \tag{1.18}$$

The initial streamwise velocities of the initial particle positions are defined by

$$u = u(\xi,\eta,t) \quad \text{at} \quad t=t_0. \tag{1.19}$$

The boundary conditions for equation (1.15) are

$$u(\xi,0,t) = 0, \tag{1.20}$$

$$\lim_{\eta\to\infty} u(\xi,\eta,t) = U_\infty(x,t), \tag{1.21}$$

where U_∞ is the external inviscid solution.

For times $t > t_0$ as the boundary layer approaches separation, the Lagrangian method has several advantages over the Eulerian formulation. The

main advantage is that the streamwise particle positions, x, and corresponding tangential velocities, u, appear in the boundary-layer equations and the normal velocities, v, and normal positions, y, do not. In general, the Eulerian procedure breaks down as the unsteady boundary layer approaches separation because v and y become large. On the contrary, x and u remain bounded even as boundary-layer separation occurs and a singularity develops in the solution of the boundary-layer equations (Peridier 1989). The convergence and resolution advantages of the Lagrangian procedure are achieved at a price of increased computational time. The particle positions are functions of time and must be found by integration at each time step. However, the advantage of using both schemes is evident; the relatively easier implemented Eulerian program starts the numerical calculations and the Lagrangian program completes them.

Because equations (1.9) and (1.15) are similar in form, the same numerical schemes are used to solve both equations for the dependent variables. These algorithms are described in Appendix A.

1.3 BACKGROUND AND PAST RESEARCH

In this study, the boundary layer in the nose region of a two-dimensional airfoil is considered. Since the flow is assumed two-dimensional, quantities such as the outer mainstream velocity, streamfunction and pressure distribution are identical at any cross-section along the span of the airfoil. It is well known that the parabola can be used to represent the nose region of a

wide variety of thin airfoils and, consequently, a number of airfoils of otherwise different shapes may be considered (Wegener 1991).

Much current research is concerned with identifying the basic physical processes of flow separation that occur on an airfoil in motion. The processes of separation are believed to initiate in the leading edge region for flows with high Reynolds numbers.

Years ago, Werle and Davis (1972) showed that a steady boundary-layer solution for flow past a parabola is not possible beyond a small critical angle of attack. Beyond this critical value, a Goldstein singularity occurs in the solution of the steady boundary-layer problem. In addition, it is expected that starting from some initial state, the unsteady boundary-layer solution will start to develop strong outflows and an unsteady separation singularity; this is a direct consequence of imposing the external pressure gradient from the inviscid solution on the boundary-layer flow for an indefinite period of time.

The main intent is to determine the circumstances under which boundary-layer separation occurs near the leading edge of the airfoil. As the airfoil is pitched up to an angle of attack, the imposed pressure distribution dominates the boundary-layer development. In the cases where separation occurs, the strong interaction that eventually develops is essentially independent of the initial flow distribution near the surface (Peridier et al, 1991).

The solution of the unsteady boundary-layer equations is advanced forward in time numerically. It has been found that for many different constant angles of attack (Degani, Li and Walker, 1994), a small recirculating bubble develops on the upper surface of the parabola. The existence of this recirculating flow indicates a zero vorticity line is now present in the flow and

at this point, one of the MRS (Moore, Rott & Sears) conditions that is necessary for separation to occur is satisfied (Peridier et al, 1991). Once the recirculating zone appears, it continues to grow in both the streamwise and normal directions. Then, finally, the boundary-layer flow rapidly starts to concentrate into a progressively thinning region on the upstream side of the thickening recirculating zone. Eventually, a narrow spike in displacement thickness forms signifying the onset of an eruption of vorticity from the boundary-layer.

Van Dommelen and Shen (1980, 1982) showed that a singularity does indeed develop at a finite time in the solution of the boundary-layer equations. Doligalski et al (1994, pp. 582-583) indicate that fluid particles above the surface somewhere along the zero vorticity line

> experience strong compression in the tangential direction and consequently become extremely elongated in a direction normal to the wall (on the boundary-layer scale); this has the effect of focussing the local boundary-layer vorticity into a narrow "spike" that moves abruptly and rapidly away from the surface. On the boundary-layer scale, the phenomenon appears as an explosively-growing spike in displacement thickness having a lateral thickness which approaches zero as $Re \to \infty$; on the scale of the external flow, the event appears as a sharply focussed concentration of vorticity near the surface that is about to knife into the mainstream.

This result is evident since an incompressible fluid near a wall subjected to severe compression in the streamwise direction must respond so that fluid particles near the surface elongate in the normal direction to conserve their volumes.

In the present study a conventional Eulerian formulation was used to start the numerical calculation until it encountered resolution and

convergence problems when the boundary-layer solution began to approach eruption. Beyond that point, the solution of the unsteady boundary-layer equations could only be computed forward in time all the way to the aforementioned singularity state by using a Lagrangian formulation (Doligalski et al, 1994). In this scheme, the solution for the spatial positions of individual fluid particles is evaluated, even in a separating boundary-layer. The solution of x and u remains relatively well behaved. However, a numerical resolution problem may develop if, after some period, the particles are swept out of a particular flow region; this gives rise to very large coefficients $\partial x/\partial \xi$ and $\partial x/\partial \eta$ in equation (1.15) as the momentum equation becomes increasingly stiff with time. This difficulty is eliminated here by periodically remeshing the flow field into an Eulerian grid; the calculations in the Lagrangian system are then restarted with the newly remeshed quantities as initial conditions. The remeshing feature allows for a stable numerical procedure to complete the boundary-layer solution up to the singularity. The complete Eulerian and Lagrangian formulations are derived in chapter 2.

1.4 VARIABLE VS. CONSTANT ANGLE OF ATTACK

Previous research on this problem was concerned with an airfoil impulsively pitched to a constant angle of attack (Degani et al, 1994). In this case the outer inviscid velocity U_∞ is not a function of time and the boundary layer is suddenly exposed to a steady external velocity field which is a function of distance along the contour of the airfoil. Figure 1.1 illustrates

the flow geometry at the leading edge region for an airfoil at a constant angle of attack. The scale of the boundary-layer is extremely exaggerated in figure 1.1 to show the streamline patterns near the airfoil's surface. The zero streamline connects to the lower surface of the airfoil at a stagnation point where the total flow velocity is zero; the flow divides about this stagnation point and moves along the airfoil on both sides of this point. At a constant angle of attack, this stagnation point remains stationary; it does not move along the surface of the airfoil.

The present research is concerned with a pitching airfoil, and now the external velocity distribution is unsteady so that $U_\infty = U_\infty(x,t)$. From equation (1.14), it is readily observed that the pressure gradient is unsteady as well. Figure 1.2 illustrates the streamline patterns as an airfoil is pitching upward. Figure 1.2(a) shows the general form of the zero streamline and the stagnation point for an airfoil at angle of attack α_a (compare this to figure 1.1). Figure 1.2(b) shows the streamlines of the same airfoil at a subsequent time at angle of attack $\alpha_b > \alpha_a$. The stagnation point has moved to a position further down the lower surface and the zero streamline near the surface in the boundary-layer has a different form as well. The moving stagnation point is a significant feature of a pitching airfoil. Overall, the streamlines approaching the airfoil are "steeper" for α_b than for α_a.

Finally, the form of the streamwise velocity u(x,y,t) used in the solution process is different for these two cases. For an airfoil at a constant angle of attack, the general Eulerian form may be written

$$u(x,y,t) = U_\infty(x) \cdot \frac{\partial \psi(x,y,t)}{\partial y}, \tag{1.22}$$

where ψ is the streamfunction. The term $\partial\psi/\partial y$ is normalized such that

$$\frac{\partial\psi}{\partial y} \to 1 \qquad \text{as } y \to \infty. \tag{1.23}$$

The streamwise velocity cannot be represented this way for a pitching airfoil because $U_\infty = U_\infty(x,t)$ and the stagnation point is in motion. It may be shown from (1.14) that the term

$$\frac{1}{U_\infty}\frac{\partial U_\infty}{\partial t} \tag{1.24}$$

results in the boundary-layer equations if a velocity representation of the form (1.22) is tried. This term will be indeterminate when $U_\infty = 0$. Therefore, the general representation of the velocity used here for a pitching airfoil is

$$u(x,y,t) = \frac{\partial\psi(x,y,t)}{\partial y}, \tag{1.25}$$

where

$$\frac{\partial\psi}{\partial y} \to U_\infty(x,t) \qquad \text{as } y \to \infty. \tag{1.26}$$

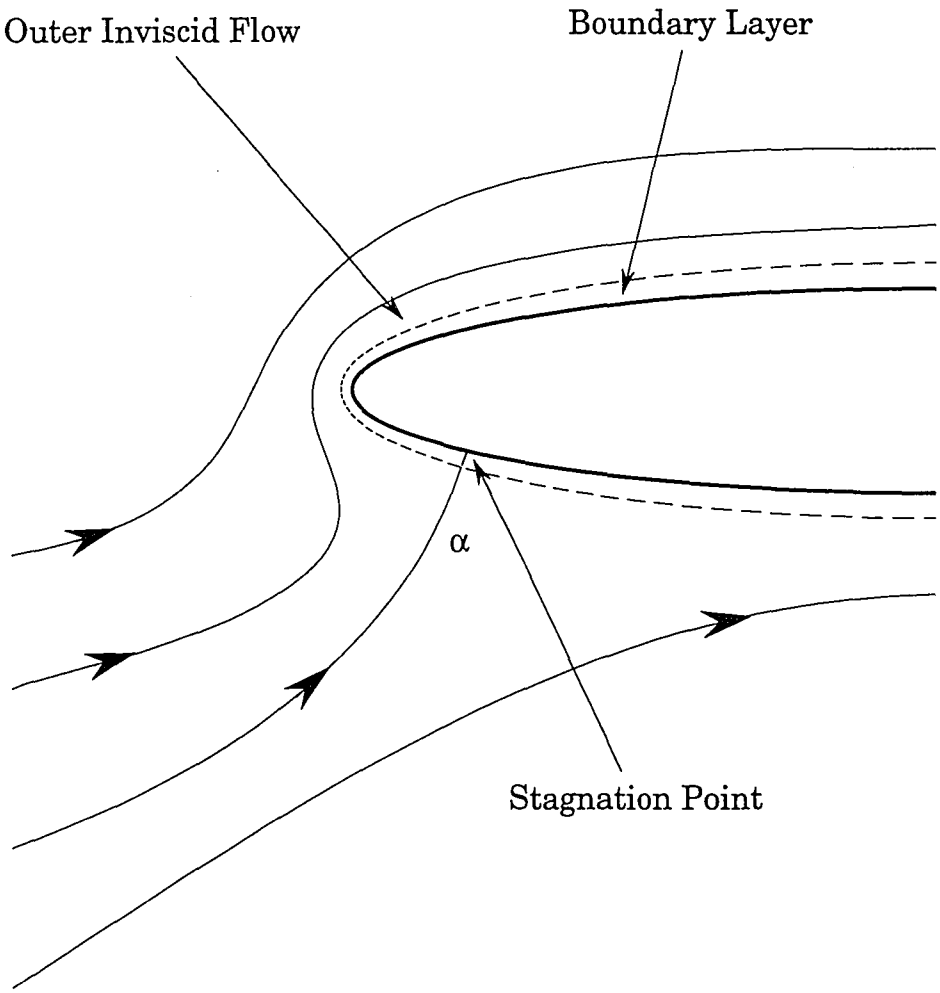

Figure 1.1- Geometry at leading edge region of an airfoil at a constant angle of attack α

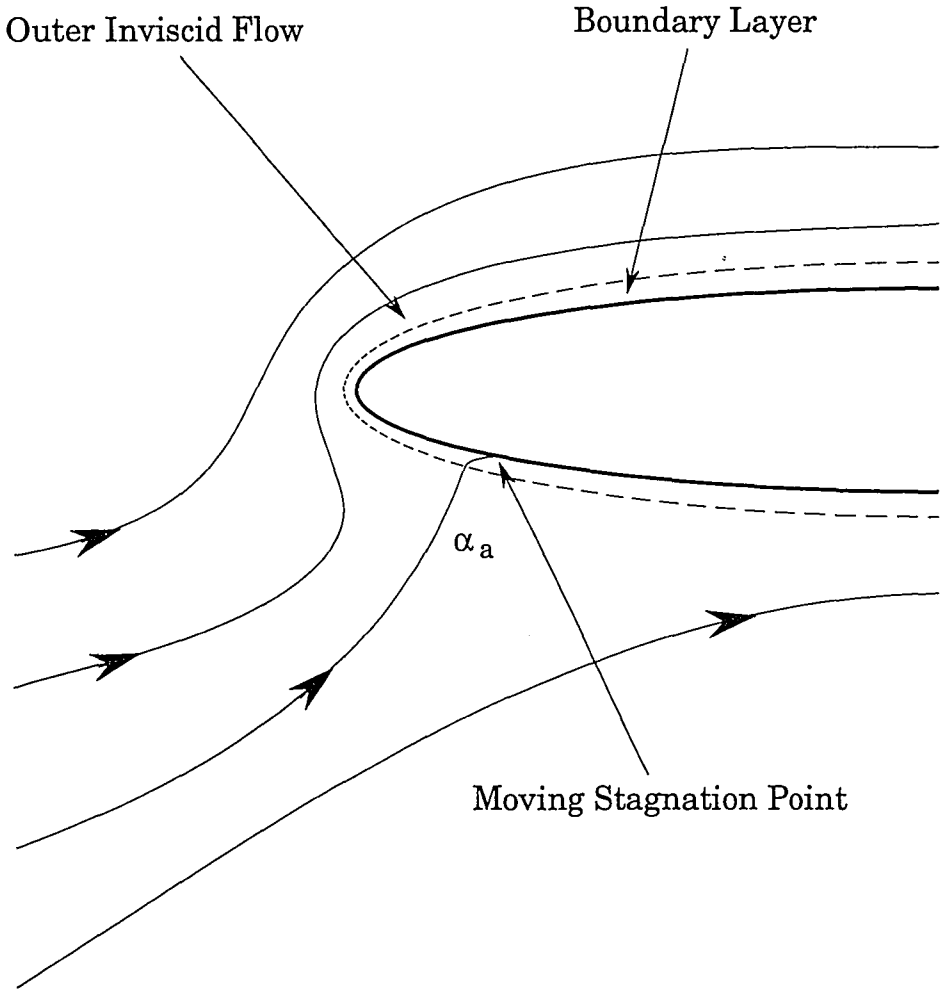

Figure 1.2 (a) - Instantaneous streamlines at leading edge region of a pitching airfoil at angle of attack α_a

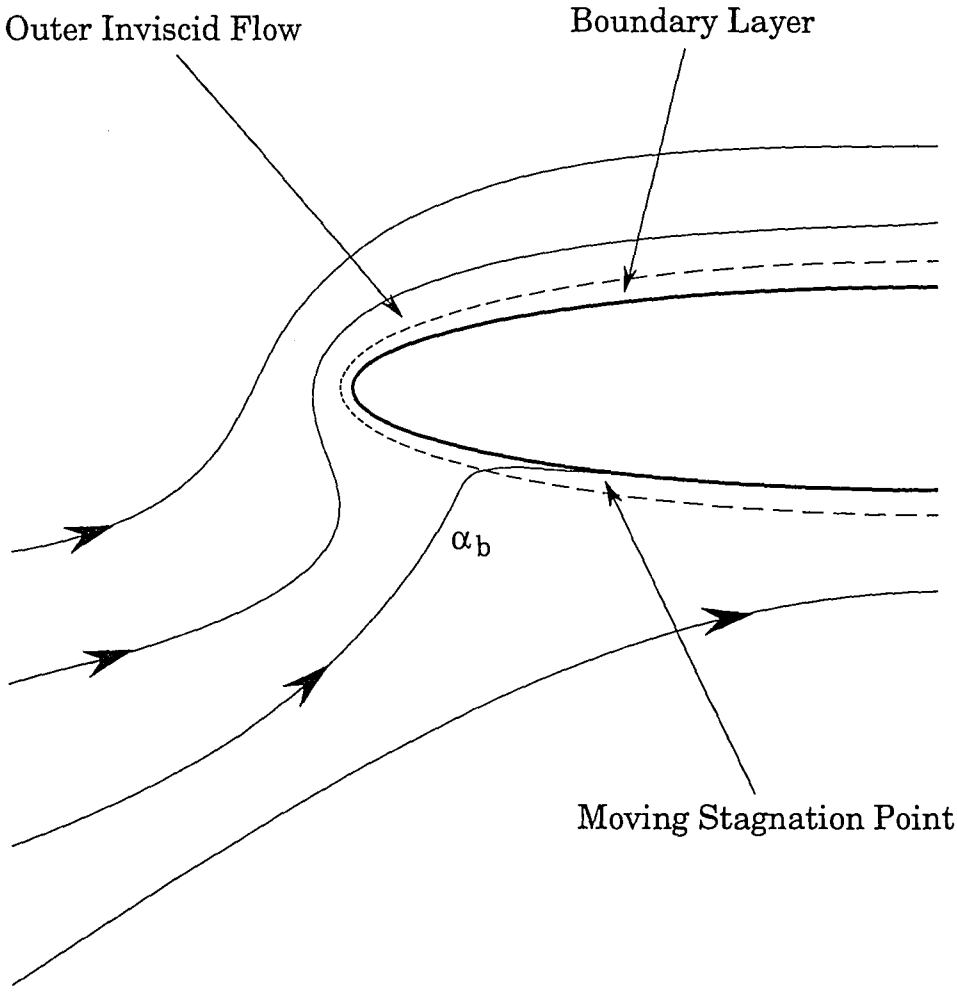

Figure 1.2 (b) - Instantaneous streamlines at leading edge region of a pitching airfoil at angle of attack α_b where $\alpha_b > \alpha_a$

CHAPTER 2
PROBLEM FORMULATION

2.1 INTRODUCTION

It is well known from thin airfoil theory (see, for example, Van Dyke (1975)), that any airfoil shape with a rounded nose may be represented as a parabola in the leading edge region. When a parabola is oriented at zero angle of attack to the oncoming freestream, the boundary layer in the leading nose region generally experiences a favorable pressure gradient as the external flow is accelerated away from a frontal stagnation point. However, when the parabola is pitched upward to a nonzero angle of attack, an adverse pressure gradient exists near the leading edge since the external velocity reaches a maximum somewhere on the upper surface; "This, coupled with the fact that all such viscous flows past a parabola approach a flat-plate solution infinitely far down stream, makes them ideal for boundary layer separation studies" (Werle & Davis, 1972).

2.2 THE MODEL PROBLEM

Consider the nose region of a parabola having the equation

$$y^2 = 2r_0 x. \tag{2.1}$$

As indicated in figure 2.1, the significance of the constant r_0 is that a circle of radius r_0 can be inscribed in the nose region of the parabola; for small x, the

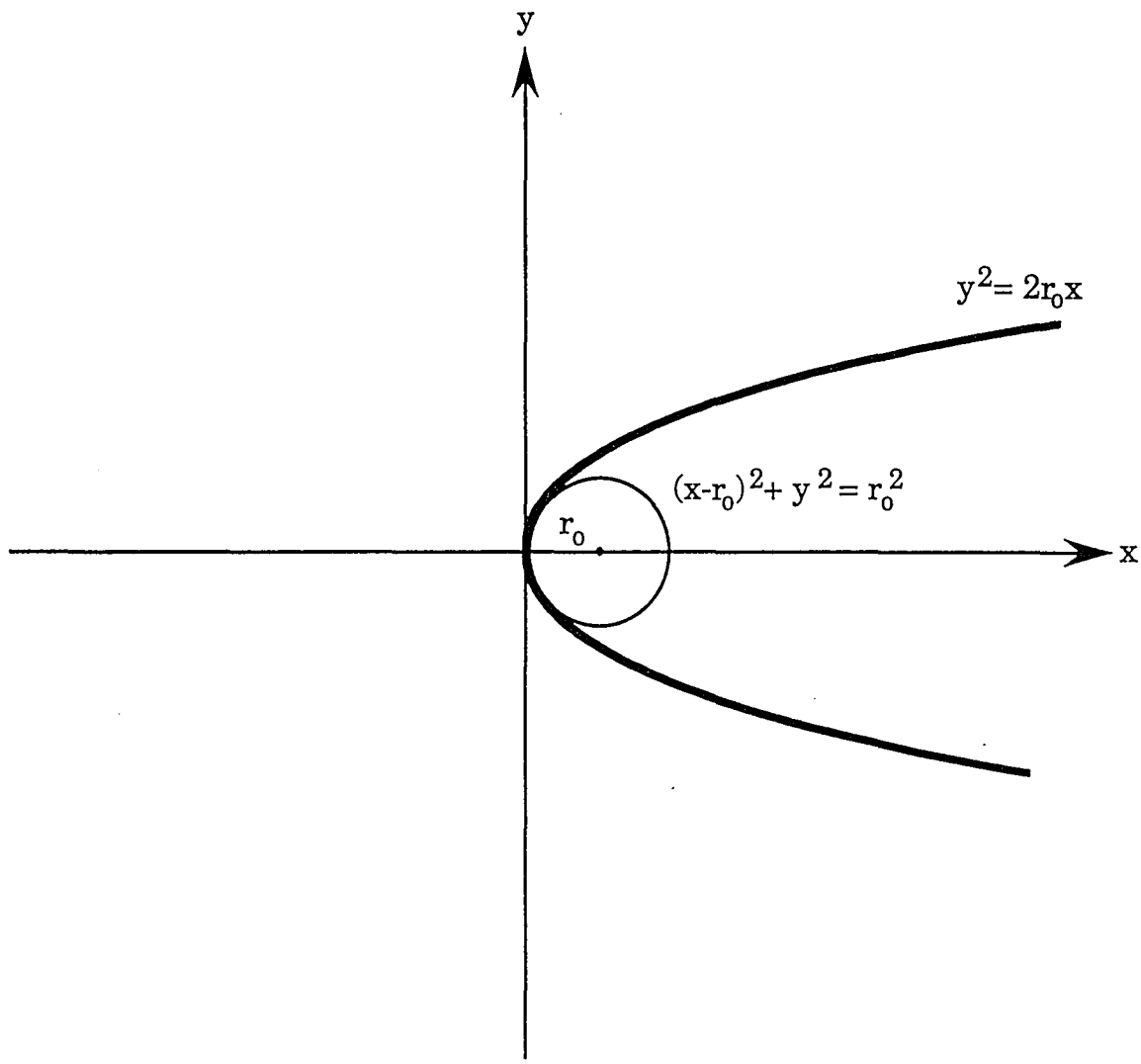

Figure 2.1 - Thin airfoil representation - circle of radius r_0 inscribed in the vertex region of a parabola

equation of the circle reduces to equation (2.1). Instead of Cartesian coordinates, the regions shown in figure 2.1 can be described in terms of parabolic coordinates. It is convenient to use complex variable theory to describe the transformation between the Cartesian coordinates (x,y) and the parabolic coordinates (ξ,η). The transformation is

$$z = \frac{1}{2}\zeta^2, \tag{2.2}$$

where z and ζ are complex variables defined by

$$z = x+iy \quad \text{and} \quad \zeta = \xi+i\eta. \tag{2.3}$$

Figure 2.2 shows the domain in terms of parabolic coordinates where $+\xi$ and $-\xi$ denote the upper and lower planes of the parabolas, respectively. It is evident that lines of constant η are confocal parabolas that open to the right with foci at the origin; and similarly, curves of constant ξ are confocal parabolas opening to the left with foci at the origin. Clearly, any point in the x,y plane can be described uniquely by parabolic coordinates (ξ,η).

In the present study, it is convenient to use a transformation that will map the parabola with nose radius r_0 to the ξ axis so that the vertex is at ξ=0 in the (ξ,η) plane; the region exterior to the parabola is to be described by orthogonal curvilinear coordinates. The transformation which accomplishes this is

$$z = \frac{r_0}{2} + \frac{1}{2}(\zeta+i\sqrt{r_0})^2. \tag{2.4}$$

This transformation defines a parabolic coordinate system for which the surface of the parabola is defined by η=0; as shown in figure 2.3, the η contours

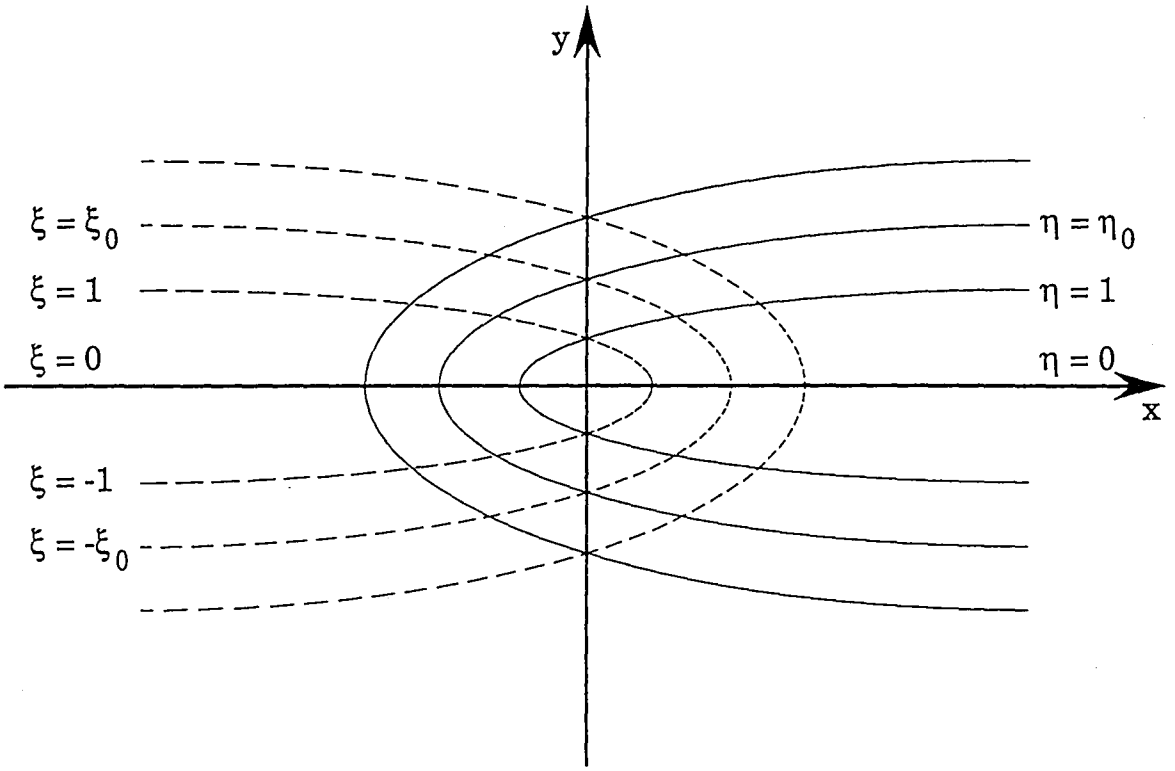

Figure 2.2 - Parabolic coordinates

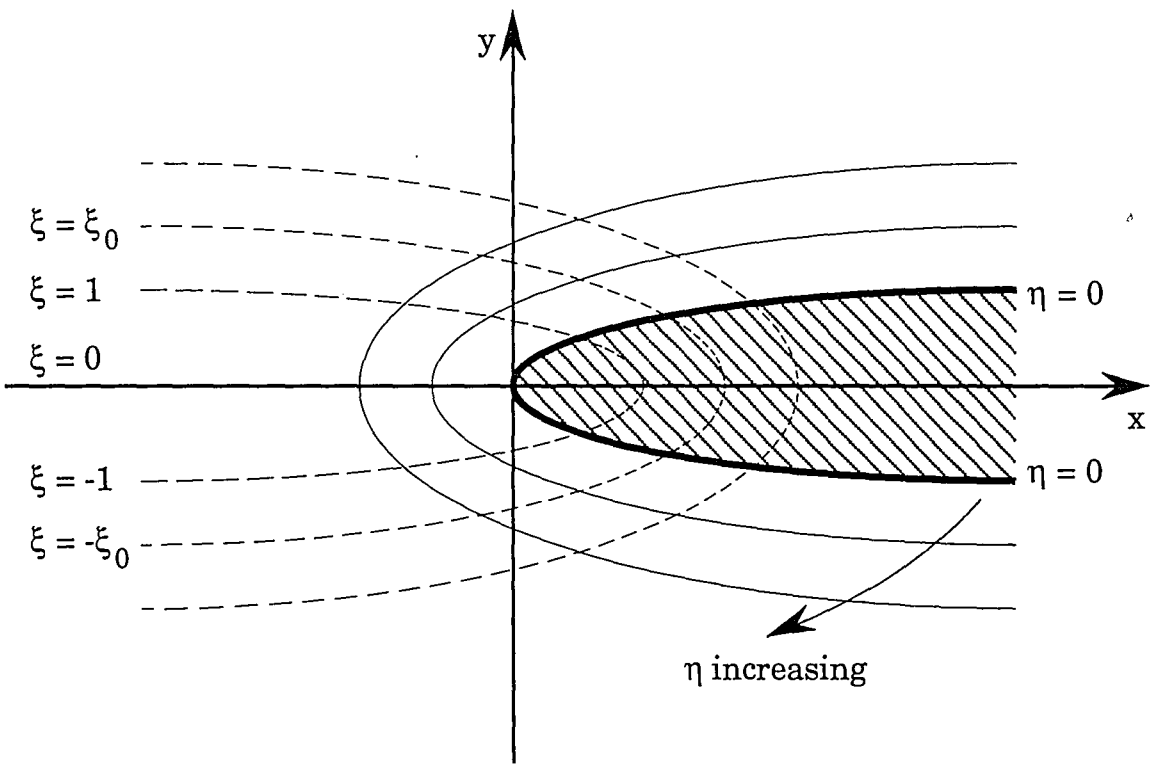

Figure 2.3 - Parabolic coordinates with airfoil surface defined as $\eta = 0$

defined by $\eta \geq 0$ correspond to the region exterior to the parabola.

To transform the governing flow equations from Cartesian coordinates to an orthogonal curvilinear coordinate system, the scale factors h_1 and h_2 must be considered (Owczarek, 1968); they are defined by

$$dx = h_1 d\xi, \quad dy = h_2 d\eta. \tag{2.5}$$

Since the coordinates are orthogonal,

$$(ds)^2 = (dx)^2 + (dy)^2 = h_1{}^2(d\xi)^2 + h_2{}^2(d\eta)^2, \tag{2.6}$$

and both scale factors may be found by differentiation of equation (2.4). It is easily shown that

$$h_1 = h_2 = \sqrt{\xi^2+(\eta+\sqrt{r_0})^2}, \tag{2.7}$$

and hence both scale factors are equivalent.

2.2.1 Inviscid Flow Solution

The fluid motion around an airfoil at zero incidence is symmetric about $\xi = 0$; on the other hand, for a pitched airfoil, the flow in the leading nose region is asymmetric with respect to $\xi = 0$. In general, the stagnation point is not located at the vertex; rather when the airfoil is pitched to a positive angle, the stagnation point is on the lower surface of the parabola (cf. Figures 1.1 and 1.2). To determine the inviscid flow around the parabola, consider the complex potential for a stagnation point located at ξ_{st} in the ζ plane (see figure 2.4) which is

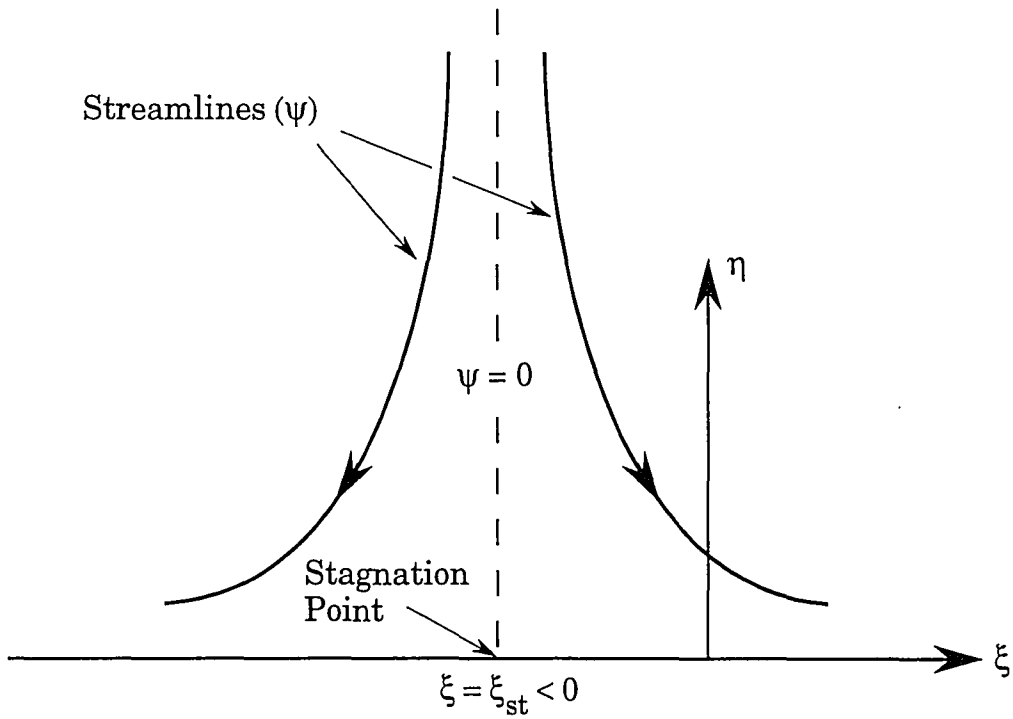

Figure 2.4 - Schematic diagram illustrating the stagnation point ξ_{st} in the ζ complex plane for an asymmetric flow.

$$\omega = \tfrac{1}{2}(\zeta - \xi_{st})^2. \tag{2.8}$$

The complex velocity in the ζ plane is defined by

$$V(\zeta) = u - iv = \frac{d\omega(\zeta)}{d\zeta} = \zeta - \xi_{st} = (\xi - \xi_{st}) + i\eta, \tag{2.9}$$

while the corresponding complex velocity in the z-plane is

$$V(z) = \frac{d\omega(z)}{dz} = \frac{d\omega}{d\zeta}\frac{d\zeta}{dz} = \frac{\zeta - \xi_{st}}{\zeta + i\sqrt{r_0}}. \tag{2.10}$$

Here $d\zeta/dz$ is determined from transformation (2.4). Note that as $\zeta \to \infty$, $V(z) \to 1$,

which corresponds to the uniform flow of unit speed at infinity in the z-plane On the other hand, the inviscid surface speed on the parabola itself at $\eta=0$ may be found from equation (2.10) and is

$$| V | = \sqrt{\frac{(\xi - \xi_{st})^2}{\xi^2 + r_0}}. \tag{2.11}$$

The upper and lower surfaces of the parabola $\eta = 0$ are defined from equation (2.4) by $\xi=\sqrt{2x}$ and $\xi=-\sqrt{2x}$, respectively. From equation (2.10), the stagnation point on $\eta = 0$ is located at $\xi_{st} = -\sqrt{2x_{st}}$; it follows from equation (2.4) that this is in the lower half plane at $y_{st} = \xi_{st} \cdot \sqrt{r_0}$.

Define

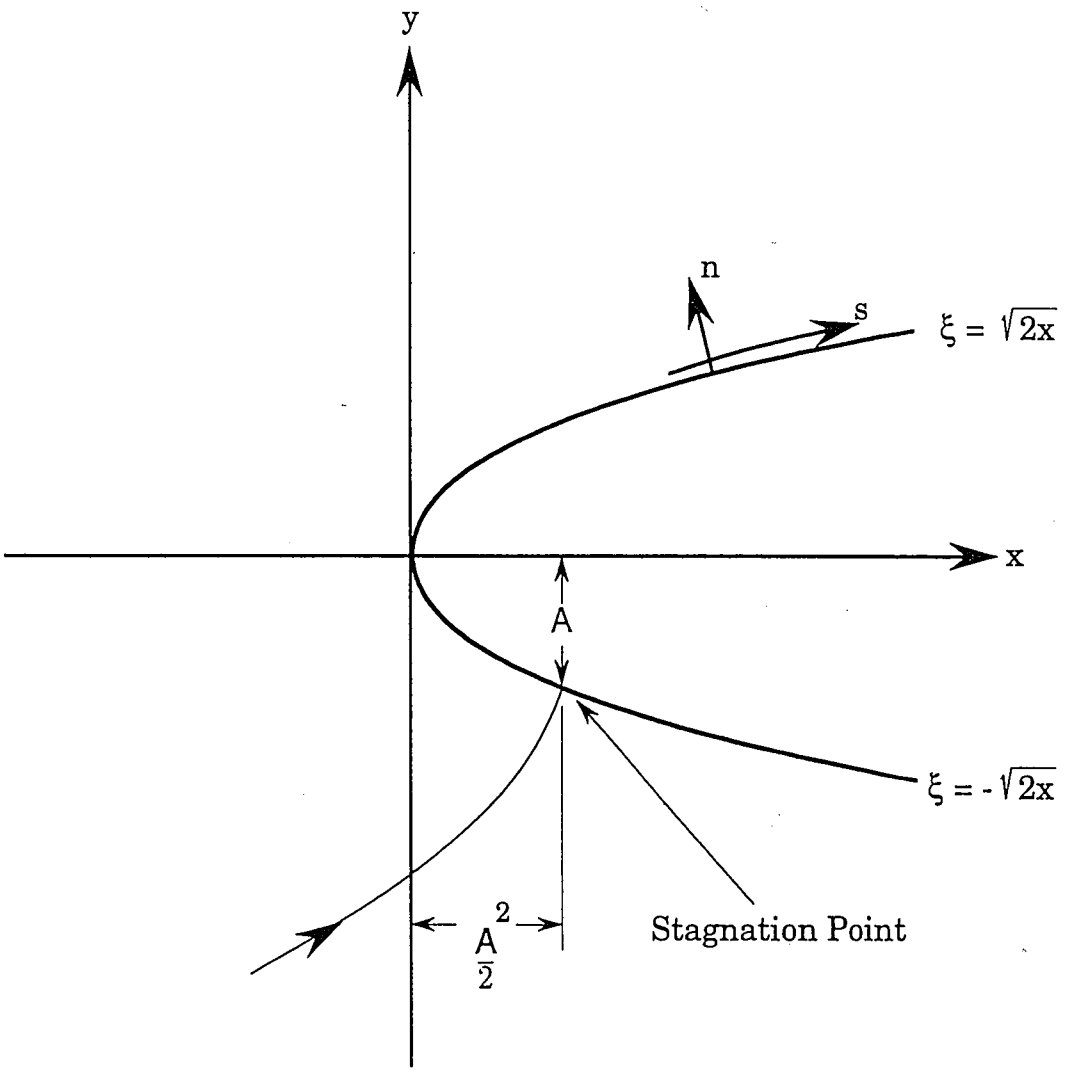

Figure 2.5 - Nomenclature for a parabola at angle of attack

$$x_{st} = \frac{\xi^2_{st}}{2} = a^2, \tag{2.12}$$

where a^2 is equal to the horizontal distance along the x-axis between the parabola's vertex and the stagnation point. Parameter "a" defines a family of inviscid solutions which all approach a uniform flow as $x^2+y^2 \to \infty$. Near the parabola, $\eta = 0$, the mainstream inviscid velocity distribution is denoted by U_∞ and from equation (2.11), it follows that

$$U_\infty(\xi,a) = \frac{\xi+\sqrt{2}\cdot a}{\sqrt{\xi^2+r_0}}. \tag{2.13}$$

Dimensionless variables are defined with respect to r_0 according to

$$x' = \frac{x}{r_0}, \quad y' = \frac{y}{r_0}, \quad \zeta' = \frac{\zeta}{\sqrt{r_0}}, \quad \xi' = \frac{\xi}{\sqrt{r_0}}, \quad \eta' = \frac{\eta}{\sqrt{r_0}}. \tag{2.14}$$

Upon suppressing the prime notation, equation (2.1) of the parabola becomes

$$y^2 = 2x, \tag{2.15}$$

while the transformation (2.4) becomes

$$z = \frac{1}{2} + \frac{1}{2}(\zeta+i)^2. \tag{2.16}$$

The scale factors defined in equation (2.7) become

$$h_1 = h_2 = \sqrt{\xi^2+(\eta+1)^2}. \tag{2.17}$$

Defining the parameter A as

$$A = \sqrt{\frac{2}{r_0}}\cdot a, \tag{2.18}$$

the inviscid mainstream velocity distribution (2.13) becomes

$$U_\infty(\xi,A) = \frac{\xi+A}{\sqrt{\xi^2+1}}. \tag{2.19}$$

The nomenclature for a parabola at an angle of attack which includes parameter A is shown in figure 2.5.

Werle and Davis (1972) have considered the possibility of steady boundary-layer solutions for the mainstream distribution given by equation (2.19). Numerical integrations were initiated at the stagnation point at $\xi = -A$ on the lower surface. For any positive value of A, the velocity initially increases with decreasing ξ and then decelerates; thus the boundary layer is exposed to a region of adverse pressure gradient. Werle and Davis (1972) determined that a steady solution is possible if A is less than a critical value of 1.158. For larger values of A, a Goldstein singularity was encountered at some positive value of ξ indicating that a steady solution is not possible and suggesting the possibility that the motion is inherently unsteady above a critical angle of attack. In terms of parameter "a," the critical value is

$$a = \sqrt{\frac{r_0}{2}} \cdot (1.158). \tag{2.20}$$

It can be shown that the parameter "a" is directly proportional to the angle of attack as determined from thin airfoil theory. Therefore, steady solutions are possible for larger angles of attack with increasing nose radius r_0.

The velocity components in the ζ plane may be defined in terms of a velocity potential ϕ and a streamfunction ψ. The complex potential (2.8) is defined as

$$w = \phi + i\psi, \tag{2.21}$$

and using equation (2.8), it is easily shown that, in the dimensionless variables defined in equation (2.14),

$$\psi = (\xi+A)\eta. \tag{2.22}$$

Therefore, the velocity components expressed in a parabolic coordinate system are

$$u_\xi = \frac{1}{h_2}\frac{\partial\psi}{\partial\eta} = \frac{\xi}{\sqrt{\xi^2+(\eta+1)^2}}, \tag{2.23}$$

$$u_\eta = -\frac{1}{h_1}\frac{\partial\psi}{\partial\xi} = -\frac{\eta}{\sqrt{\xi^2+(\eta+1)^2}}. \tag{2.24}$$

At the boundary layer edge, the mainstream velocity is

$$U_\infty(\xi,t) = \lim_{\eta\to 0} u_\xi = \frac{\xi+A}{\sqrt{\xi^2+1}}, \tag{2.25}$$

as given in equation (2.19). By taking the derivative $\partial U_\infty/\partial\xi=0$, it is easily shown that the maximum velocity occurs just past the vertex of the parabola on the upper surface where $\xi = 1/A$; the maximum value is $\sqrt{A^2+1}$. Consequently, with increasing angle of attack (and hence increasing A), the point of maximum velocity shifts toward the nose and the magnitude of the maximum increases. On the upper surface for $\xi > 1/A$, the mainstream velocity decreases monotonically and the boundary layer is exposed to a region of adverse pressure gradient.

2.2.2 Boundary Layer Problem

The boundary-layer is assumed to remain thin with thickness $O(Re^{-1/2})$, at least until separation occurs. Near the surface the normal velocity and distance are small within the boundary layer and here scaled variables are defined by

$$v = Re^{1/2}\, u_\eta, \quad Y = \eta Re^{1/2}, \tag{2.26}$$

where the Reynolds number Re is assumed to be very large. While the boundary layer is thin and attached, v and Y are O(1) within the boundary layer. The normal velocities v eventually become singular when eruption develops because the large updrafts eventually become greater than $O(Re^{-1/2})$ (see, for example, Peridier et al. 1991a). Taking $u_\xi = u$, it is easily shown that the two-dimensional streamwise momentum equation (1.1) becomes

$$\frac{\partial u}{\partial t} + \frac{1}{\sqrt{\xi^2+1}}\left\{u\frac{\partial u}{\partial \xi} + v\frac{\partial u}{\partial Y}\right\} = -\frac{1}{\sqrt{\xi^2+1}}\frac{\partial p}{\partial \xi} + \frac{1}{(\xi^2+1)}\frac{\partial^2 u}{\partial Y^2}, \tag{2.27}$$

in the limit $Re\to\infty$, while the continuity equation is

$$\frac{\partial u}{\partial \xi} + \frac{\partial v}{\partial Y} + \frac{\xi}{(\xi^2+1)}\, u = 0. \tag{2.28}$$

The velocity at the boundary-layer edge (2.25) may be written in the form

$$U\infty(\xi,t) = \frac{\xi + A(t)}{\sqrt{\xi^2+1}}, \tag{2.29}$$

where A(t) is a function of time and proportional to the angle of attack of the airfoil. As discussed previously, a critical situation is expected at whenever A(t) exceeds a critical value of 1.158. The boundary-layer problem thus formulated models the developing flow on the leading nose region for which the angle of attack of the oncoming flow is continuously changing with time.

The boundary conditions associated with the system (2.27) - (2.29) are

$$u = v = 0 \quad \text{at } \eta = 0,$$

$$\lim_{\eta \to \infty} u(\xi,\eta,t) = U\infty(\xi,t). \qquad \Big\} \quad (2.30)$$

It is evident from equation (2.29) that at downstream infinity, the external velocity is such that

$$\left.\begin{aligned} U\infty &\to \ \ 1 \qquad \text{as } \xi \to \infty, \\ U\infty &\to -1 \qquad \text{as } \xi \to -\infty, \end{aligned}\right\} \quad (2.31)$$

and thus returns to a uniform flow. There are, however, potential difficulties with the boundary-layer problem thus defined in parabolic coordinates. First, coefficients in the streamwise momentum equation (2.27) approach zero for large ξ, and second, the scale factor $\sqrt{\xi^2+1}$ becomes large as $\xi \to \infty$ thereby implying that lines of constant η move progressively further from the surface of the airfoil as $|\xi| \to \infty$.

To avoid such complications, the boundary-layer equations are transformed to a set of new coordinates. A variable s, measuring arclength along the surface of the parabola, and a scaled normal variable n are introduced (see figure 2.5).

The parabola is given parametrically by $x = \frac{1}{2}\xi^2$, $y = \xi$ in the range $-\infty < \xi < \infty$, in terms of the parabolic coordinate along the surface of the parabola. The arclength between any two points at $\xi = a$ and $\xi = b$ is given by

$$s = \int_a^b \sqrt{\left(\frac{\partial x}{\partial \xi}\right)^2 + \left(\frac{\partial y}{\partial \xi}\right)^2}\, d\xi \qquad (2.32)$$

Thus the arclength as measured from the vertex of the parabola is

$$s = \int_0^{\xi} \sqrt{t^2+1}\, dt = \frac{1}{2}\left\{\xi\sqrt{\xi^2+1} + \ln\left(\xi+\sqrt{\xi^2+1}\right)\right\}. \tag{2.33}$$

Note that this is similar to a coordinate used by Werle and Davis (1972) who chose to measure distance from the front stagnation point. In the present problem, the stagnation point is in continual motion and therefore it is convenient to measure arclength from the vertex. Introducing this new variable s, as well as a new normal variable n and velocity $\tilde{v}$ by

$$n = \sqrt{\xi^2+1}\; Y, \qquad \tilde{v} = v + \frac{2\xi\eta u}{(\xi^2+1)^{3/2}}, \tag{2.33}$$

it is easily shown that

$$\frac{\partial}{\partial\xi} = \sqrt{\xi^2+1}\,\frac{\partial}{\partial s} + \frac{2\xi\eta}{(\xi^2+1)}, \qquad \frac{\partial}{\partial Y} = \sqrt{\xi^2+1}\,\frac{\partial}{\partial n} \tag{2.34}$$

and

$$u = \frac{\partial\psi}{\partial n}, \qquad \tilde{v} = -\frac{\partial\psi}{\partial s}. \tag{2.35}$$

The streamwise momentum equation (2.27) after substitution becomes

$$\frac{\partial u}{\partial t} + u\frac{\partial u}{\partial s} + v\frac{\partial u}{\partial n} = -\frac{1}{\sqrt{\xi^2+1}}\frac{\partial p}{\partial\xi} + \frac{\partial^2 u}{\partial n^2}, \tag{2.36}$$

where the pressure distribution is derived from the inviscid solution. As described in section (1.2), as $Y\to\infty$ in equation (2.27), the imposed pressure gradient from the external flow is defined by

$$-\frac{1}{\sqrt{\xi^2+1}}\frac{\partial p}{\partial\xi} = \frac{\partial U_\infty}{\partial t} + \frac{U_\infty}{\sqrt{\xi^2+1}}\frac{\partial U_\infty}{\partial\xi}, \tag{2.37}$$

where from the definition of U_∞ (2.29),

$$\frac{\partial U_\infty}{\partial t} = \frac{1}{\sqrt{\xi^2+1}} \frac{\partial A(t)}{\partial t}, \tag{2.38}$$

$$\frac{\partial U_\infty}{\partial \xi} = \frac{1 - A(t)\cdot\xi}{(\xi^2+1)^{3/2}}. \tag{2.39}$$

2.3 EULERIAN FORMULATION

The substitution of equation (2.37) into (2.27) gives

$$\frac{\partial u}{\partial t} + u\frac{\partial u}{\partial s} + \tilde{v}\frac{\partial u}{\partial n} = \frac{\partial U_\infty}{\partial t} + \frac{U_\infty}{\sqrt{\xi^2+1}}\frac{\partial U_\infty}{\partial \xi} + \frac{\partial^2 u}{\partial n^2}, \tag{2.40}$$

with the associated continuity equation being

$$\frac{\partial u}{\partial s} + \frac{\partial v}{\partial n} = 0, \tag{2.41}$$

The boundary conditions are

$$\left.\begin{aligned} u &= 0 && \text{at } n = 0, \\ u &\to U_\infty(\xi,t) && \text{as } n \to \infty. \end{aligned}\right\} \tag{2.42}$$

Since the boundary layer has a thickness proportional to $\sqrt{t}$ after the impulsive start, it is convenient to introduce Rayleigh variables (Doligalski & Walker, 1984) according to

$$\Psi(s,n,t) = \frac{\psi}{2\sqrt{t}}, \qquad \zeta = \frac{n}{2\sqrt{t}}. \tag{2.43}$$

Let the streamwise velocity in terms of the unsteady streamfunction Ψ be denoted by

$$U = \frac{\partial \Psi}{\partial \zeta}. \tag{2.44}$$

and upon substituting, the streamwise momentum equation becomes

$$4t\,\frac{\partial U}{\partial t} = 4t\left\{\frac{\partial U_\infty}{\partial t} + \frac{U_\infty}{\sqrt{\xi^2+1}}\,\frac{\partial U_\infty}{\partial \xi}\right\} + \left\{2\zeta + 4t\,\frac{\partial \Psi}{\partial s}\right\}\frac{\partial U}{\partial \zeta} - \tag{2.45}$$

$$4t\;U\frac{\partial U}{\partial s} + \frac{\partial^2 U}{\partial \zeta^2}.$$

The boundary conditions are

$$\left.\begin{aligned} &\Psi = U = 0, && \text{at } \zeta = 0, \text{ all s, t} \\ &U \to U\infty, && \text{as } \zeta \to \infty, \text{ all s, t.} \end{aligned}\right\} \tag{2.46}$$

To determine the initial conditions, let time t→0, and then equation (2.45) reduces to

$$\frac{\partial^2 U}{\partial \zeta^2} + 2\zeta\,\frac{\partial U}{\partial \zeta} = 0, \tag{2.47}$$

subject to the conditions (2.46). The solution to equation (2.47) is

$$U(\xi,\eta,0) = U_\infty(\xi,t)\;\mathrm{erf}(\zeta), \tag{2.48}$$

and integration of equation (2.44) yields

$$\Psi(\xi,\eta,0) = U_\infty \cdot \left\{\zeta \cdot \mathrm{erf}(\zeta) + \frac{1}{\sqrt{\pi}}\left(e^{-\zeta^2} - 1\right)\right\}. \tag{2.49}$$

These equations give the initial condition from which the solution of equation (2.45) may be integrated forward in time.

The boundary conditions as $\xi \to \pm\infty$ must be considered also. At downstream infinity on the top surface of the parabola (s→∞), $U_\infty \to 1$, while

on the bottom surface ($s \to -\infty$), $U_\infty \to -1$. It is easy to show that equation (2.45) reduces to (2.47) for all time t as $\xi \to \pm\infty$ and that the solution there is also given by equations (2.48) and (2.49). Therefore,

$$U \to U_\infty(\xi,t)\ \mathrm{erf}(\zeta) \qquad \text{as } s \to \pm\infty,\ \text{all } \zeta,\ \text{all } t. \tag{2.50}$$

The boundary-layer problem is defined on an infinite domain ($-\infty < s < \infty$) in the streamwise direction and a semi-infinite domain ($0 < \zeta < \infty$) in the normal direction. For computational purposes, it is convenient to introduce new variables defined by

$$\hat{s} = \frac{1}{\pi}\arctan\left(\frac{s}{b_k}\right) + \frac{1}{2}, \tag{2.51}$$

$$\hat{\zeta} = \frac{2}{\pi}\arctan\left(\frac{\zeta}{a_k}\right), \tag{2.52}$$

which map s and ζ to finite intervals in $\hat{s}$ and $\hat{\zeta}$, respectively. Here, a_k and b_k are expansion factors used to control the mapping of the physical coordinates to the rectangular computational mesh; with smaller values of a_k and b_k, relatively more points are packed near $s = 0$ (the vertex of the parabola) and $\zeta = 0$ (the wall), respectively. The independent arclength variable s is mapped from a doubly infinite range

$$\infty \le s \le \infty \quad \text{to the range} \quad 0 \le \hat{s} \le 1, \tag{2.53}$$

and the independent normal variable is mapped from

$$0 \le \zeta \le \infty \quad \text{to the range} \quad 0 \le \hat{\zeta} \le 1. \tag{2.54}$$

The inverse transformations are

$$s = b_k \cdot \tan[\pi(\hat{s} - \tfrac{1}{2})], \tag{2.55}$$

$$\zeta = a_k \cdot \tan(\frac{\pi}{2}\hat{\zeta}). \tag{2.56}$$

Thus the partial derivatives are transformed into

$$\frac{\partial}{\partial s} = \frac{1}{\pi b_k}\cos^2[\pi(\hat{s} - \frac{1}{2})]\,\frac{\partial}{\partial \hat{s}}, \qquad \frac{\partial}{\partial \zeta} = = \frac{2}{\pi a_k}\cos^2(\frac{\pi}{2}\hat{\zeta})\,\frac{\partial}{\partial \hat{\zeta}}, \tag{2.57}$$

$$\frac{\partial^2}{\partial \zeta^2} = \frac{4}{\pi^2 {a_k}^2}\cos^4(\frac{\pi}{2}\hat{\zeta})\,\frac{\partial^2}{\partial \hat{\zeta}^2} - \frac{4}{\pi {a_k}^2}\cos^3(\frac{\pi}{2}\hat{\zeta})\sin(\frac{\pi}{2}\hat{\zeta})\,\frac{\partial}{\partial \hat{\zeta}}. \tag{2.58}$$

After dividing equation (2.45) by 4t, the partial differential equation describing the Eulerian formulation of the problem can be written in the following general form:

$$\frac{\partial U}{\partial t} = P\frac{\partial^2 U}{\partial \hat{s}^2} + Q\frac{\partial^2 U}{\partial \hat{s}\,\partial \hat{\zeta}} + R\frac{\partial^2 U}{\partial \hat{\zeta}^2} + S\frac{\partial U}{\partial \hat{s}} + T\frac{\partial U}{\partial \hat{\zeta}} + WU + \Gamma, \tag{2.59}$$

where U is defined in terms of Ψ by

$$U = \frac{2}{\pi a_k}\cos^2(\frac{\pi}{2}\hat{\zeta})\,\frac{\partial \Psi}{\partial \hat{\zeta}}. \tag{2.60}$$

The coefficients in equation (2.59) are given by:

$$P = 0, \qquad Q = 0, \qquad W = 0 \tag{2.61}$$

$$R = \frac{1}{t\pi^2 {a_k}^2}\cos^4\alpha, \quad S = -\frac{1}{\pi b_k}U \cdot \cos^2\omega, \tag{2.62}$$

$$T = \frac{\cos^2\alpha}{\pi^2}\left\{\frac{\pi \tan\alpha}{t}\left(1 - \frac{\cos^2\alpha}{{a_k}^2}\right) + \frac{2\cos^2\omega}{a_k \cdot b_k}\frac{\partial \Psi}{\partial \hat{s}}\right\}, \tag{2.63}$$

$$\Gamma = \frac{\partial U_\infty}{\partial t} + \frac{U_\infty \, \partial U_\infty}{\sqrt{\xi^2+1} \, \partial \xi}, \tag{2.64}$$

where α and β denote

$$\alpha = \frac{\pi}{2}\hat{\zeta}, \qquad \omega = \pi(\hat{s} - \frac{1}{2}). \tag{2.65}$$

Recall that $\frac{\partial U_\infty}{\partial t}$ is defined by (2.38) and $\frac{\partial U_\infty}{\partial \xi}$ by (2.39). Finally, the boundary conditions (2.46) and (2.50) in this description are given by

$$\left.\begin{aligned} U &= 0 && \text{at } \hat{\zeta} = 0, \\ U &= U_\infty(\xi,t) && \text{at } \hat{\zeta} = 1, \\ U &= U_\infty \cdot \mathrm{erf}[a_k \cdot \tan(\tfrac{\pi}{2}\hat{\zeta})] && \text{at } \hat{s} = 0,1. \end{aligned}\right\} \tag{2.66}$$

2.4 EULERIAN NUMERICAL PROCEDURES

This study constitutes an extension of previous research that focussed on the development of the boundary layer at the leading nose region of an airfoil whose angle of attack was abruptly changed from zero to a finite angle. The computer programs utilized in that research (Degani et al, 1994) have been modified here to treat the present model of a pitching airfoil.

The Eulerian formulation was used to initiate the calculation for the pitching airfoil. The motion was impulsively started from rest at t=0 and at $A(0) = 0$, corresponding to zero angle of attack. With increasing time, the angle of attack was increased normally as a linear function of time.

A rectangular mesh was defined in the computational domain $0 \leq \hat{s} \leq 1$ and $0 \leq \hat{\zeta} \leq 1$. A number of meshes were used as a test of the accuracy, and the number of mesh points ranged from 601 × 201 to 201 × 101; here the

first number denotes the number of points in the $\hat{s}$ direction while the second corresponds to those in the $\hat{\zeta}$ direction. The velocity U was calculated at each time step Δt. The solution was advanced forward in time beginning at $t = 0$ when the motion was assumed to be impulsively started from rest when the airfoil was at zero angle of attack. A number of time steps were used as a check on the accuracy with typical time steps being in the range $\Delta t = 0.0005$ to 0.0025. At each time step, the solution for U was computed iteratively until all values in the mesh had converged to five significant figures. The angle of attack increased continually as A(t) increased. Since the external velocity is a function of A(t), $U_\infty(\xi,t)$ was recalculated for each new time t. In addition, because the boundary layer problem is cast in terms of s as opposed to the parabolic coordinate ξ, the values of ξ were found by solving equation (2.33) with the Newton-Raphson method.

At any value of t, the solution for U was calculated using a factored ADI (alternating-direction-implicit) numerical solver method which also employs an "upwind-downwind" differencing scheme and the Thomas algorithm (see Peridier et al, 1991a). These numerical methods are briefly described in Appendix A. Upon completion of one ADI cycle, the streamfunction Ψ was found from the integration of equation (2.44) using Simpson's method along lines of constant s. The solution for U and Ψ were saved and the process was advanced to the next time step.

The Eulerian program was allowed to continue until convergence was no longer achieved; this occurs because the numerical resolution is compromised as the boundary layer starts to approach separation. The calculations were terminated when the convergence test was not satisfied after a specified

maximum amount of iterations at any given time step. In order to continue the integrations with good accuracy, it was necessary to move to a Lagrangian formulation and this is considered next.

2.5 LAGRANGIAN FORMULATION

As described in section 1.2, independent boundary-layer variables in the Lagrangian formulation are the initial positions (χ,ρ) of the fluid particles, viz.

$$s(\chi,\rho,t) = \chi, \qquad n(\chi,\rho,t) = \rho, \qquad \text{at } t=t_0. \tag{2.67}$$

The streamwise particle positions and their tangential velocities are the principle dependent variables, i.e.

$$s = s(\chi,\rho,t), \qquad u = u(\chi,\rho,t). \tag{2.68}$$

The system of two coupled, unsteady equations in Lagrangian variables is derived from the Eulerian formulation in Appendix B and is repeated here:

$$\left.\begin{aligned} &\frac{\partial s}{\partial t} = u, \\ &\frac{\partial u}{\partial t} = \frac{\partial U_\infty}{\partial t} + \frac{U_\infty}{\sqrt{\xi^2+1}}\frac{\partial U_\infty}{\partial \xi} + \left(\frac{\partial s}{\partial \chi}\frac{\partial}{\partial \rho} - \frac{\partial s}{\partial \rho}\frac{\partial}{\partial \chi}\right)^2 u. \end{aligned}\right\} \tag{2.69}$$

As in the Eulerian case, the Lagrangian boundary-layer equations can be written in the following general form:

$$\frac{\partial u}{\partial t} = P\frac{\partial^2 u}{\partial \hat{\chi}^2} + Q\frac{\partial^2 u}{\partial \hat{\chi}\partial \hat{\rho}} + R\frac{\partial^2 u}{\partial \hat{\rho}^2} + S\frac{\partial u}{\partial \hat{\chi}} + T\frac{\partial u}{\partial \hat{\rho}} + Wu + \Gamma, \tag{2.70}$$

$$\frac{\partial s}{\partial t} = u, \tag{2.71}$$

where the functional coefficients P, Q, R, S, T, W and Γ will be defined subsequently. Here, the dependent spatial variable s and the independent spatial variables χ and ρ have been mapped to finite domains by the following transformations:

$$\hat{s} = \frac{1}{\pi}\arctan\left(\frac{s}{b_k}\right) + \frac{1}{2}, \qquad 0 \le \hat{s} \le 1, \tag{2.72}$$

$$\hat{\chi} = \frac{1}{\pi}\arctan\left(\frac{\chi}{b_k}\right) + \frac{1}{2}, \qquad 0 \le \hat{\chi} \le 1, \tag{2.73}$$

$$\hat{\rho} = \frac{2}{\pi}\arctan\left(\frac{\rho}{a_k}\right), \qquad 0 \le \hat{\rho} \le 1. \tag{2.74}$$

The boundary condition along the surface of the airfoil is simply the no-slip condition,

$$u = 0 \qquad \text{at} \qquad \hat{\rho} = 0, \tag{2.75}$$

which states that particles initially on the surface remain there for all t. Fluid particles which are initially at an infinite distance from the surface remain so but their streamwise positions must change as a function of time and their velocities must match the mainstream velocity distribution at the boundary-layer edge according to

$$u \to U_\infty(\xi,t), \qquad \hat{\rho} \to 1. \tag{2.76}$$

The boundary conditions at upstream and downstream infinity state that the particles initially located there remain there for all time $t > t_0$, viz.

$$\hat{s}(0,\hat{\rho},t) = 0, \qquad \hat{s}(1,\hat{\rho},t) = 1. \tag{2.77}$$

It is easily shown that the velocity u at upstream and downstream infinity is time dependent corresponding to a Rayleigh solution (Peridier et al, 1991a) given in terms of the present coordinates by

$$u(\hat{\chi},\hat{\rho},t) = U_{\infty}(\xi,t)\cdot \mathrm{erf}\left(\frac{\tan\frac{\pi}{2}\hat{\rho}}{2\sqrt{t}}\right) \quad \text{at } \hat{\chi} = 0,\ 1, \tag{2.78}$$

It is convenient to define the following variables so that the coefficients in equation (2.70) may be written in condensed form:

$$\alpha = \frac{\pi}{2}\hat{\rho}, \qquad \omega = \pi(\hat{\chi}-\frac{1}{2}), \qquad \Omega = \frac{4}{\pi^2 {a_k}^2}\cos^4\alpha\cdot\frac{\cos^4[\pi(\hat{\chi}-\frac{1}{2})]}{\cos^4[\pi(\hat{s}-\frac{1}{2})]}. \tag{2.79}$$

Now, the coefficients are defined as:

$$P = \Omega\cdot\left(\frac{\partial\hat{s}}{\partial\hat{\rho}}\right)^2, \tag{2.83}$$

$$Q = -2\Omega\cdot\frac{\partial\hat{s}}{\partial\hat{\chi}}\frac{\partial\hat{s}}{\partial\hat{\rho}}, \tag{2.84}$$

$$R = \Omega\cdot\left(\frac{\partial\hat{s}}{\partial\hat{\chi}}\right)^2, \tag{2.85}$$

$$S = \Omega\cdot\left\{\frac{\partial\hat{s}}{\partial\hat{\rho}}\frac{\partial^2\hat{s}}{\partial\hat{\chi}\partial\hat{\rho}} - \frac{\partial\hat{s}}{\partial\hat{\chi}}\frac{\partial^2\hat{s}}{\partial\rho^2} - 2\pi\cdot\tan\omega\cdot\left(\frac{\partial\hat{s}}{\partial\hat{\rho}}\right)^2 + \pi\cdot\tan\alpha\cdot\frac{\partial\hat{s}}{\partial\hat{\chi}}\frac{\partial\hat{s}}{\partial\hat{\rho}}\right\}, \tag{2.86}$$

$$T = \Omega\cdot\left\{\frac{\partial\hat{s}}{\partial\hat{\chi}}\frac{\partial^2\hat{s}}{\partial\hat{\chi}\partial\hat{\rho}} - \frac{\partial\hat{s}}{\partial\hat{\rho}}\frac{\partial^2\hat{s}}{\partial\hat{\chi}^2} - \pi\cdot\tan\alpha\cdot\left(\frac{\partial\hat{s}}{\partial\hat{\chi}}\right)^2 + 2\pi\cdot\tan\omega\cdot\frac{\partial\hat{s}}{\partial\hat{\chi}}\frac{\partial\hat{s}}{\partial\hat{\rho}}\right\}, \tag{2.87}$$

$$W = 0, \tag{2.88}$$

$$\Gamma = \frac{\partial U_\infty}{\partial t} + \frac{U_\infty}{\sqrt{\xi^2+1}} \frac{\partial U_\infty}{\partial \xi}. \tag{2.89}$$

Here, U_∞ is given as a function of (ξ,t) by equation (2.29), where ξ is the parabolic coordinate shown in figure 2.3.

2.6 LAGRANGIAN NUMERICAL PROCEDURES

In the present study, calculations were carried out in the Eulerian formulation for t in the range $0 \leq t \leq t_0$, comprising a majority of the total integration time. In general, the Eulerian computation is considerably more efficient and the Lagrangian scheme was used only when needed. As a boundary-layer eruption starts to develop, the solution develops a severe local variation in flow properties over narrow streamwise distances and eventually the Eulerian integration fails to converge. Therefore, at a time t_0 well in advance of this occurrence and while the Eulerian velocity field was still smooth, the calculation was switched to the Lagrangian formulation and continued in this mode until separation was encountered.

As the Eulerian calculation arrives at time t_0, the stretching factors for the streamwise and normal transformations a_k and b_k in equations (2.55) and (2.56), respectively, have values which have been held fixed throughout the course of the integration. The initial conditions for the Lagrangian integrations are defined by equations (2.67), with transformed independent variables given by equations (2.73) and (2.74). It is evident that if the streamwise factor b_k is used with the normal factor increased to $2\sqrt{t_0}\ a_k$, the

same grid can be used to initiate the Lagrangian integration. It may be noted that the simplification is not necessary and is merely convenient since interpolation is avoided at the switch-over time at t_0.

At any time step, both dependent variables s and u are unknown for each fluid particle and, because the equations are nonlinear and coupled, iteration is necessary at each time step. At any stage in this procedure, the position of each particle is predicted by using the current estimate of $u_{i,j}$ and the known value in the previous time plane at $t = t^*$. This is accomplished through the integration of (2.71), viz.

$$s_{i,j} = s^*_{i,j} + \frac{\Delta t}{2}(u_{i,j} + u^*_{i,j}). \tag{2.90}$$

Then $\hat{s}$ is found from transformation (2.72), and a new current estimate of $u_{i,j}$ is calculated by using the factored ADI numerical scheme given in appendix A to solve equation (2.70). If this current value of $u_{i,j}$ failed to satisfy the convergence tolerance (i.e. agreement to five significant figures with the previous iterate), a new estimate of the particle positions was predicted by (2.90) and a further iterate for $u_{i,j}$ was obtained.

The external velocity U_∞ changes as a function of time and as a particle arrives at any ξ location, it is necessary to obtain the pressure gradient at that value of ξ and at time t. At any time, U_∞ was defined as a function of ξ and cubic splines were used to interpolate the quantities of Γ in (2.89) that involve U_∞. Thus, interpolation was also used to calculate U_∞ at each position s in the computational domain.

The Lagrangian scheme is computationally intensive because at each time step, the vertical position n of each particle must be calculated from the

known values of its corresponding streamwise position χ in order to check for the possible evolution of a separation singularity. This is accomplished through integration of the continuity equation using the method of characteristics. The curves of $s(\chi,\rho,t)$=constant are the characteristic curves (i.e. integration is along a path of constant s that passes through the point χ,ρ), and the necessary integral is

$$n(\chi,\rho,t) = \int_{\text{surface}}^{(\chi,\rho)} \frac{dz}{\sqrt{s_\chi{}^2+s_\rho{}^2}}. \tag{2.91}$$

It is evident that when a stationary point develops, i.e.

$$\frac{\partial s}{\partial \chi} = \frac{\partial s}{\partial \rho} = 0, \tag{2.92}$$

a singularity develops in the boundary-layer solution at time $t=t_s$. That is, $n(\chi,\rho,t)$ becomes large on the characteristic near the singular point at $t = t_s$; this is simply an indication that fluid particles are becoming severely compressed in the streamwise direction as separation develops, and by continuity, must grow substantially in a direction normal to the wall (Peridier, 1989). It is noted in passing that the Lagrangian integration may on occasion encounter convergence difficulties prior to t_s. This occurs whenever the Lagrangian calculation is run for significant periods and is an indication that fluid particles have been swept out of various regions of the flow field. Consequently, fluid particles which were initially close together now become far apart and the gradients such as $\partial s/\partial \chi$ in equation (2.69) become large. This problem was cured in the present study by a process of remeshing in which the integration was stopped and the corresponding Eulerian velocity

field was calculated, in a manner to be described in the next chapter; from this field the Lagrangian calculation was started again. It should be noted that remeshing can only be carried out with good accuracy at times well before t_s when the Eulerian velocity field is sufficiently smooth.

The development of a separation singularity concludes the integration. When such a singularity is encountered, it is an indication that the boundary layer is about to separate in a violently focussed eruption. A continuation of the integrations would require the use of an additional subset of the Navier-Stokes equations and, thus, is beyond the scope of this study. Calculated results leading up to this event are given in chapter 3.

CHAPTER 3
CALCULATED RESULTS

3.1 INTRODUCTION

In this chapter, calculated results will be given for several properties of interest which characterize the pitching airfoil problem. Here, the four main quantities of interest will be described; these are: (1) streamlines; (2) vorticity; (3) wall shear stress; and (4) normal perturbation velocity.

Recall that the velocity u in Eulerian variables is defined in terms of the streamfunction Ψ by

$$u = \frac{\partial \Psi}{\partial \zeta} = \frac{\partial \psi}{\partial n}. \tag{3.1}$$

The instantaneous **streamlines** are lines of constant Ψ or, equivalently, lines of constant ψ. To plot the streamlines, the streamfunction was calculated at all the nodes in the rectangular mesh at a particular time by integrating equation (3.1) from the wall, where $\Psi = 0$, using Simpson's method. Using equation (2.43), the unsteady streamfunction is converted from Rayleigh variables to $\psi = 2\sqrt{t} \cdot \Psi$. The instantaneous streamlines are then found by plotting lines of constant ψ.

The fluid **vorticity** $\vec{\omega}$ is defined as twice the rotation of a fluid particle. In two-dimensional flow there is only one component of vorticity ω and the boundary-layer vorticity in Eulerian variables is given by

$$\omega = -\frac{\partial U}{\partial \zeta}. \tag{3.2}$$

In computational coordinates, the scalar vorticity is calculated using

transformation (2.56) according to

$$\omega = -\frac{2}{\pi a_k}\cos^2\left(\frac{\pi}{2}\hat{\zeta}\right)\frac{\partial U}{\partial \hat{\zeta}}. \tag{3.3}$$

The vorticity is zero on the boundaries $\hat{\zeta}=1$ and $\hat{s}=0,1$ while the vorticity is calculated at the internal nodes in the mesh using a central difference approximation, viz.

$$\frac{\partial u_{i,j}}{\partial \hat{\zeta}} = \frac{1}{2(\Delta\hat{\zeta})}(u_{i,j+1} - u_{i,j-1}). \tag{3.4}$$

Finally, the vorticity in Lagrangian variables prior to a transformation to computational coordinates is

$$\omega = -\left(\frac{\partial s}{\partial \chi}\frac{\partial u}{\partial \rho} - \frac{\partial s}{\partial \rho}\frac{\partial u}{\partial \chi}\right), \tag{3.5}$$

where $s=s(\chi,\rho,t)$ and $u=u(\chi,\rho,t)$; thus ω may be evaluated at each internal point in the mesh by central difference approximations. A technique to obtain ω on an Eulerian mesh from Lagrangian data is described by Peridier et al (1991a).

The definition of dimensionless **wall shear stress** is

$$\tau_w(s,t) = \frac{\partial u}{\partial \zeta}\Big|_{\zeta=0}, \tag{3.6}$$

and in terms of computational coordinates,

$$\tau_w(\hat{s},t) = \frac{2}{\pi a_k}\frac{\partial u}{\partial \hat{\zeta}}\Big|_{\hat{\zeta}=0}. \tag{3.7}$$

The wall shear stress at a given time is numerically calculated at $\hat{\zeta}=0$ by using a second order accurate forward-difference equation according to

$$\left.\frac{\partial u_{i,j}}{\partial \hat{\zeta}}\right)_{\hat{\zeta}=0} = \frac{1}{2(\Delta\hat{\zeta})}\left(-3u_{i,1} + 4u_{i,2} - u_{i,3}\right). \tag{3.8}$$

The **normal perturbation velocity** v_1 is evaluated here as an indicator of local boundary-layer growth and outflows from the boundary layer, instead of the displacement thickness δ^*. Since δ^* is defined in general as

$$\delta^* = \int_0^\infty \left(1 - \frac{u}{U_\infty}\right) dn, \tag{3.9}$$

it is evident that δ^* is undefined if $U_\infty(\xi,t)$ has zeros. Thus it is necessary to seek an alternate variable that is characteristic of boundary-layer growth. In general

$$u = \frac{\partial \psi}{\partial n} \sim U_\infty \qquad \text{as } n\to\infty, \tag{3.10}$$

at the boundary-layer edge and, therefore, integration yields

$$\psi \sim U_\infty(\xi,t)\cdot n + \tilde{A}(\xi,t) \qquad \text{as } n\to\infty, \tag{3.11}$$

where $\tilde{A}(\xi,t)$ is easily determined from the boundary-layer solution at any time t. The significance of $\tilde{A}$ is as follows.

The boundary layer induces perturbations of $O(Re^{-1/2})$ in the outer flow, viz.

$$u = u_0(s,n,t) + Re^{-1/2}u_1(s,n,t) + \dots , \tag{3.12}$$

$$v = v_0(s,n,t) + Re^{-1/2} v_1(s,n,t) + \dots , \tag{3.13}$$

where

$$u_0 \to U_\infty(\xi,t) \qquad \text{as } n \to 0. \tag{3.14}$$

Furthermore, the continuity equation is satisfied with

$$v_0 \to -n \cdot \frac{\partial U_\infty}{\partial s} \qquad \text{as } n \to 0. \tag{3.15}$$

Again, on the boundary-layer scale,

$$v = Re^{-1/2}\, V, \qquad n = Re^{-1/2}\, Y, \tag{3.16}$$

and the equation of conservation of mass (1.2) becomes

$$\frac{\partial u}{\partial s} + \frac{\partial V}{\partial Y} = 0. \tag{3.17}$$

Integration of equation (3.17) yields

$$V = -\int_0^Y \frac{\partial u}{\partial s}\, dY = -\frac{\partial \psi}{\partial s}. \tag{3.18}$$

The substitution of equation (3.11) into (3.18) gives

$$V \sim -\frac{\partial U_\infty(\xi,t)}{\partial s} \cdot Y - \frac{\partial \tilde{A}(\xi,t)}{\partial s}. \tag{3.19}$$

The velocity v is matched at the interface between the outer flow and the boundary layer, viz.

$$\lim_{Y\to\infty} Re^{-1/2}\, V = \lim_{n\to 0} (v_0 + Re^{-1/2}\, v_1). \tag{3.20}$$

Substitution of (3.19) into (3.20) yields

$$\mathrm{Re}^{-1/2}\left(-\frac{\partial U_\infty}{\partial s}\cdot Y-\frac{\partial \tilde{A}}{\partial s}\right)\sim \zeta\frac{\partial U_\infty}{\partial s}+\mathrm{Re}^{-1/2}\,v_1. \tag{3.21}$$

Substituting the definition of n in equation (3.16) into expression (3.21) yields

$$v_1=-\frac{\partial \tilde{A}\,(\xi(s),t)}{\partial s}. \tag{3.22}$$

Figure 3.1 shows a schematic sketch of a typical normal perturbation parameter $\tilde{A}\,(\xi(s),t)$ and the functional relationship between v_1 and $\partial\tilde{A}/\partial s$. Wherever $\tilde{A}$ is decreasing, an outflow from the boundary layer is implied while regions where $\tilde{A}$ increases imply inflow to the boundary layer.

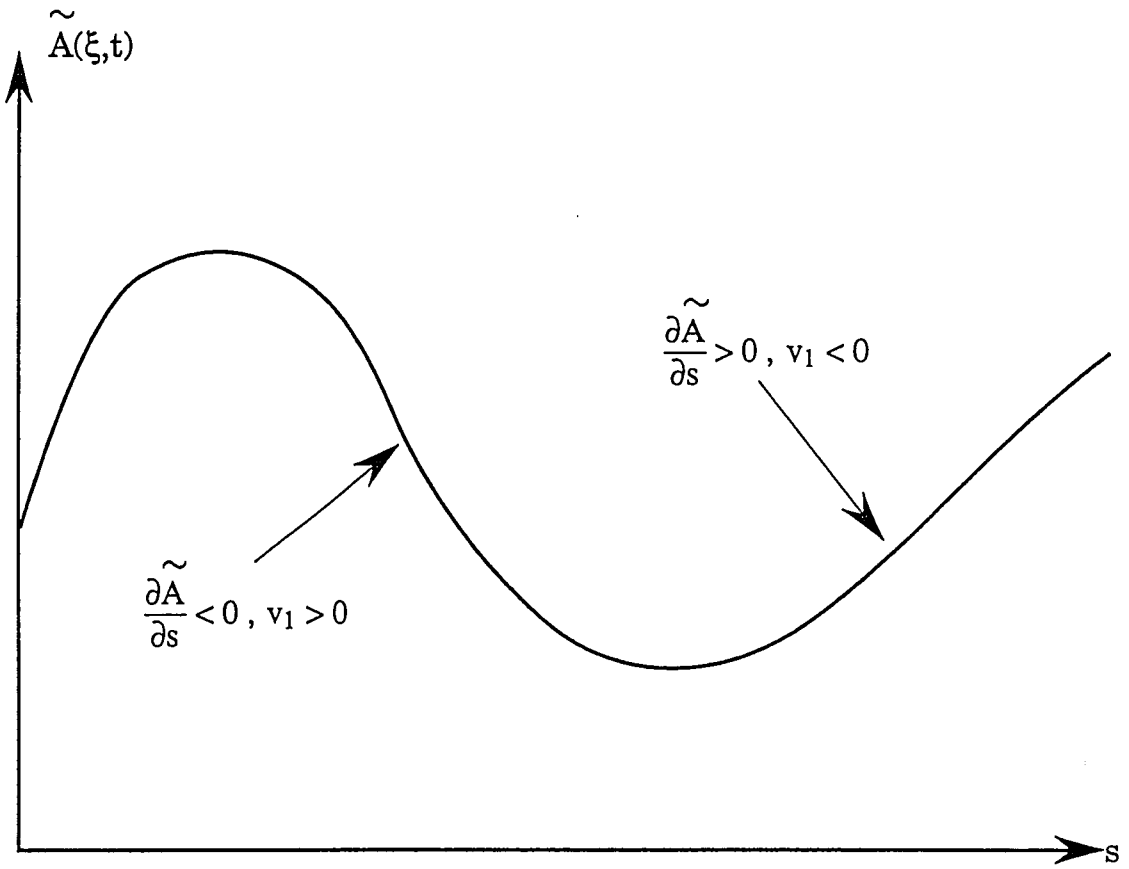

Figure 3.1 - A general sketch of the parameter $\tilde{A}(\xi(s),t)$ in the normal perturbation velocity $v_1 = -\frac{\partial \tilde{A}}{\partial s}$

3.2 INCREASING ANGLE OF ATTACK

This section contains the results of the boundary-layer integrations for the case when the angle of attack is increasing linearly with time; the main case that will be documented in detail is $A(t) = t$. However, other situations for which $A(t) = ct$ were also considered. These situations model the instantaneous flow near the leading edge of an airfoil which is pitched up uniformly in a stream to have an angle of attack that increases linearly with time. The following figures are plotted on the boundary-layer scale in a frame of reference fixed on the parabola and show the flow patterns in the thin boundary layer.

Initially, the numerical solution was calculated on a 201 by 101 (201 points in $\hat{s}$ and 101 points in $\hat{\zeta}$) rectangular mesh using a uniform time step of $\Delta t = 0.001$. Subsequently refined results were calculated using a refined mesh of 401 by 201 and a uniform time step of $\Delta t = 0.0005$. The time steps were chosen after some experimentation and are believed to be sufficiently small to ensure good accuracy. The two sets of results agree closely and are believed to be grid independent, at least to the resolution shown on the following graphs. The resolution in the vertex region of the parabola was enhanced by using transformations (2.55) - (2.56) or (2.72) - (2.74) to concentrate mesh nodes in the nose region in the physical space. The normal expansion factor was $a_k = 0.8$ for the Eulerian formulation and $a_k = 2\sqrt{t_0} \times 0.8$ for the Lagrangian approach while the streamwise expansion factor was $b_k = 2.3$ for both calculations. The calculation may be switched from the Eulerian to Lagrangian at any reasonable value of t, without significant influence on the

computed results. The results shown were for a switch at $t_0 = 2$; according to $a_k = 2\sqrt{t_0} \times 0.8$, the expansion factor for the balance of the Lagrangian calculation was $a_k = 2.26$.

The Eulerian formulation of the boundary-layer equations was implemented first. The flow was impulsively started at $t = 0$ and the solution process continued until successive iterates for u at each time step converged to five significant figures; the integration failed at about $t = 4.8$ when convergence could no longer be obtained. The Lagrangian program was started at $t_0 = 2.0$ by using the Eulerian results as the initial condition. In other computational runs, initial conditions at other values of t_0 had no effect on the subsequent results. For $t = t_0$, it was necessary to remesh the Lagrangian solution at times $t = 2.8$, 3.4, 3.8, 4.1, and 4.5, when using the most refined mesh. An increase in the number of iterations in the Lagrangian calculations is an indication that fluid particles have been swept out of various local flow regions in the boundary layer. When this occurs, it is convenient to stop the integration and redefine a new Lagrangian mesh. This is particularly important here where the Lagrangian calculation is relatively lengthy.

In the Lagrangian calculation, the continuity equation is solved by the method of characteristics. The characteristic curves are vertical straight lines at the start of the calculation as depicted in figure 3.2(a) at the last remeshing at $t = 4.5$. These contours physically represent the locations of fluid particles that have all arrived at lines of constant $\hat{s}$ at the current time plane (Peridier, 1989). As time increases, these initial straight lines of constant $\hat{s}$ distend as shown in figures 3.2(b) through 3.2(f). Note that fluid particles on the surface

of the parabola do not move. The contours near upstream and downstream infinity remain virtually vertical because the particles experience little movement. The "bulge" that develops in the characteristics indicates that the fluid particles in this region have experienced the greatest drift since the last remeshing at $t = 4.5$. Figure 3.2(f) shows the stationary point that develops in the "thumb-like" region of the constant $\hat{s}$ contours; this point is calculated using the method described in section 2.6. Thus, a singularity has developed in the boundary layer at $t_s = 4.752$.

The instantaneous streamlines near the leading nose in Cartesian coordinates, x and y, are plotted for various times in figures 3.3(a) through 3.3(f). As time increases, the angle of attack increases and the stagnation point moves along the lower surface of the parabola away from the vertex. Figure 3.3(c) shows the presence of a recirculation bubble above the vertex at $t = 4.0$. This recirculation region develops in the region of adverse pressure gradient induced by the mainstream flow on the upper surface of the parabola. This recirculation zone continues to grow in both dimensions and, eventually, the instantaneous streamlines seem to run closer together on the upstream side of the bubble indicating a region of intense flow variation. This intense variation in velocity is the result of the recirculation region "blocking" the flow as fluid is deflected around the expanding recirculation zone. The motion continually focuses into a decreasing streamwise region until the separation singularity forms at $t_s = 4.752$ as illustrated by the distinctly-formed "spike" in figure 3.3(f). This spike prevents the boundary-layer flow from moving around the vertex and over the top surface and is the initiation of a boundary-layer

eruption where a subsequent viscous-inviscid interaction is inevitable.

A different perspective of this event is provided by figures 3.4(a) through 3.4(d) which illustrate the temporal development of the streamlines in computational coordinates, i.e. the finite domain resulting from transformations (2.51) and (2.52). Figures 3.4(a) and 3.4(b) illustrate that the recirculation zone of fluid develops on the surface of the airfoil at a time between $t = 3.6$ and $t = 3.8$. Figures 3.4(c) and 3.4(d) show the growth of the bubble.

Figures 3.5(a) through 3.5(c) illustrate the instantaneous streamline patterns near the vertex of the parabola by using an enlarged spatial scale. The fluid inside the bubble recirculates in a clockwise direction. In figure 3.5(a), the bubble is small and the fluid recirculates in an almost circular motion at $t = 4.0$. By $t = 4.4$, the bubble has grown in both dimensions and encapsulated more fluid which now recirculates in an oblong circular motion, as depicted in figure 3.5(b). Figure 3.5(c) shows that a separation singularity has formed on the upstream side of the bubble at $t_s = 4.752$. The recirculating fluid is now drawn into the "spike" and then returned back into the bubble. The singularity forms here as a consequence of attempting to impose the external pressure distribution for an indefinite period of time. At the stage shown in figure 3.5(c), a boundary-layer eruption will develop and the next stage can only be described using a new subset of the Navier-Stokes equations which permits an eruption of the boundary layer into the external flow.

As the angle of attack of the airfoil increases, the pressure gradient in the leading nose region increases causing the external flow speed to increase.

Separation can be expected in regions where a persistent adverse pressure gradient exists. Figure 3.6 shows the external pressure gradient distribution at selected times and, as indicated, the pressure gradient increases in the direction of flow to a maximum value and then decreases. The pressure gradient is favorable from the stagnation point to the vertex; initially it is also favorable all the way to downstream infinity ($\hat{s} = 1$). However, for times greater than about $t \approx 2$, a region of adverse pressure gradient occurs on the upper surface which expands and strengthens with increasing time.

Figure 3.7 displays the surface shear stress distribution at selected times. It may be noted that the surface shear remains regular as $t \to t_s$ near the streamwise coordinate $\hat{s}_s = 0.60$, where the singularity develops; this is consistent with the theory of Van Dommelen (Peridier, 1989). An enlarged plot of the surface shear at t_s shows that the distribution is well-behaved near $\hat{s}_s$. Figure 3.7 indicates that the surface shear stress becomes zero at a time between $t = 3.6$ and $t = 3.8$; negative wall shear $\tau_w < 0$ signifies a region of recirculation, and this is in agreement with the instantaneous streamline plots in figures 3.4(a) and 3.4(b).

Figure 3.8 shows the temporal development of the normal perturbation $\tilde{A}(\hat{s},t)$. As time increases, $\tilde{A}$ increases, especially above the upper surface near the vertex region where separation ultimately develops. Note that the distribution focuses into a narrow streamwise band as t increases. As $t \to t_s$, $\tilde{A}$ increases explosively and becomes singular at the streamwise coordinate $\hat{s}_s = 0.60$. Since $v_1 = -\partial\tilde{A}/\partial s$, the implication of this is that separation induces a normal perturbation velocity which is alternately large and positive,

rather than large and negative, which is a behavior characteristic of a strongly focussed violent eruption. The "spike-like" development in the normal perturbation distribution is an indication of the separation singularity.

Figure 3.9 illustrates the constant vorticity contours in Cartesian coordinates at $t = t_s = 4.752$. Note that the vorticity is concentrated into a "spike" as the boundary layer starts to erupt into the outer flow. The structure of the vorticity contours is better shown using figures plotted in computational coordinates which is shown is shown in figures 3.10(a) through 3.10(e). All contours begin and end on the surface of the airfoil. The vorticity is negative everywhere in the flow field when the flow is impulsively started at $t = 0$. This is still the case at times t=2.0 and $t = 3.0$ as shown in figures 3.10(a) and 3.10(b). At $t = 3.0$, constant contours of vorticity approach each other near $\hat{s} = 0.75$; figure 3.10(b) illustrates that two contours with the same letter (A, B or C) are equal in value. Contours A, B, C are all negative in magnitude. It is observed that two contour lines (labeled C) of equal value $\omega = -0.73$ connect together at $\hat{s} = 0.76$ and $\hat{\zeta} = 0.11$. At $t = 4.0$, a zero vorticity contour line is present for the first time bounding a small zone of positive vorticity; this is associated with the development of the vortex and is labeled in figure 3.10(c). The presence of a zero vorticity line is one of the MRS conditions necessary for separation. The vorticity between the surface and the $\omega = 0$ contour is positive. The vorticity elsewhere is negative. The constant vorticity contours of $\omega = -0.59$ connect at $\hat{s} = 0.81$ and $\hat{\zeta} = 0.27$. Figure 3.10(d) shows that the region of positive vorticity has increased in size and deformed with the passage of time. The constant vorticity contours of

ω = -0.56 connect at $\hat{s} = 0.83$ and $\hat{\zeta} = 0.31$. Figure 3.10(e) illustrates the contours at $t_s = 4.752$ and the concentration of vorticity into a spike. The constant vorticity contours of ω = -0.54 connect at $\hat{s} = 0.84$ and $\hat{\zeta} = 0.33$.

Figure 3.11 illustrates the temporal development of the distribution of the external velocity U_∞. It is seen that U_∞ increases as time increases and that the maximum value shifts towards $\hat{s} = 0.5$, the vertex of the parabola. As discussed previously in section 2.2.1, the point of maximum velocity shifts towards the nose with an increasing angle of attack, and for fixed t, the mainstream velocity decreases monotonically on the upper surface for all points beyond the maximum point.

Figure 3.12 illustrates the temporal development of the velocity u profiles at specific $\hat{s}$ locations in the boundary layer. Figure 3.12(a) shows the u profiles at $\hat{s} = 0.30$, which is a station on the lower surface of the parabola. Figure 3.12(b) shows the u profiles at $\hat{s} = 0.4$, a point on the lower surface that is closer to the vertex. Figure 3.12(c) illustrates the profiles at $\hat{s} = 0.5$, the vertex while figure 3.12(d) illustrates the u profiles at $\hat{s} = 0.6$, a point on the upper surface. Note that for all these situations, the motion is accelerating at the mainstream and the motion is always in the direction of increasing $\hat{s}$. At times t = 4.0 and 4.4, it is seen that the profiles are changing form near the wall. Figure 3.12(e) shows the u profiles at $\hat{s} = 0.65$, which is a station located midway through the recirculation zone that develops on the parabola at the higher angles of attack. At times t = 4.0 and 4.4, the u profiles actually become negative near the surface indicating a region of reversed flow. It is also worthwhile to note that these profiles change curvature in the upper

portion of the boundary layer, and therefore, exhibit an inflection point midway through the boundary layer. Inflectional points are often associated with instability in boundary layers. However, there was no evidence of instability in the present calculation for any of the mesh sizes considered. Comparing plot 3.12(e) to figure 3.4(c), it is seen that $\hat{s} = 0.65$ is located in the bubble illustrated in the instantaneous streamline patterns. Figure 3.12(f) also shows reversed flow at $\hat{s} = 0.7$ for $t = 4.0$ and 4.4, but it is not as pronounced. This streamwise position is nearer to the downstream side of the recirculation bubble. Figure 3.12(g) shows the u profiles at $\hat{s} = 0.8$, a position farther downstream on the upper surface and out of the recirculation region.

Figures 3.13(a) and 3.13(b) show the constant contours of velocity U from the Lagrangian results in computational coordinates at $t = 2.4$ and $t = 4.4$, respectively. The contours are smooth everywhere for all t. Also, as $t \rightarrow t_S = 4.752$, the velocity of the singularity is almost zero, $U_S = 0.00037$. This indicates that the singularity remains stationary and does not move along the surface; this is similar to the singularity behavior observed in the case of an airfoil impulsively pitched to a constant angle of attack (Degani et al, 1994).

In summary, the pertinent features and results of the boundary-layer analysis in the nose region of a parabola as the angle of attack increases proportionally to $A(t) = t$ are as follows:

1) The Lagrangian calculation is started at $t_0 = 2.0$ and remeshed at $t = 2.8$, 3.4, 3.8, 4.1, and 4.5.

2) A zone of recirculating fluid develops on the downstream side of the parabola's vertex between $t = 3.6$ and $t = 3.8$.

3) A separation singularity develops at $t = t_s = 4.752$ and is represented as a "spike."

4) The vorticity and normal perturbation velocity are concentrated into a "spike-like" region at $t_s = 4.752$.

5) The surface shear stress remains regular as $t \to t_s$.

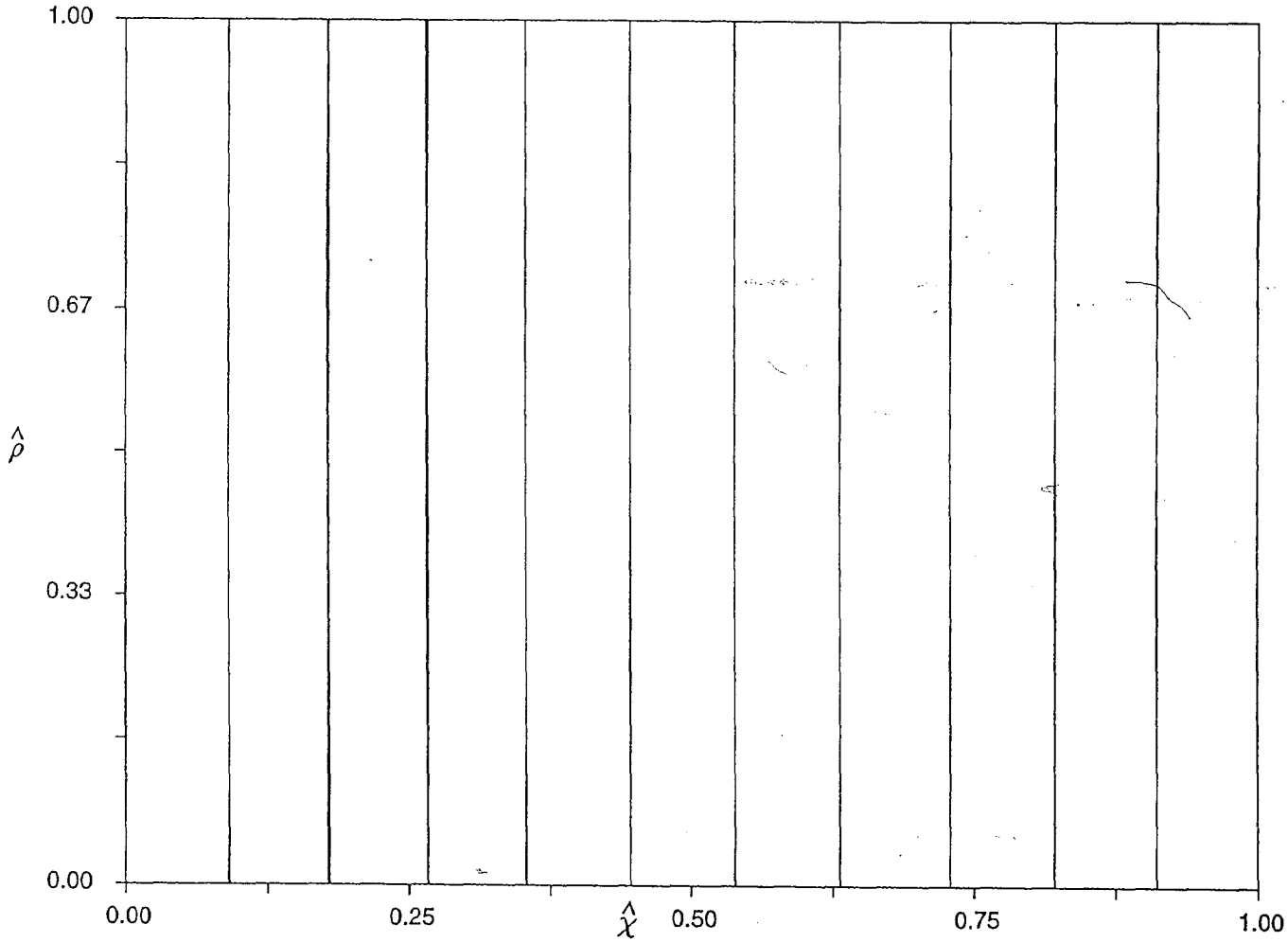

Figure 3.2 - The evolution of lines of constant $\hat{s}$ during lagrangian calculation for A(t) = t

3.2 (a) at t = 4.5, corresponding to the start of calculation after a remeshing

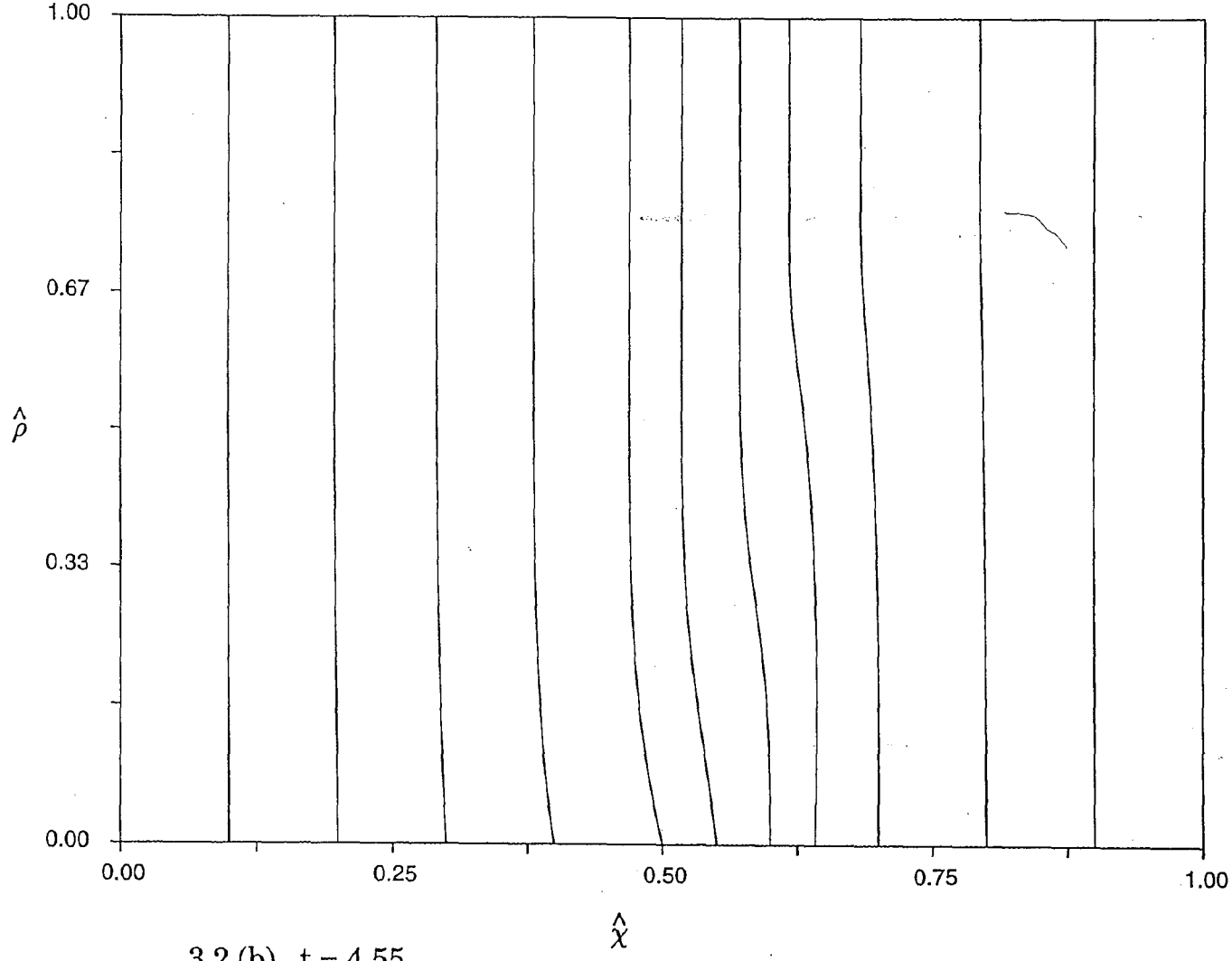

3.2 (b) t = 4.55

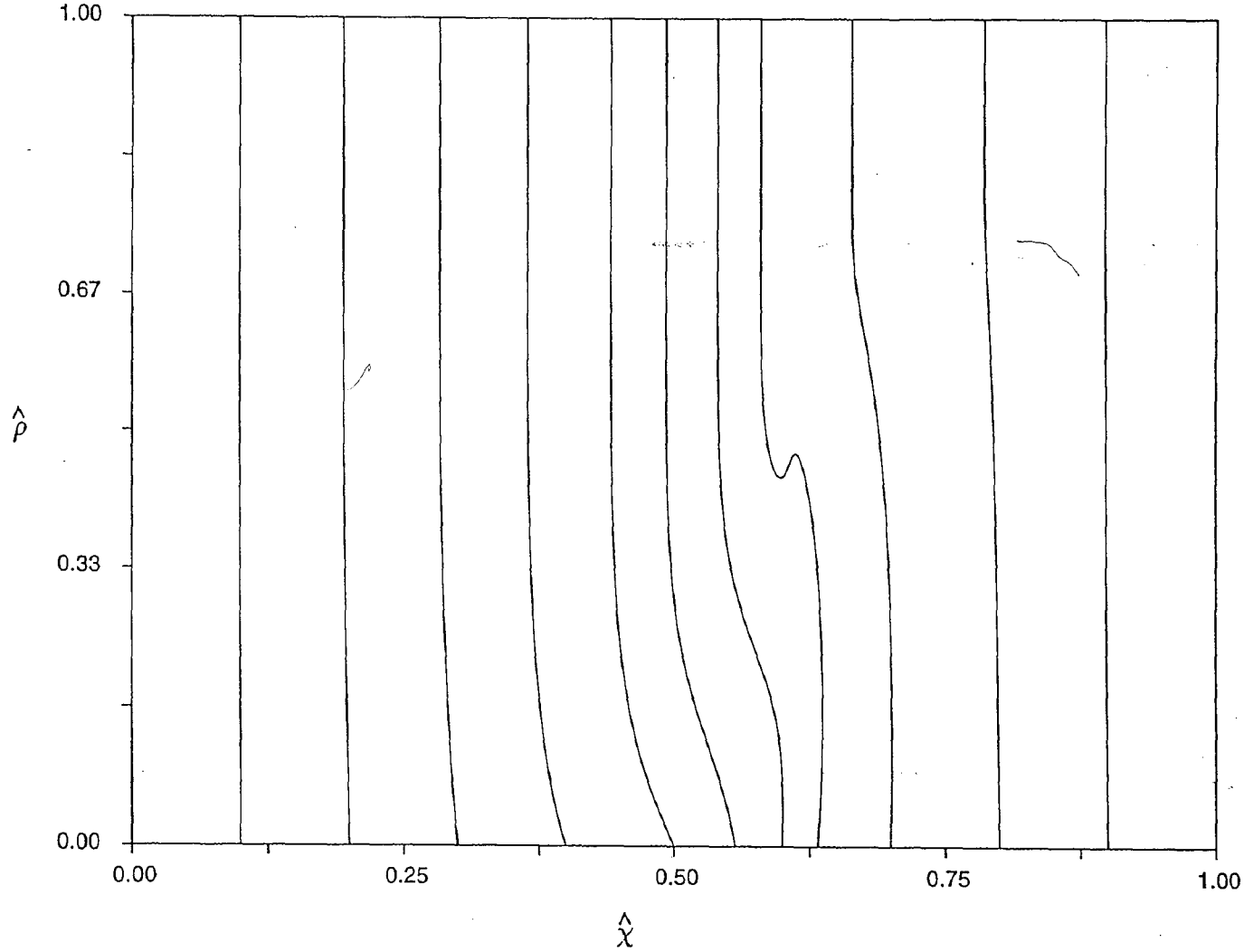

3.2 (c) t = 4.6

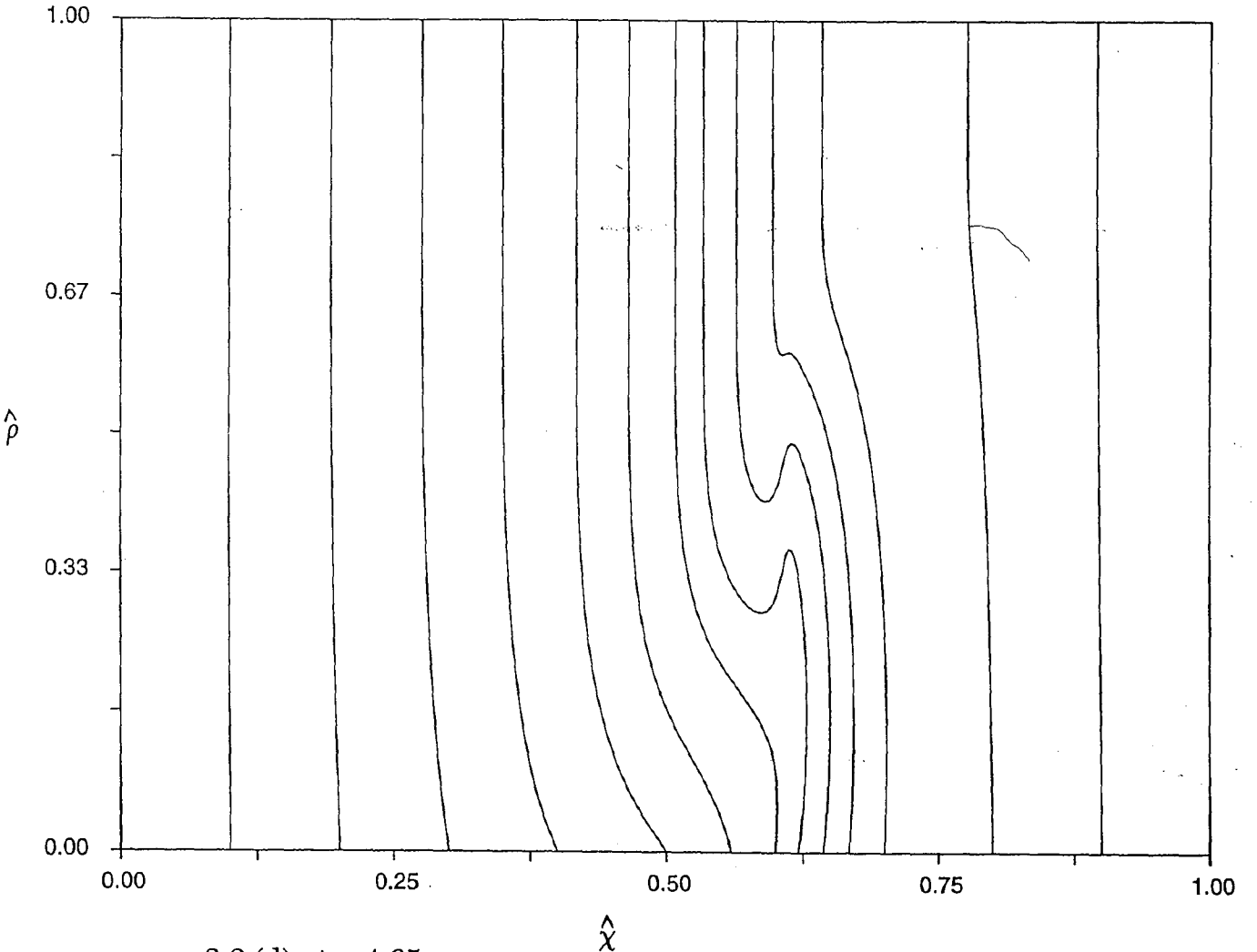

3.2 (d) t = 4.65

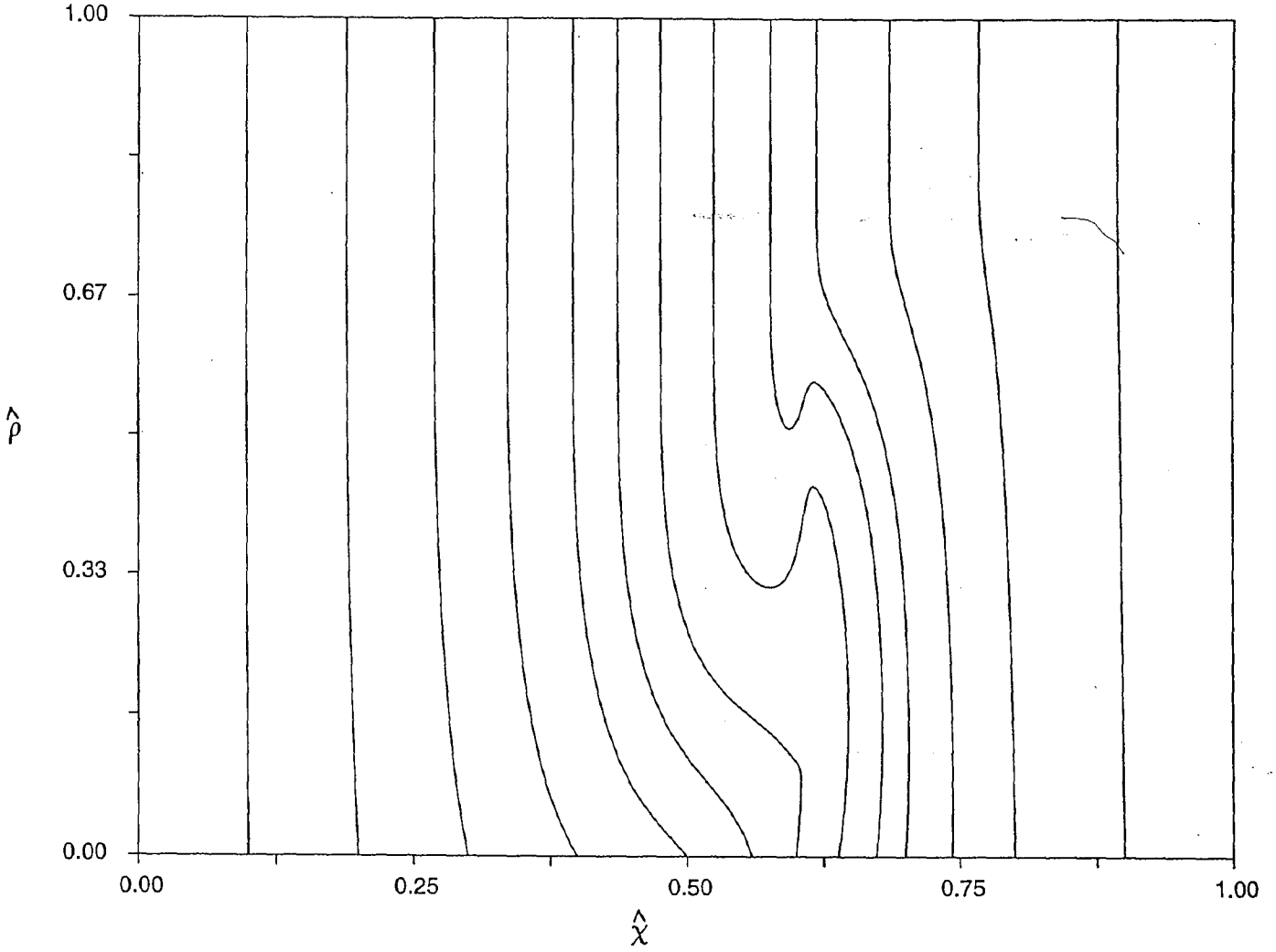

3.2 (e) t = 4.7

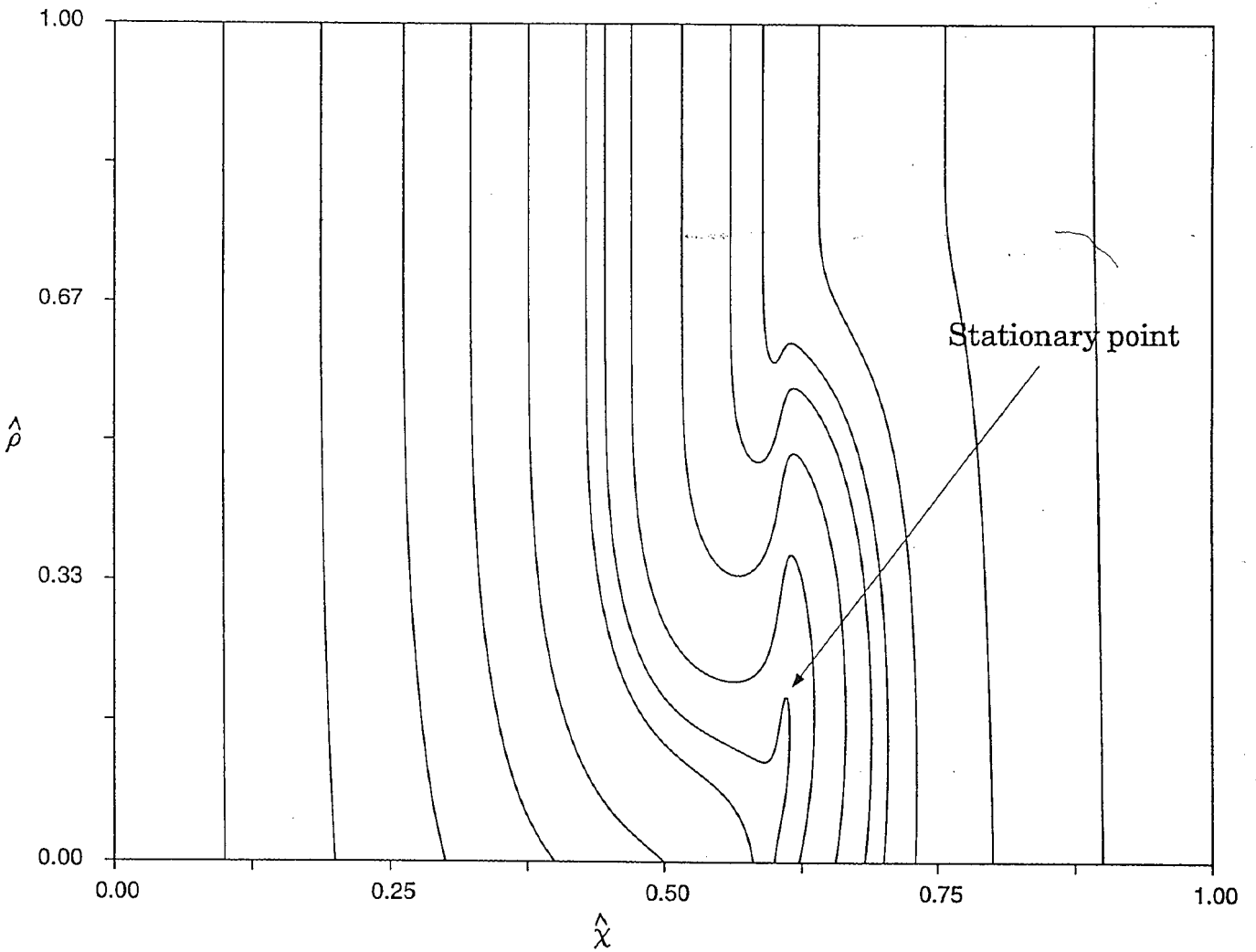
1.00
0.67
0.33
0.00
$\hat{\rho}$
0.00
0.25
0.50
0.75
1.00
$\hat{\chi}$
Stationary point

3.2 (f) $t = t_s = 4.752$

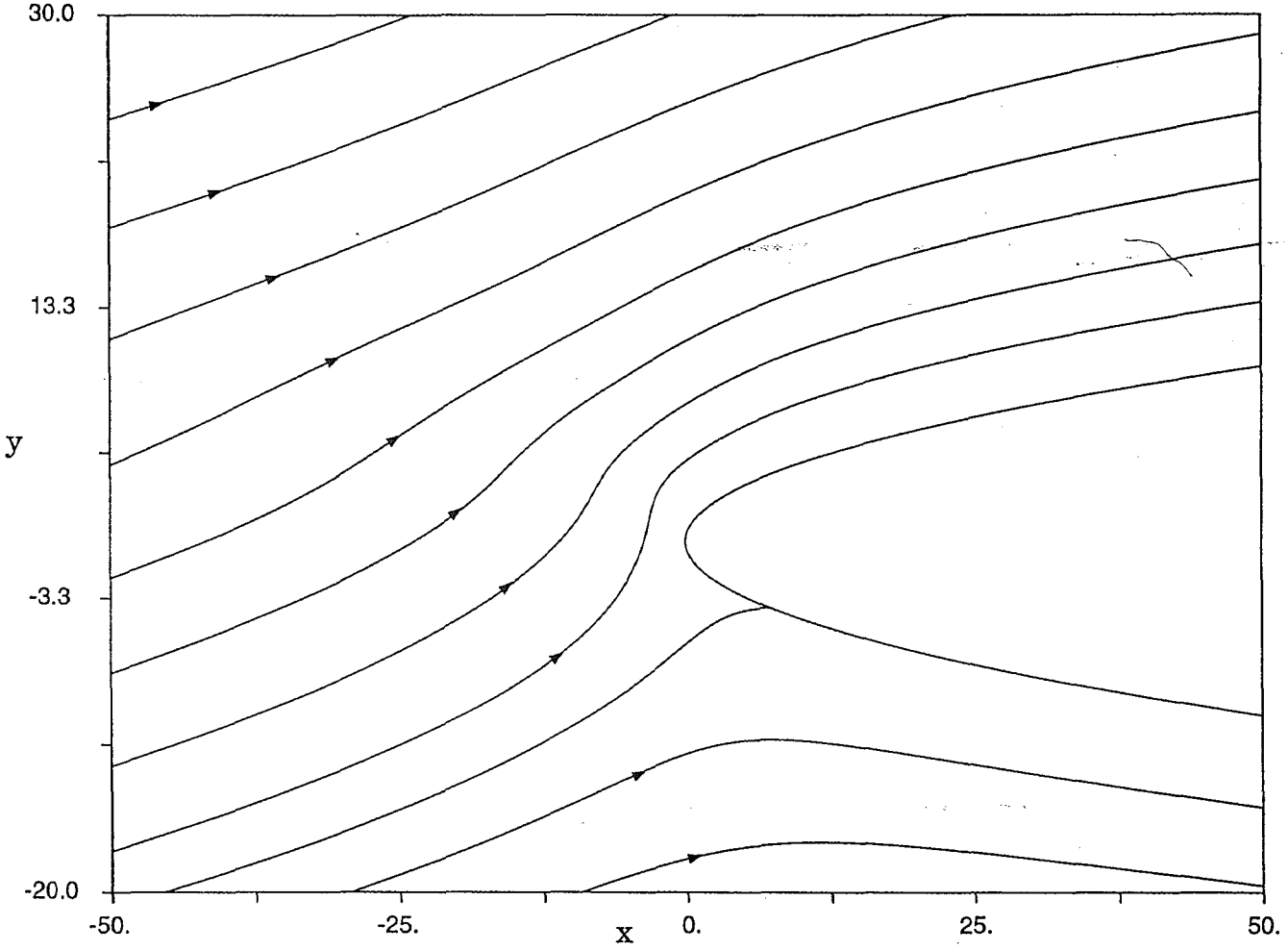

Figure 3.3 - Temporal development of the instantaneous streamline patterns for A(t) = t

3.3 (a) t = 2.0

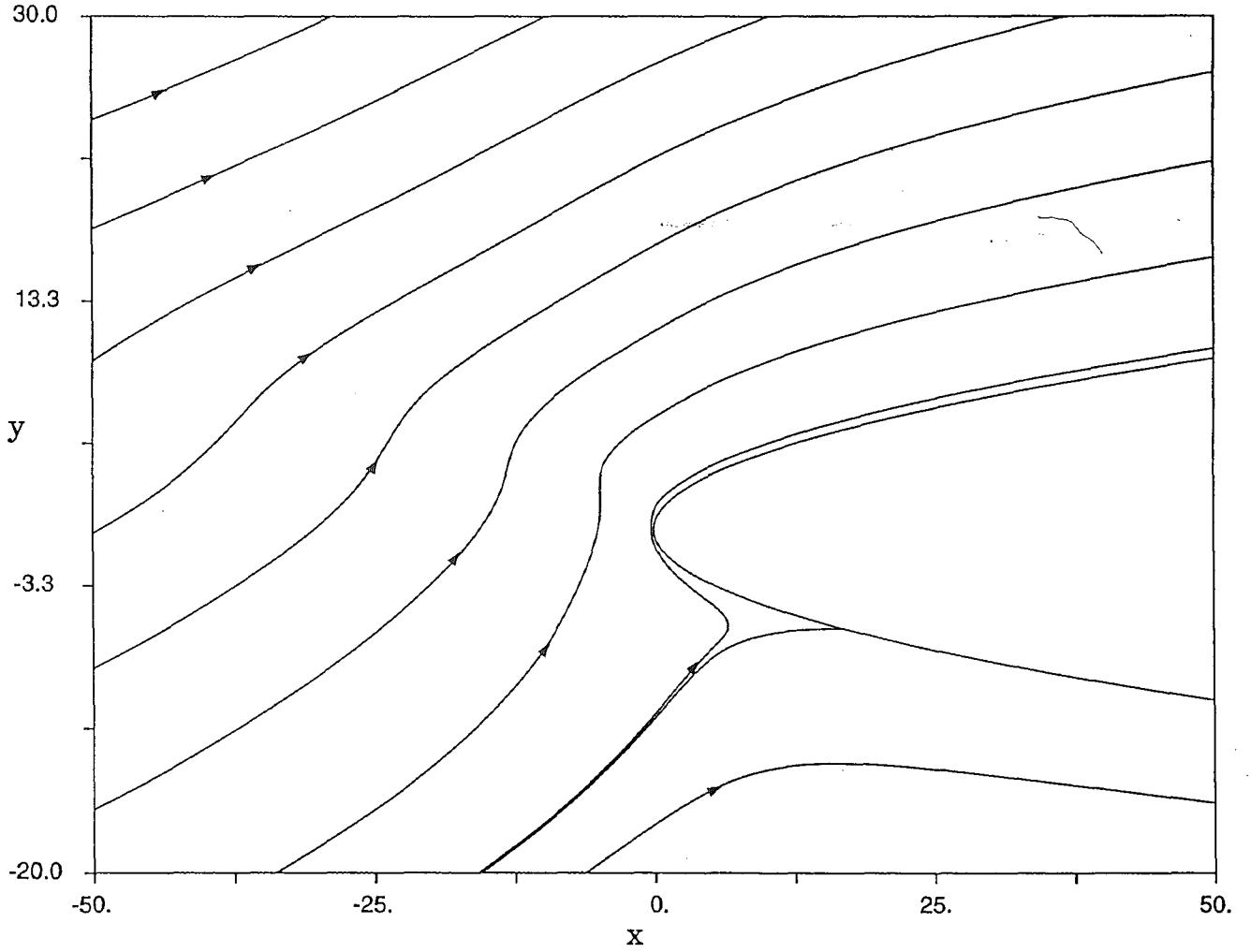

3.3 (b) t = 3.0

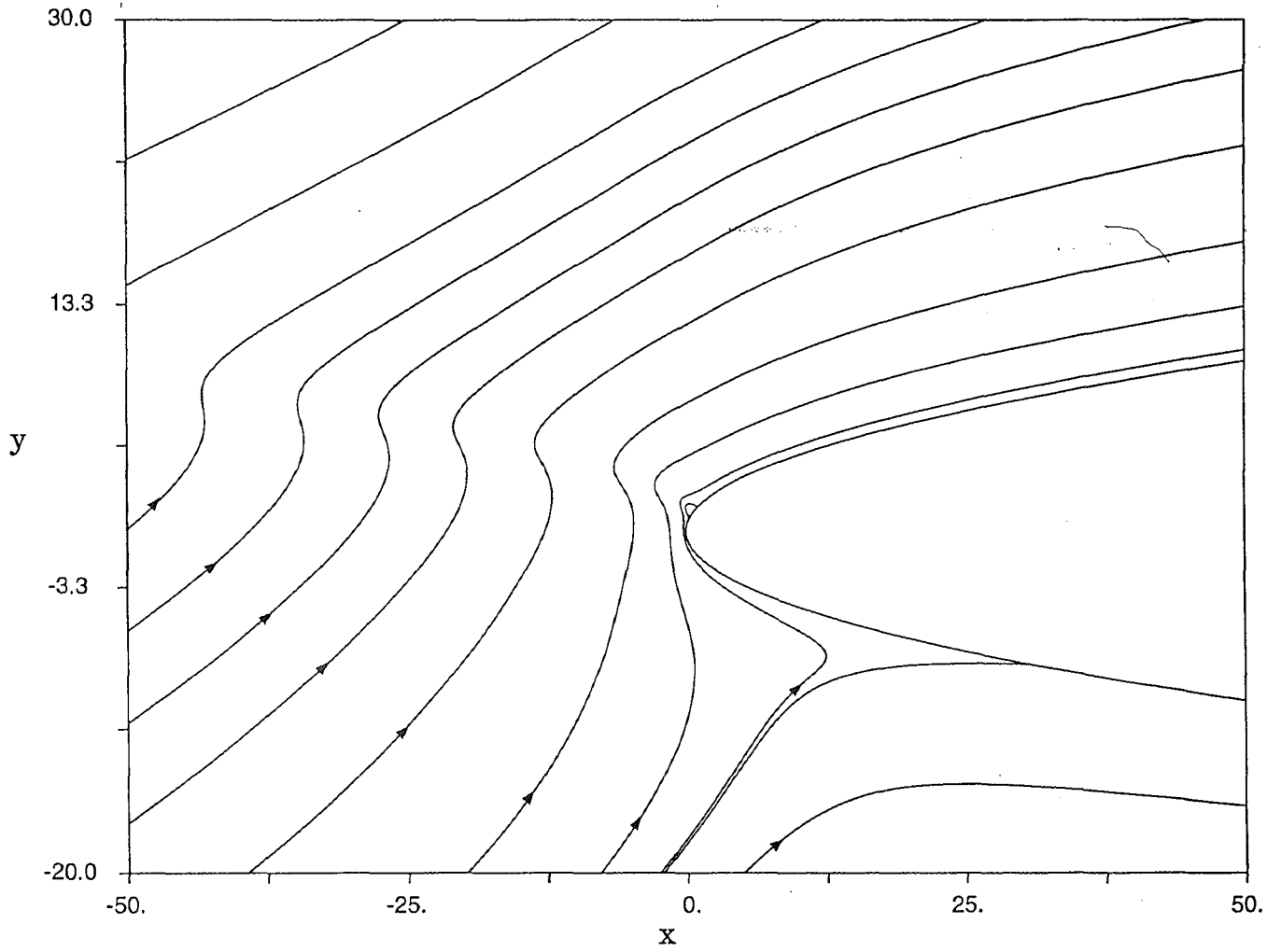

3.3 (c) t = 4.0

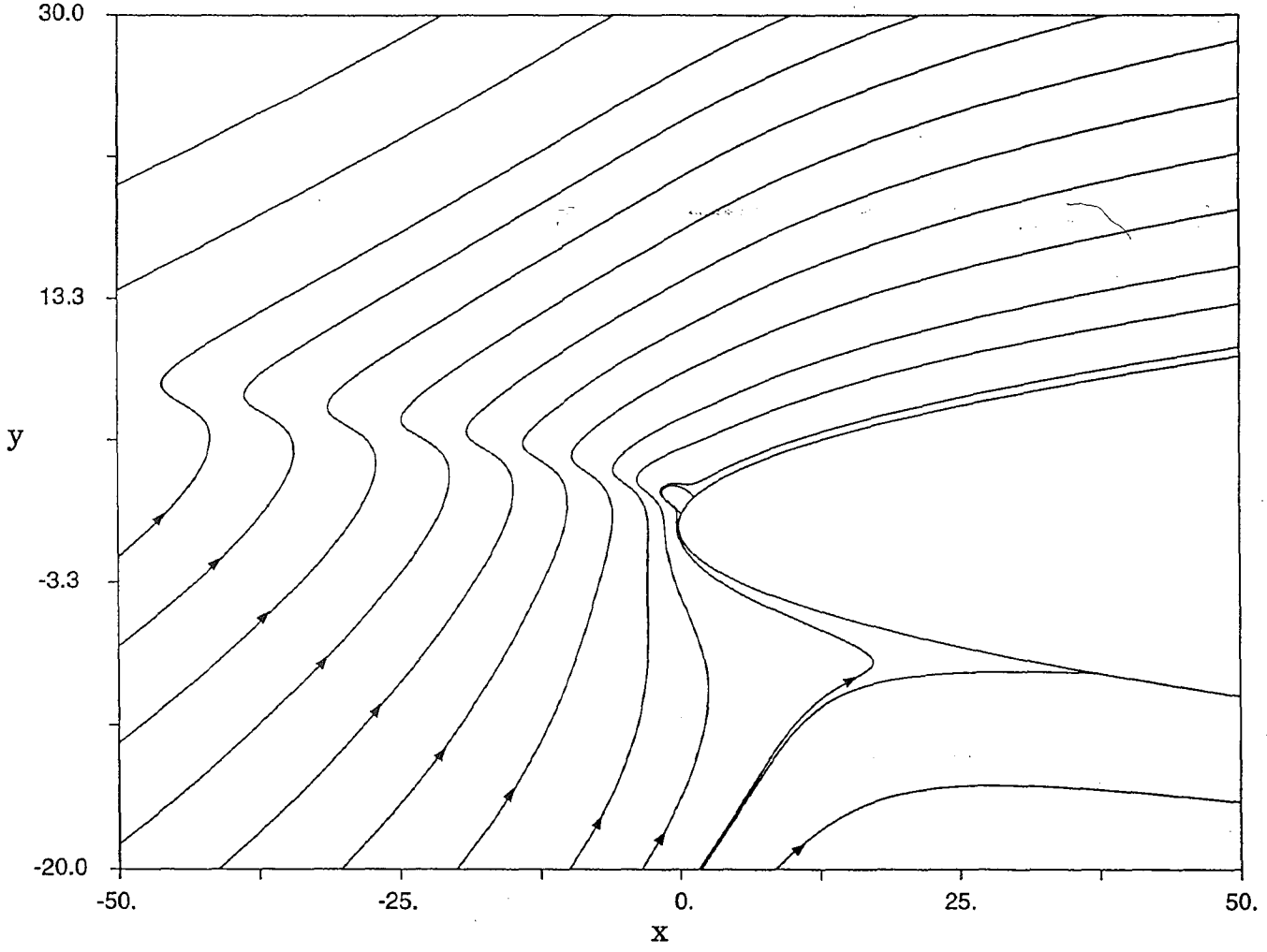

3.3 (d) t = 4.4

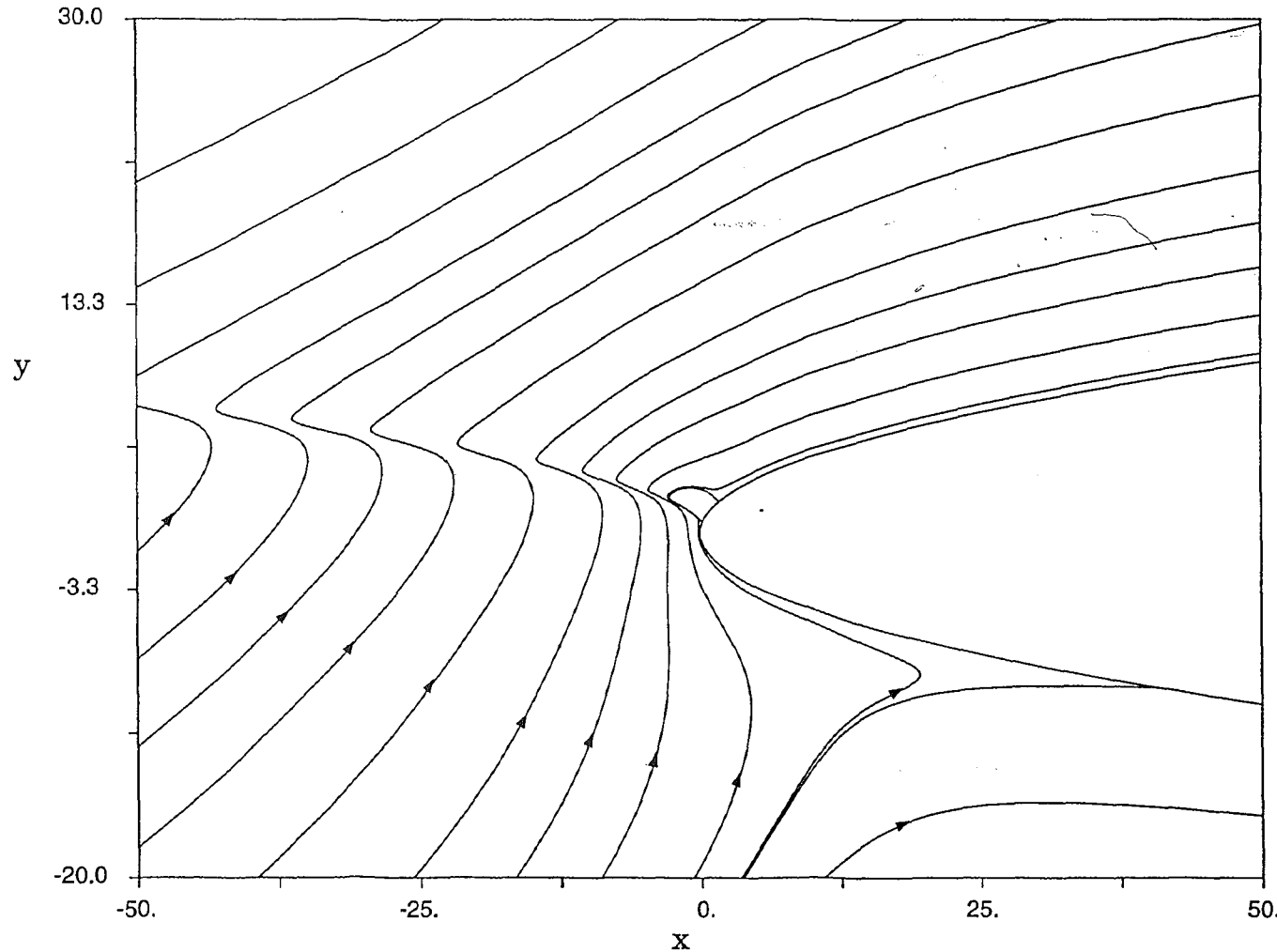

3.3 (e) t = 4.6

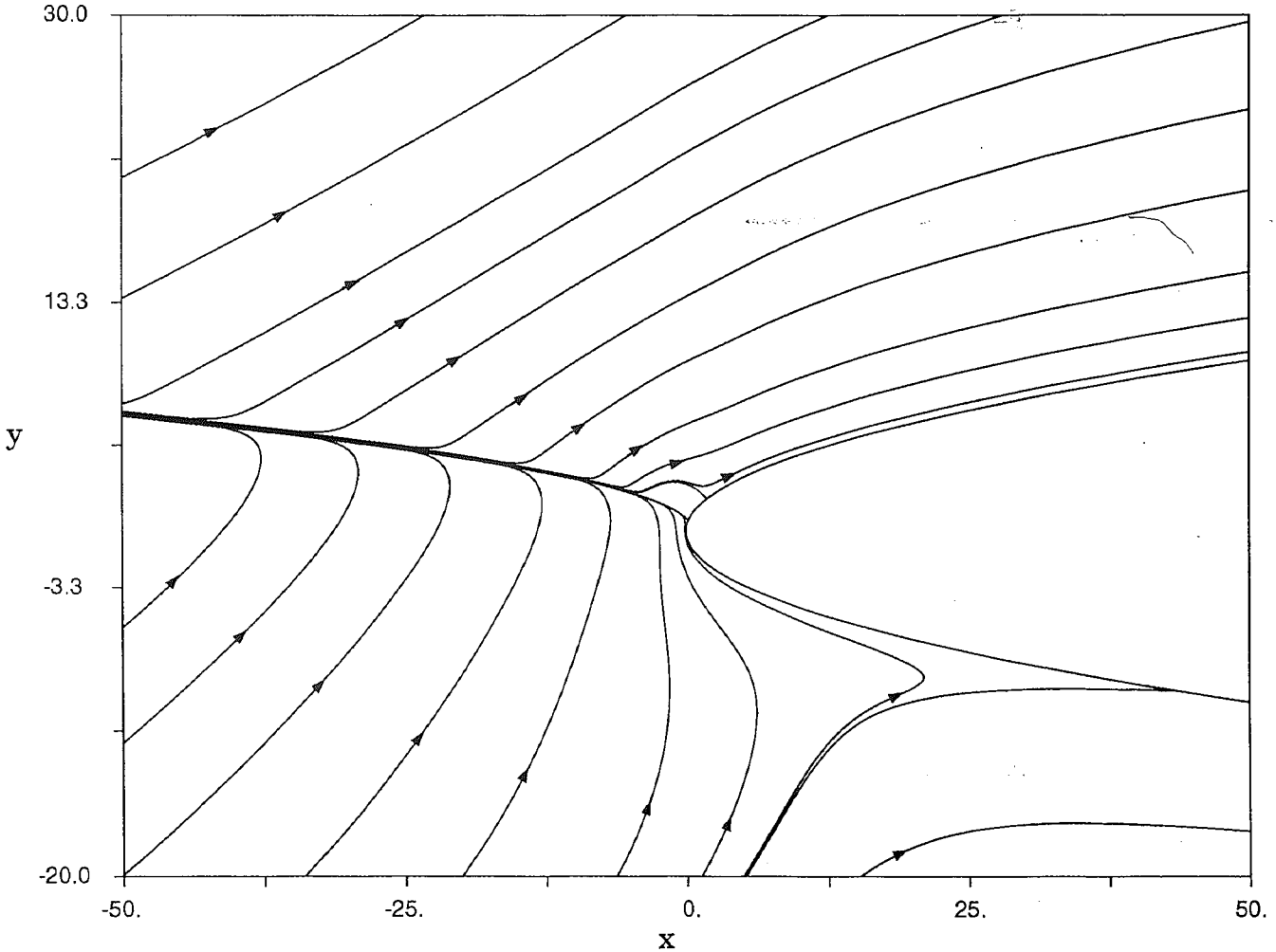

3.3 (f) $t = t_s = 4.752$

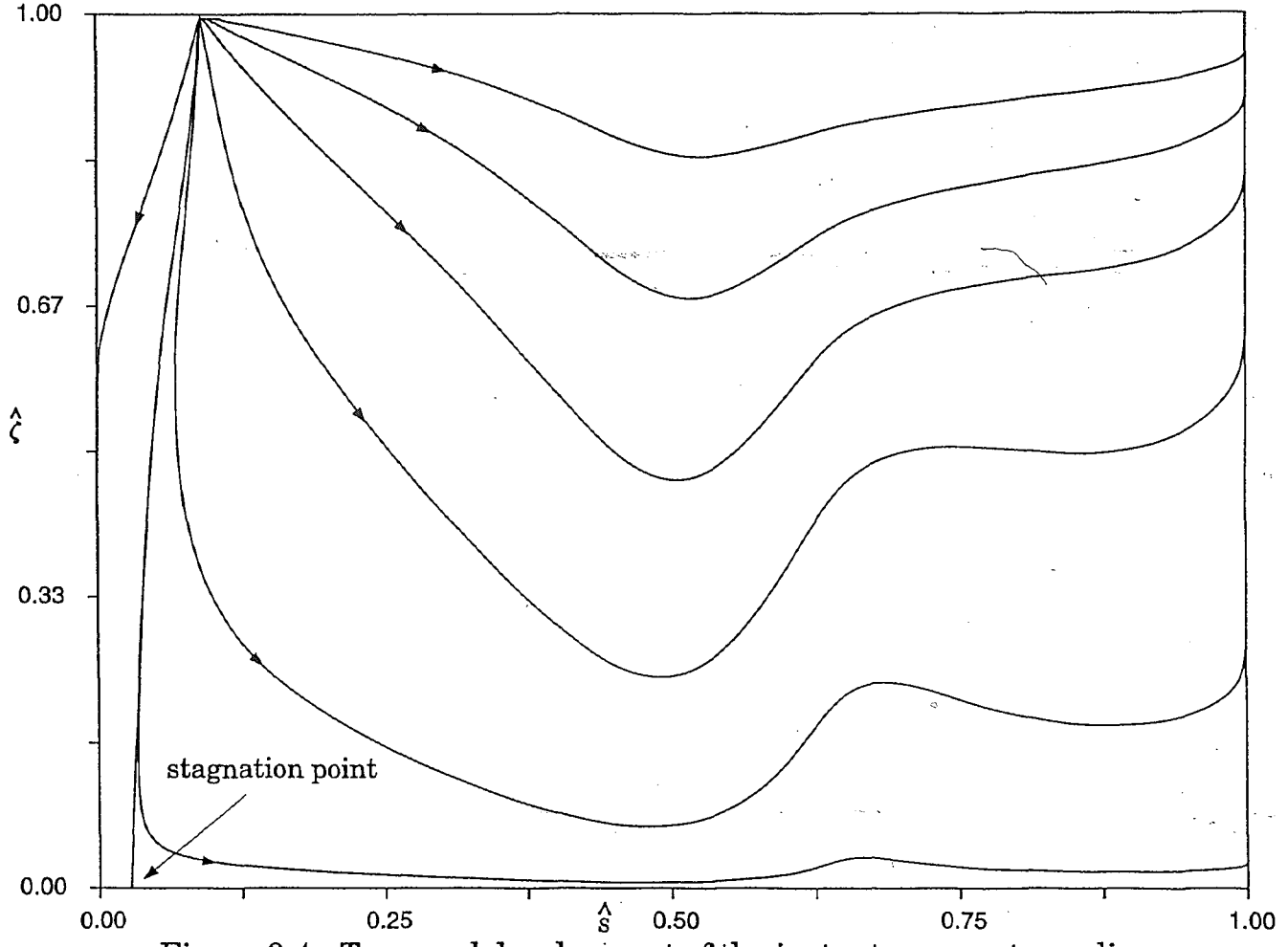

Figure 3.4 - Temporal development of the instantaneous streamline patterns in computational coordinates for A(t) = t

3.4 (a) t = 3.6

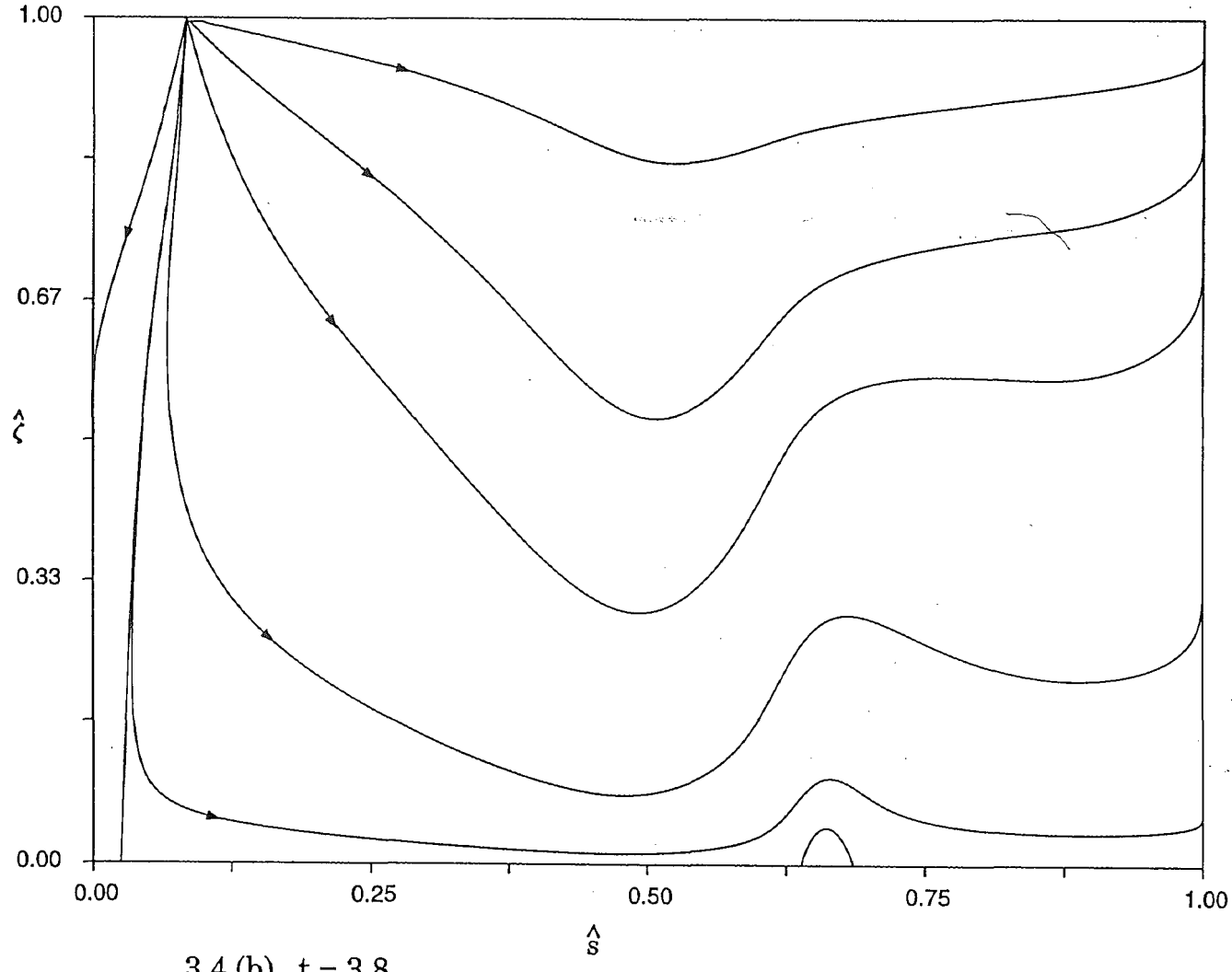

3.4 (b) t = 3.8

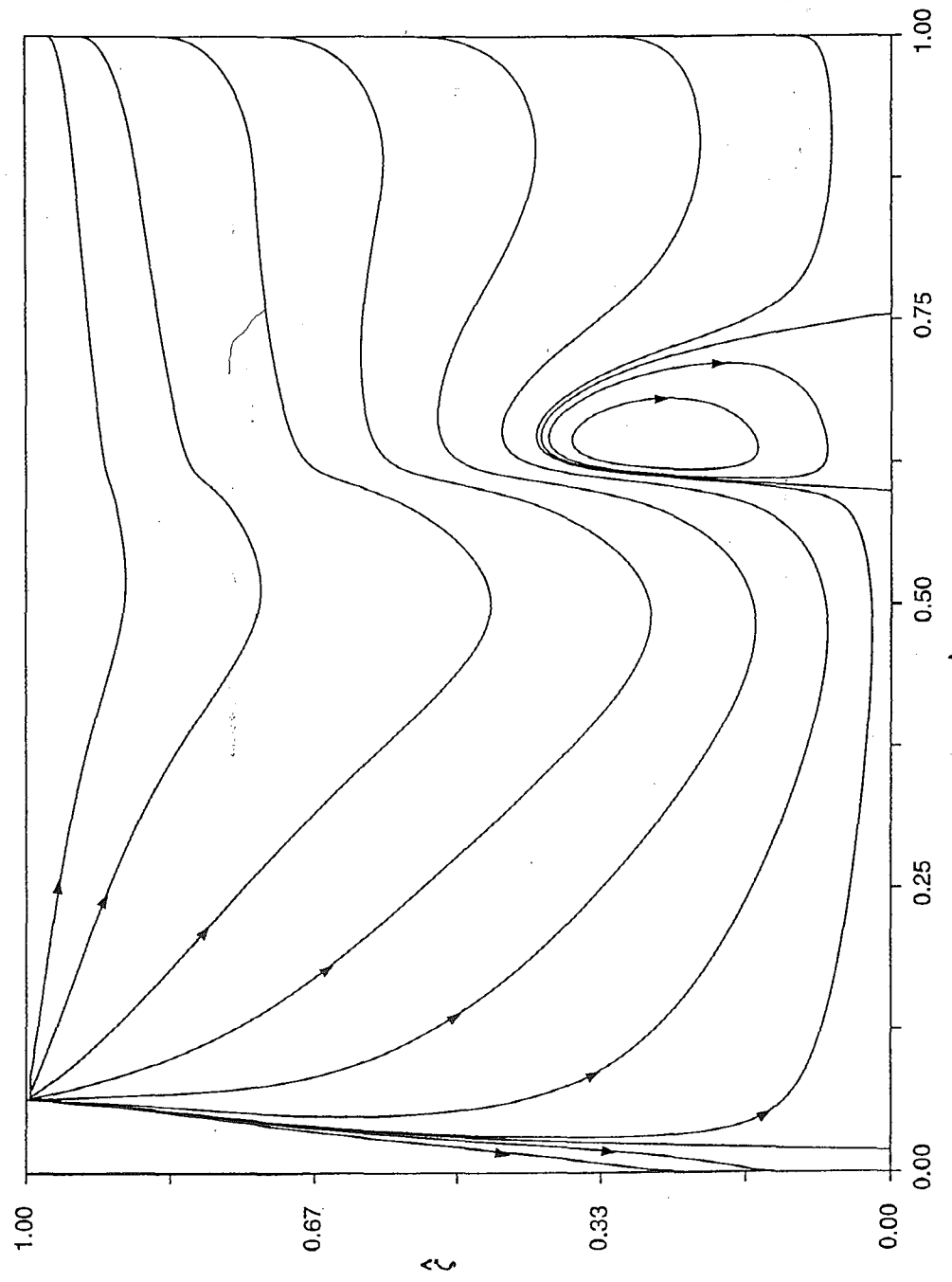

3.4 (c) $t = 4.4$

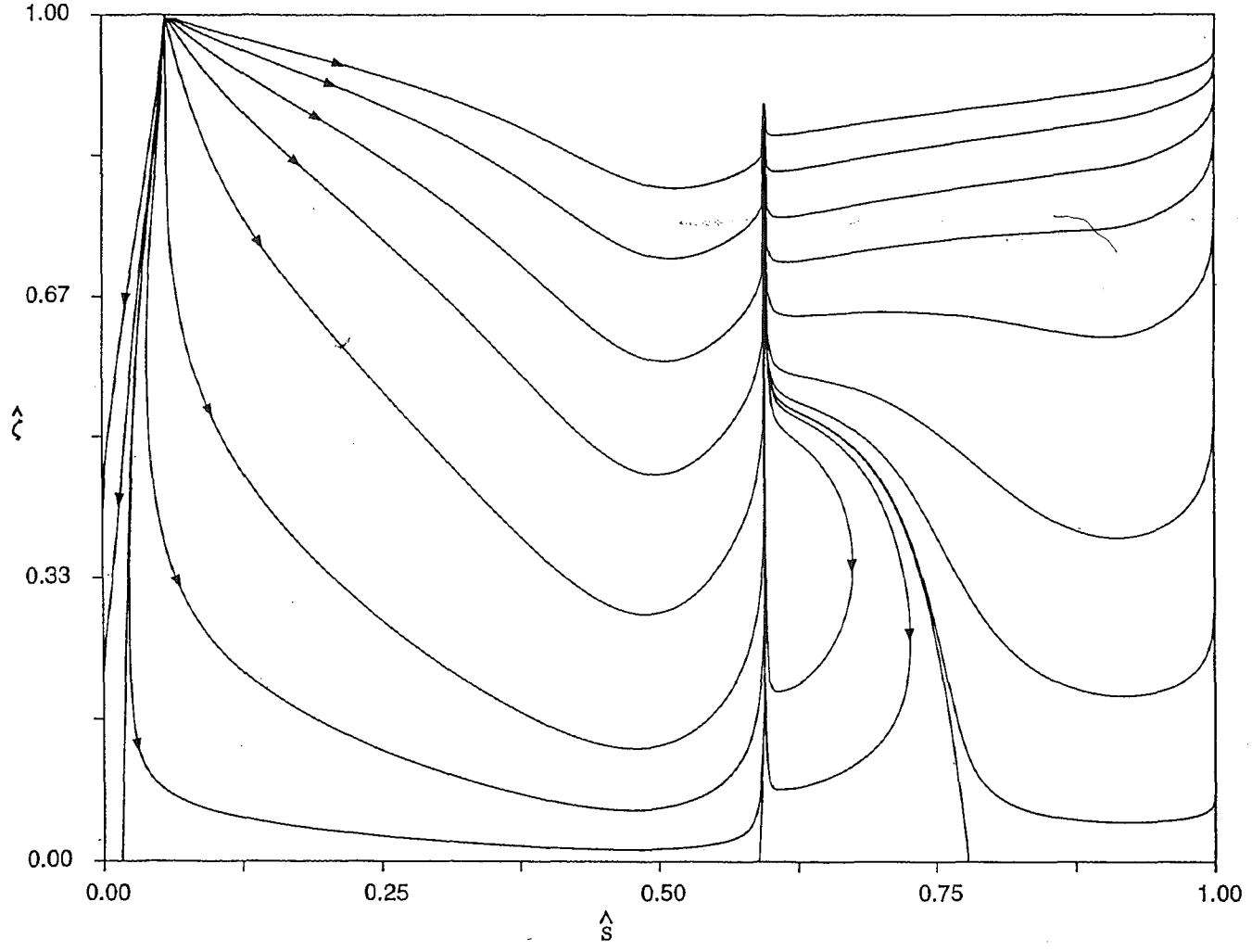

3.4 (d) $t = t_s = 4.752$

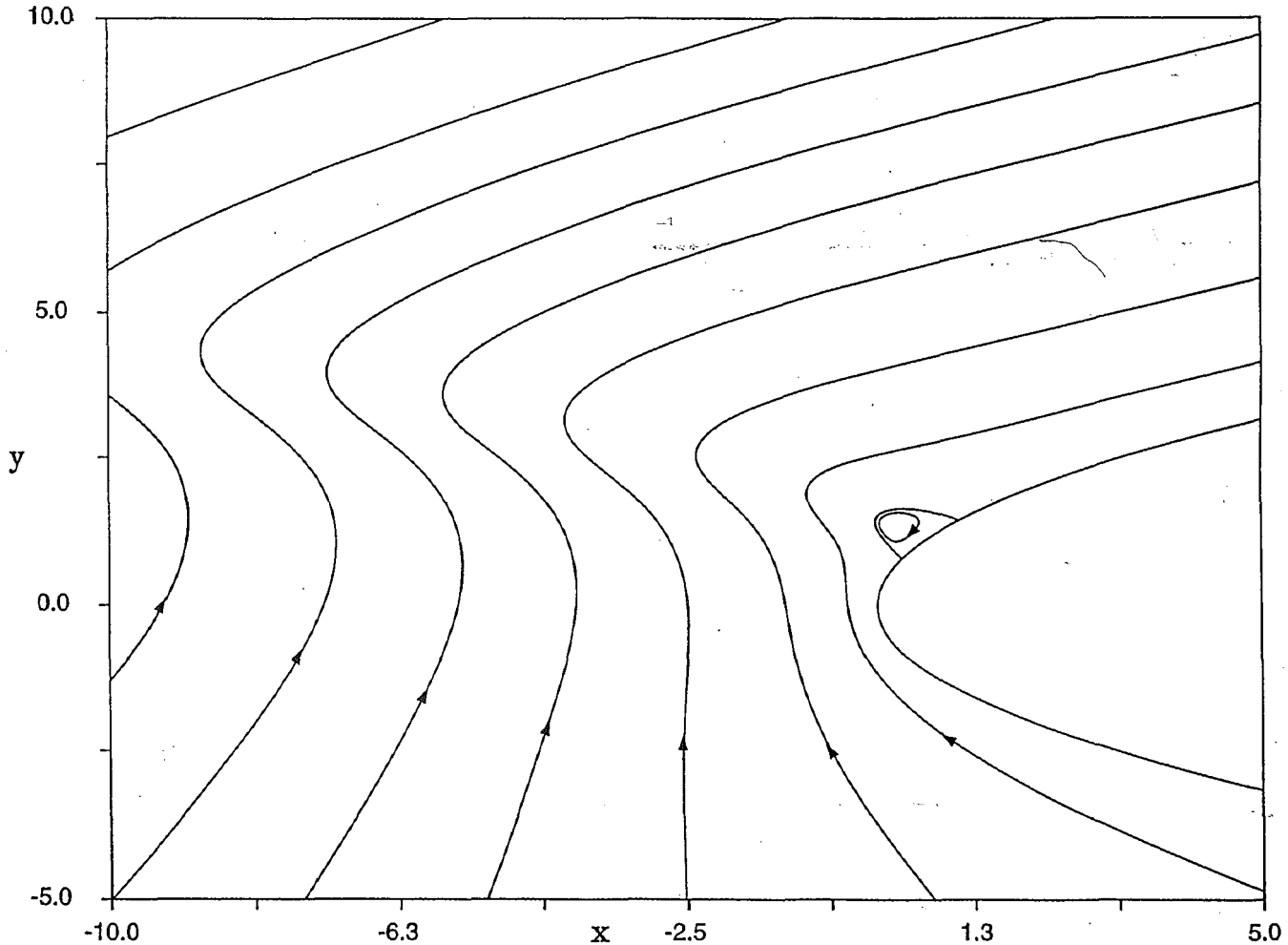

Figure 3.5 - Instantaneous streamlines using an enlarged scale near the parabola's vertex

3.5 (a) t = 4.0

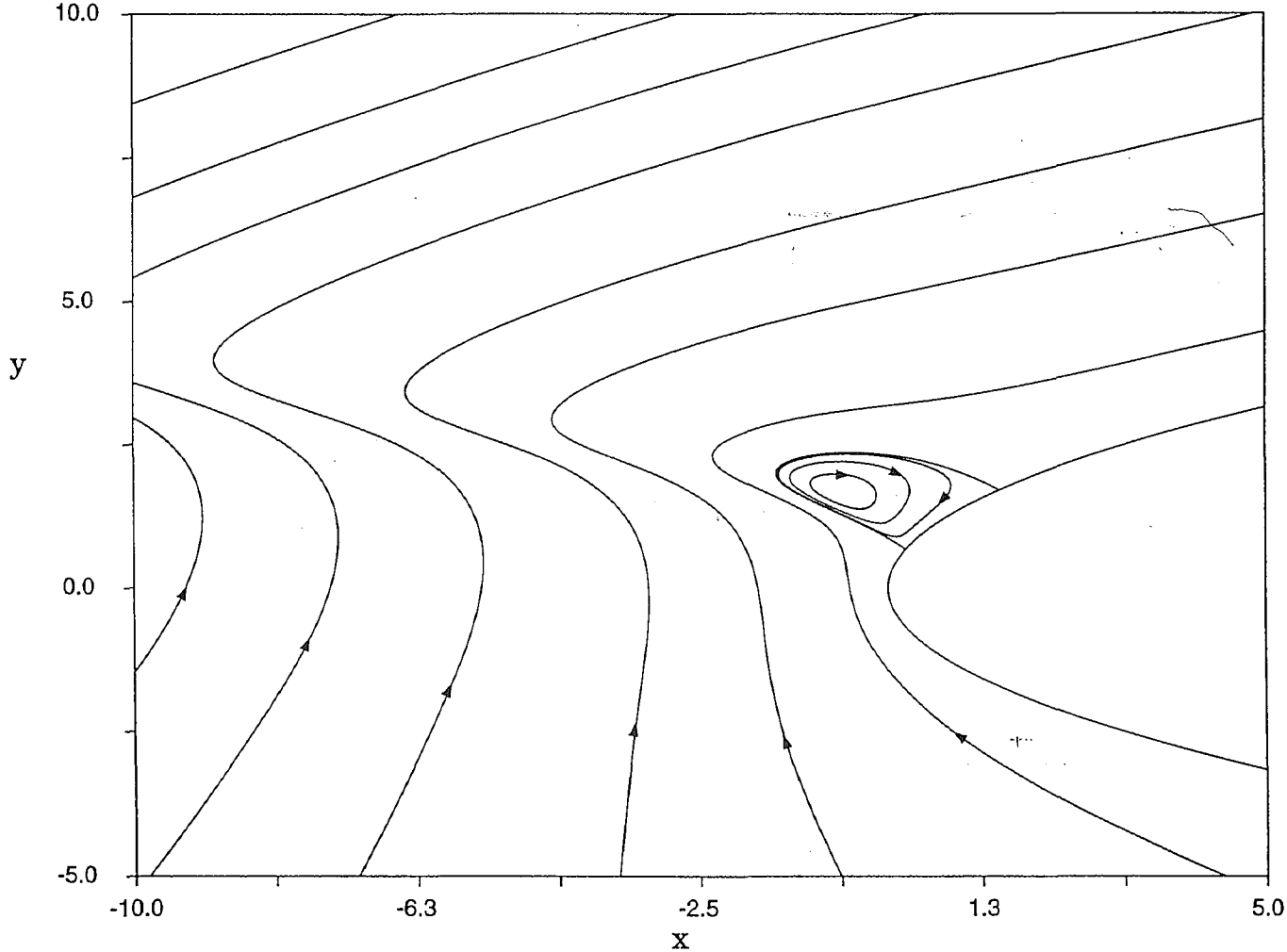

3.5 (b) t = 4.4

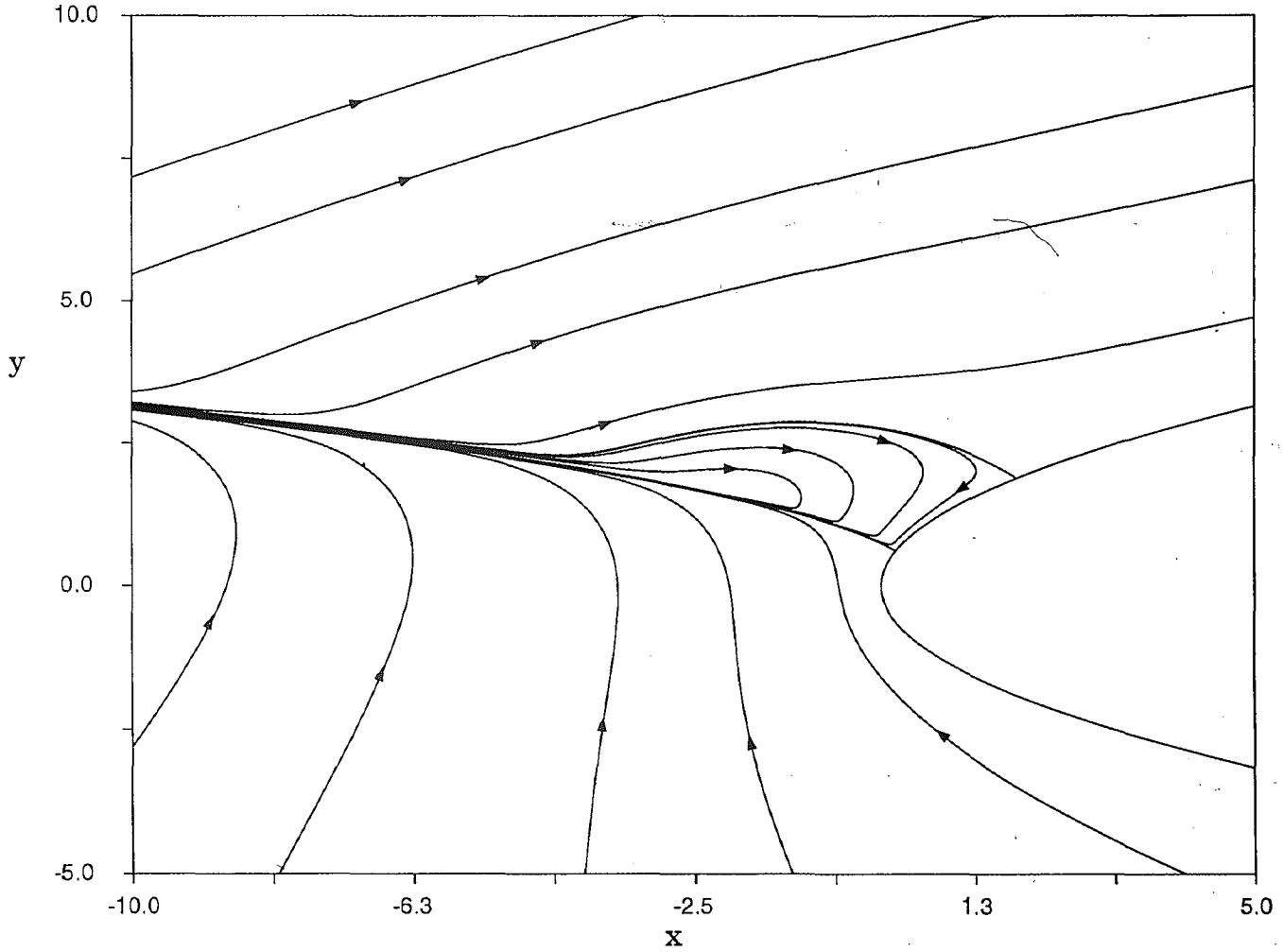

3.5 (c) $t = t_s = 4.752$

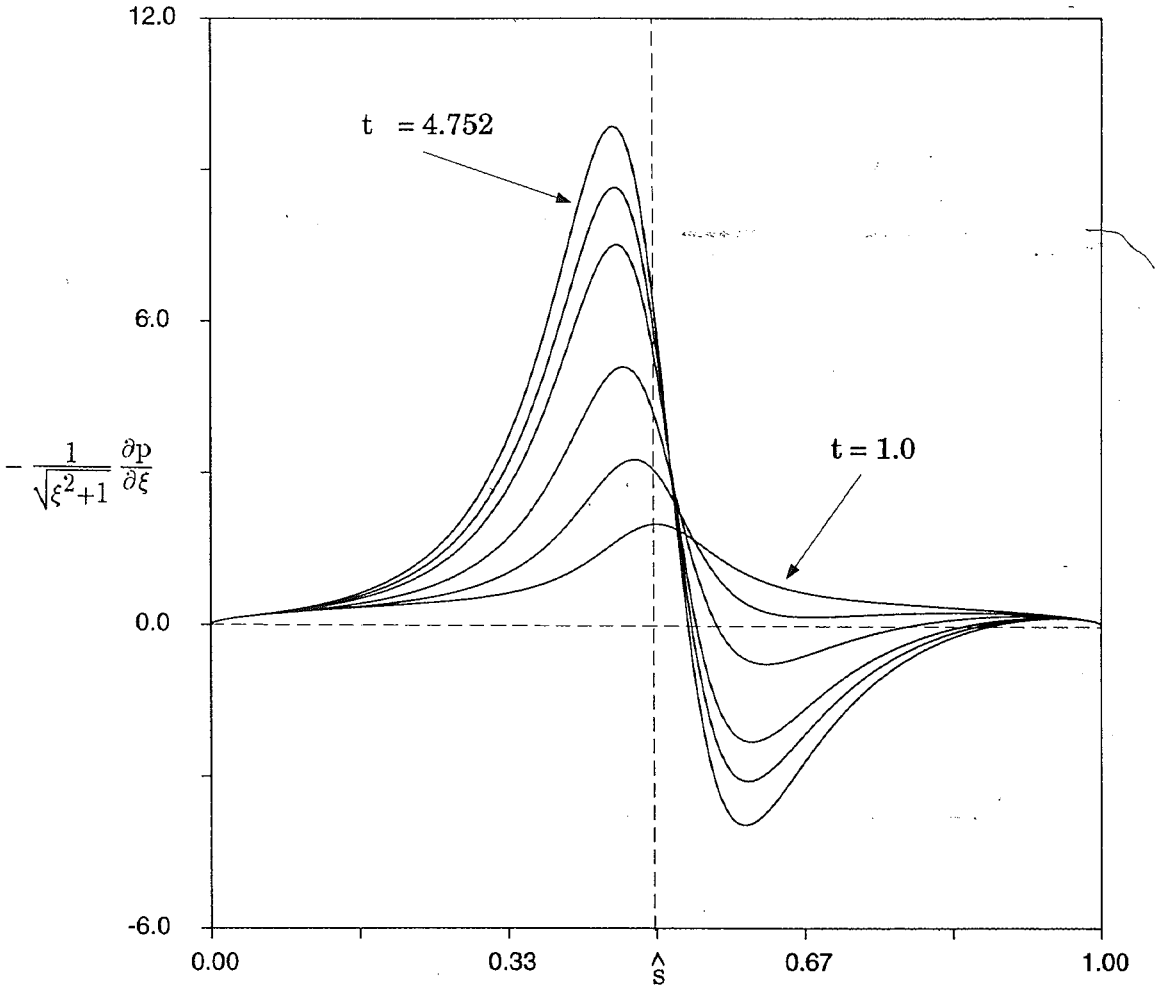

Figure 3.6 - External pressure gradient distribution at selected times:
t = 1.0, 2.0, 3.0, 4.0, 4.4, 4.752

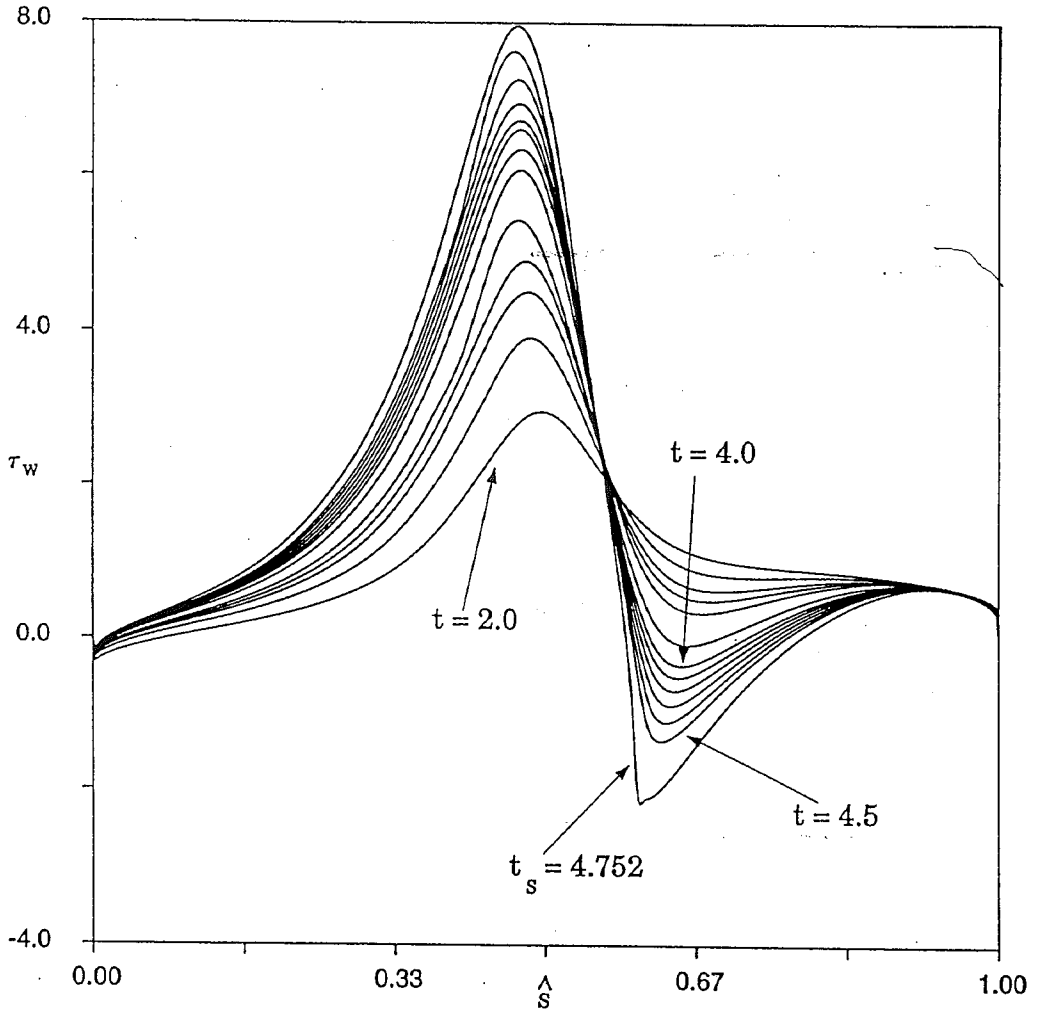

Figure 3.7 - Surface shear stress distribution at selected times :
t = 2.0, 2.6, 3.0, 3.2, 3.4, 3.8, 4.0 (0.1) 4.5, 4.752

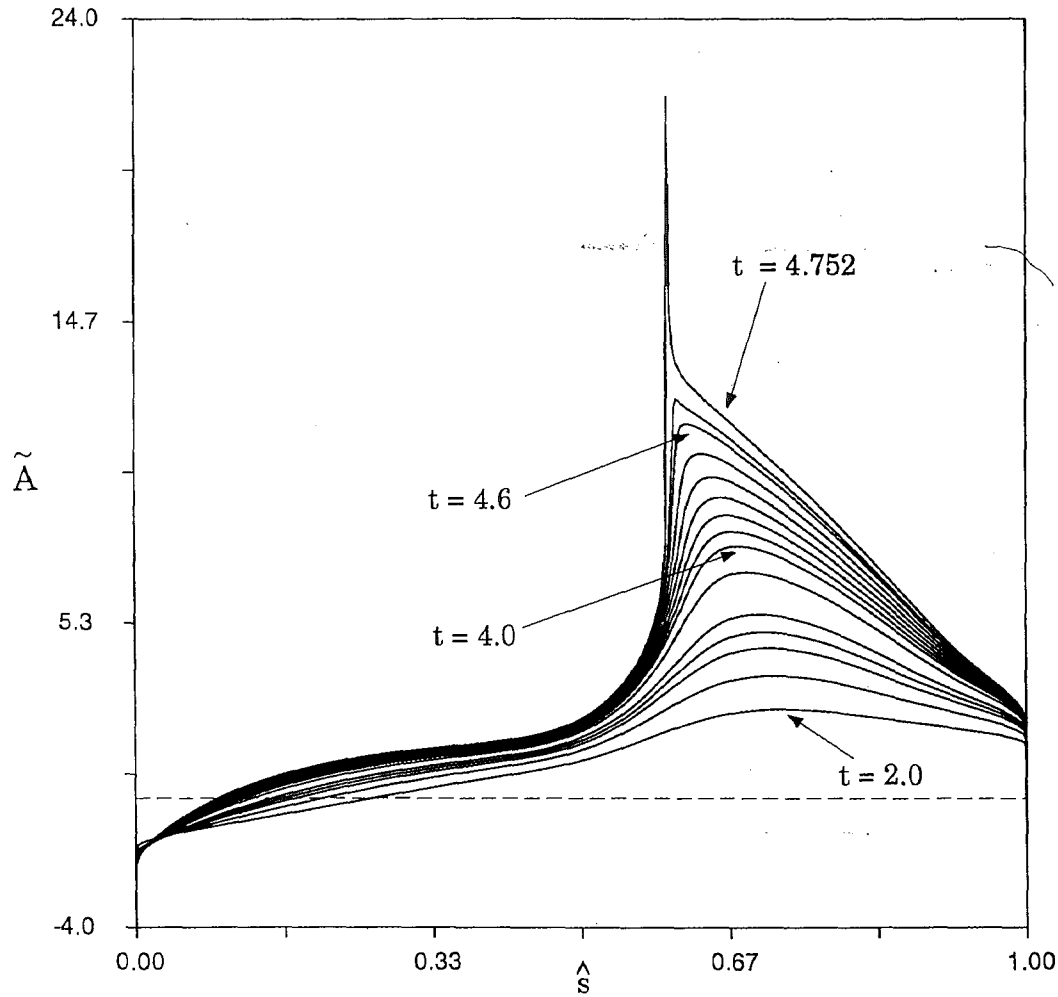

Figure 3.8 - Distribution of normal perturbation $\tilde{A}$ at selected times :
t = 2.0, 2.6, 3.0, 3.2, 3.4, 3.8, 4.0 (0.1) 4.6, 4.65, 4.752

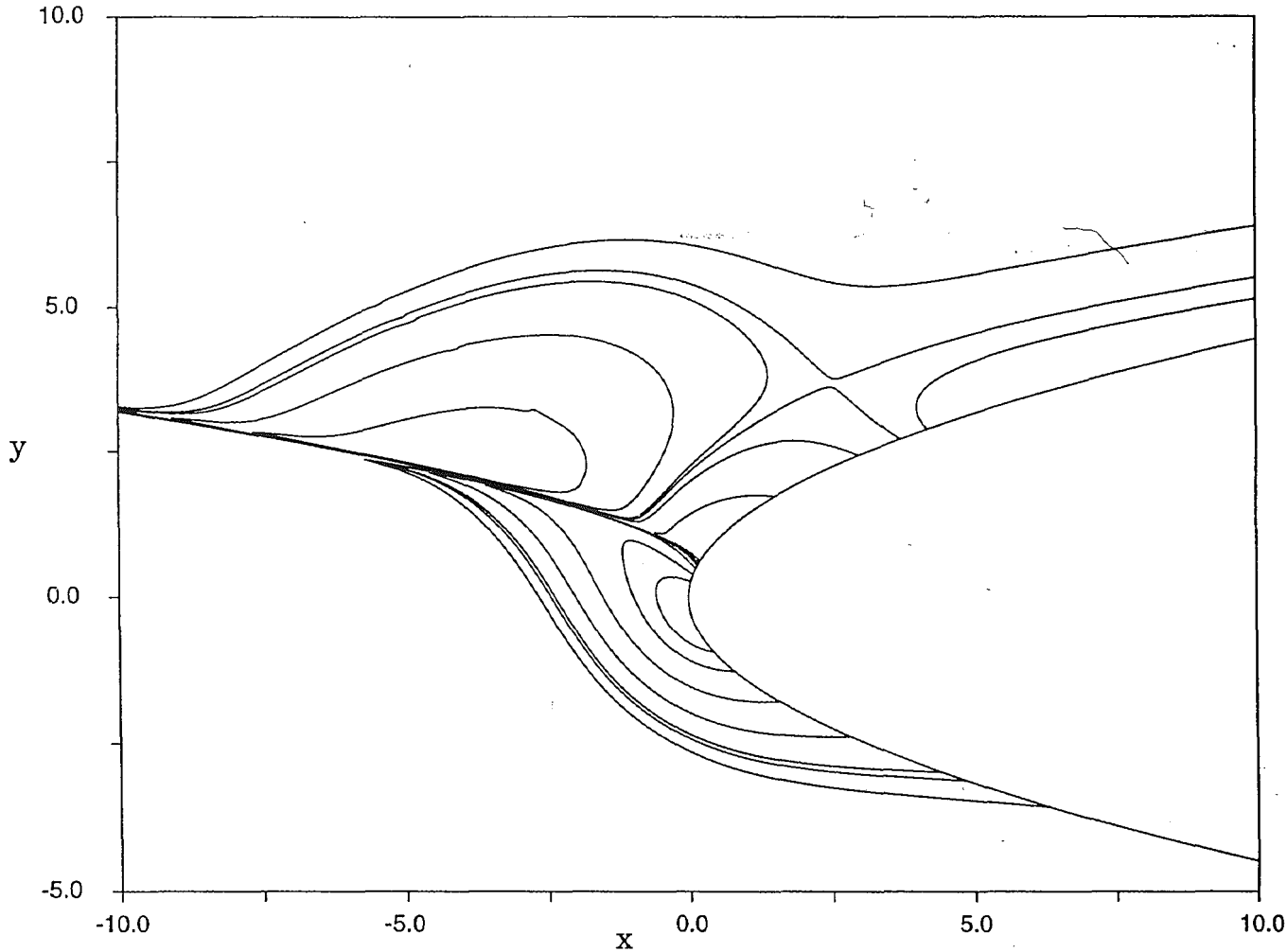

Figure 3.9 - Constant vorticity contours in cartesian coordinates at $t = t_s = 4.752$

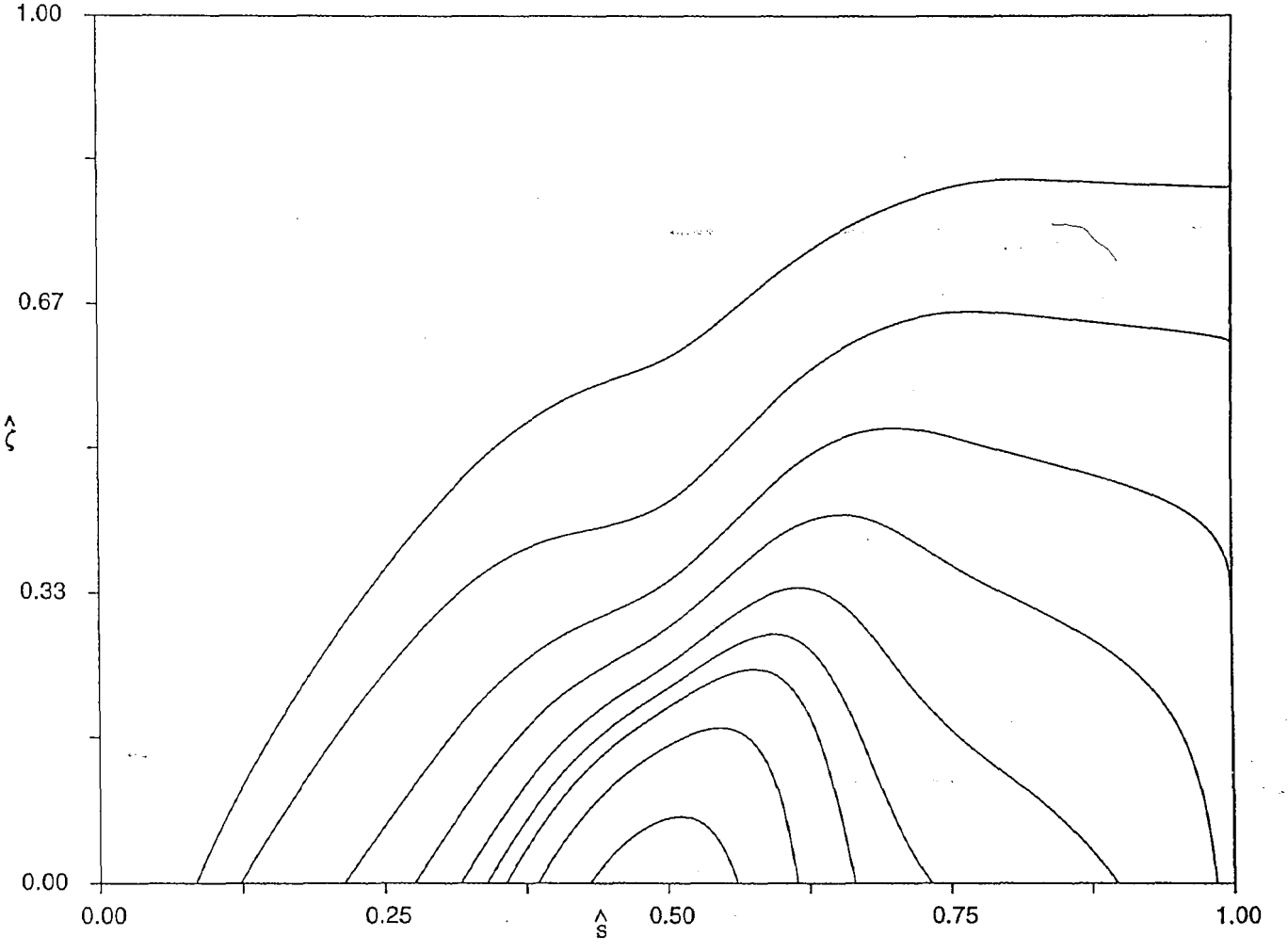

Figure 3.10 - Evolution of the constant vorticity contours in computational coordinates

3.10 (a) t = 2.0

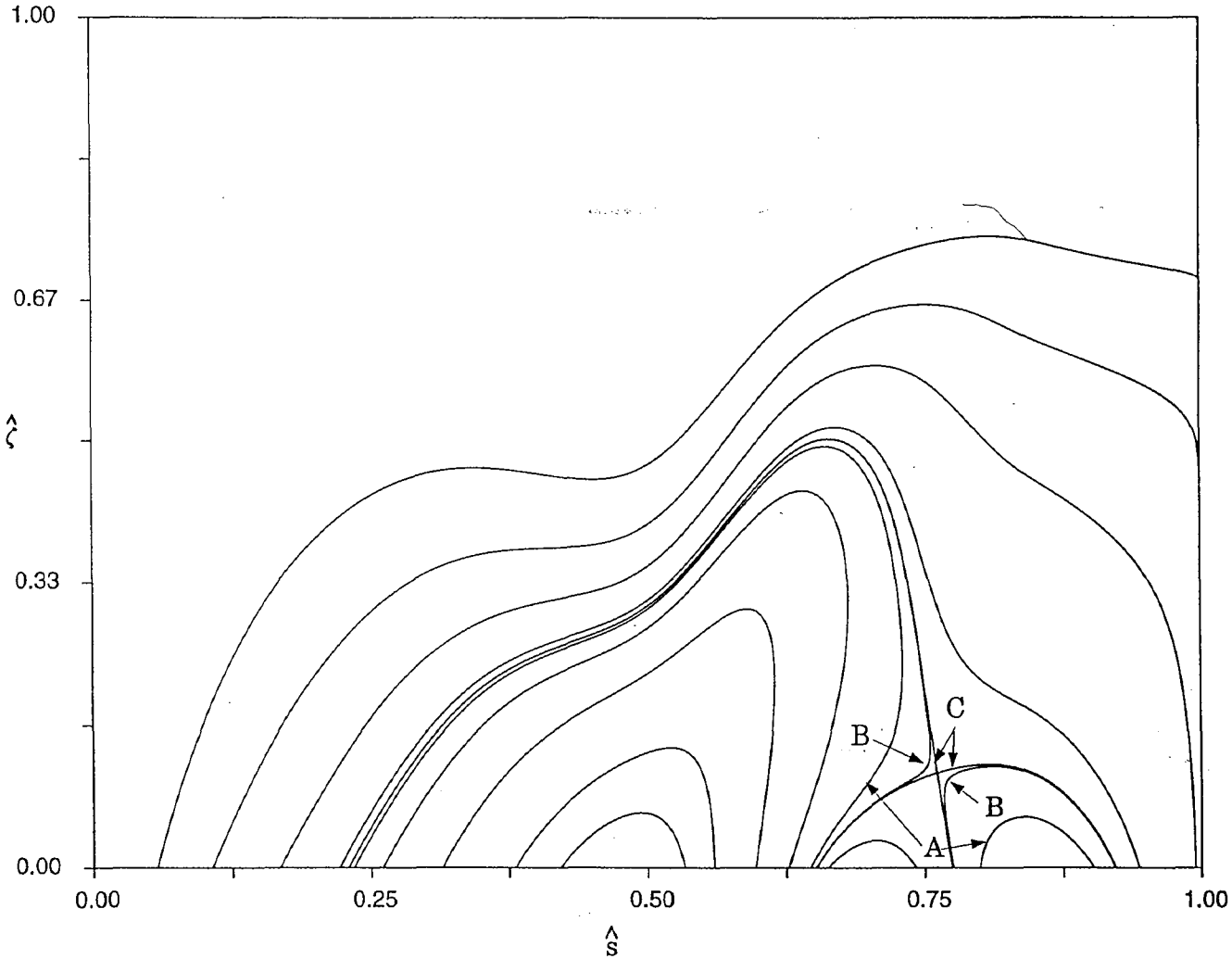

Figure 3.10 (b) t = 3.0

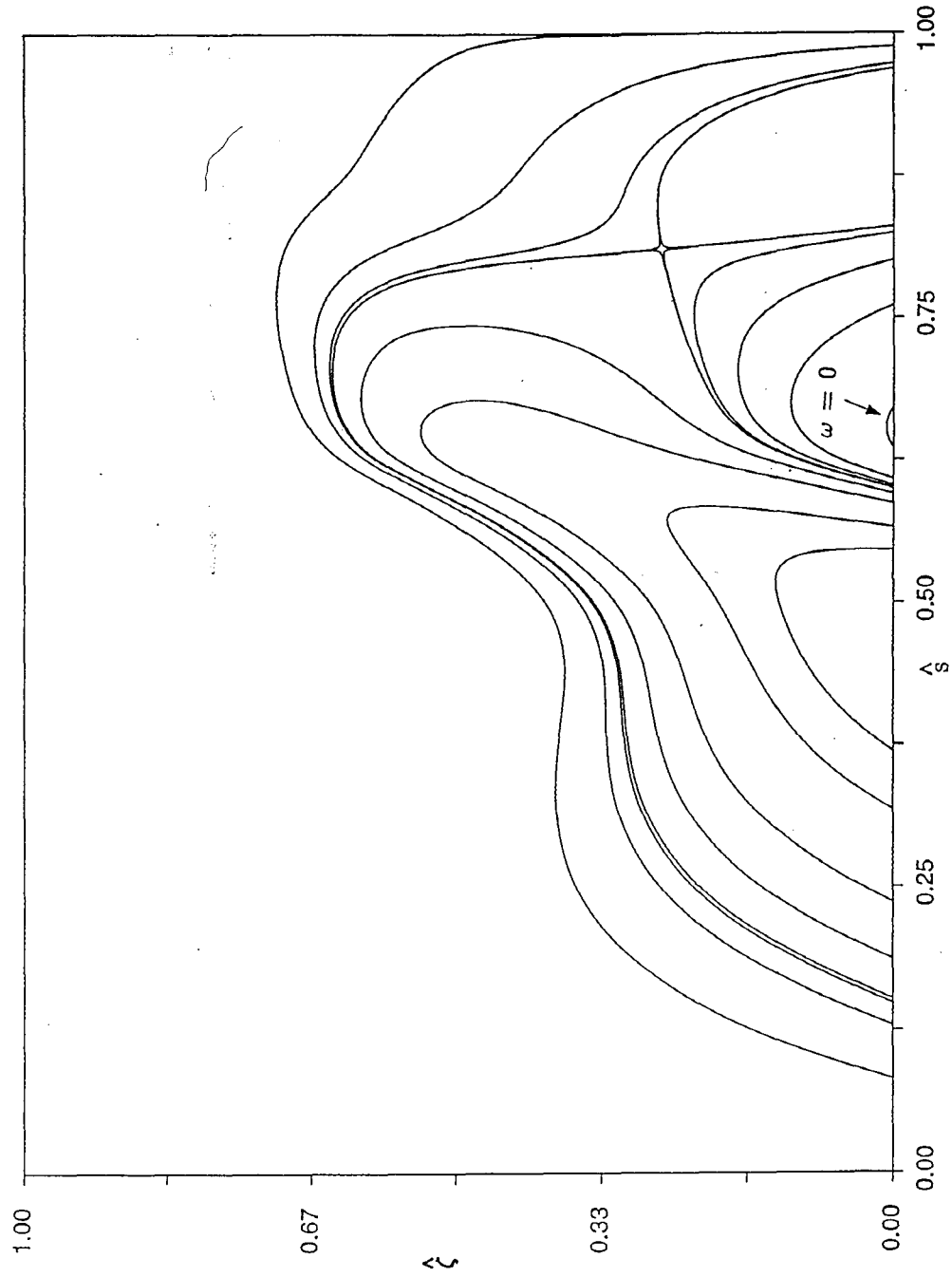

3.10 (c) $t = 4.0$

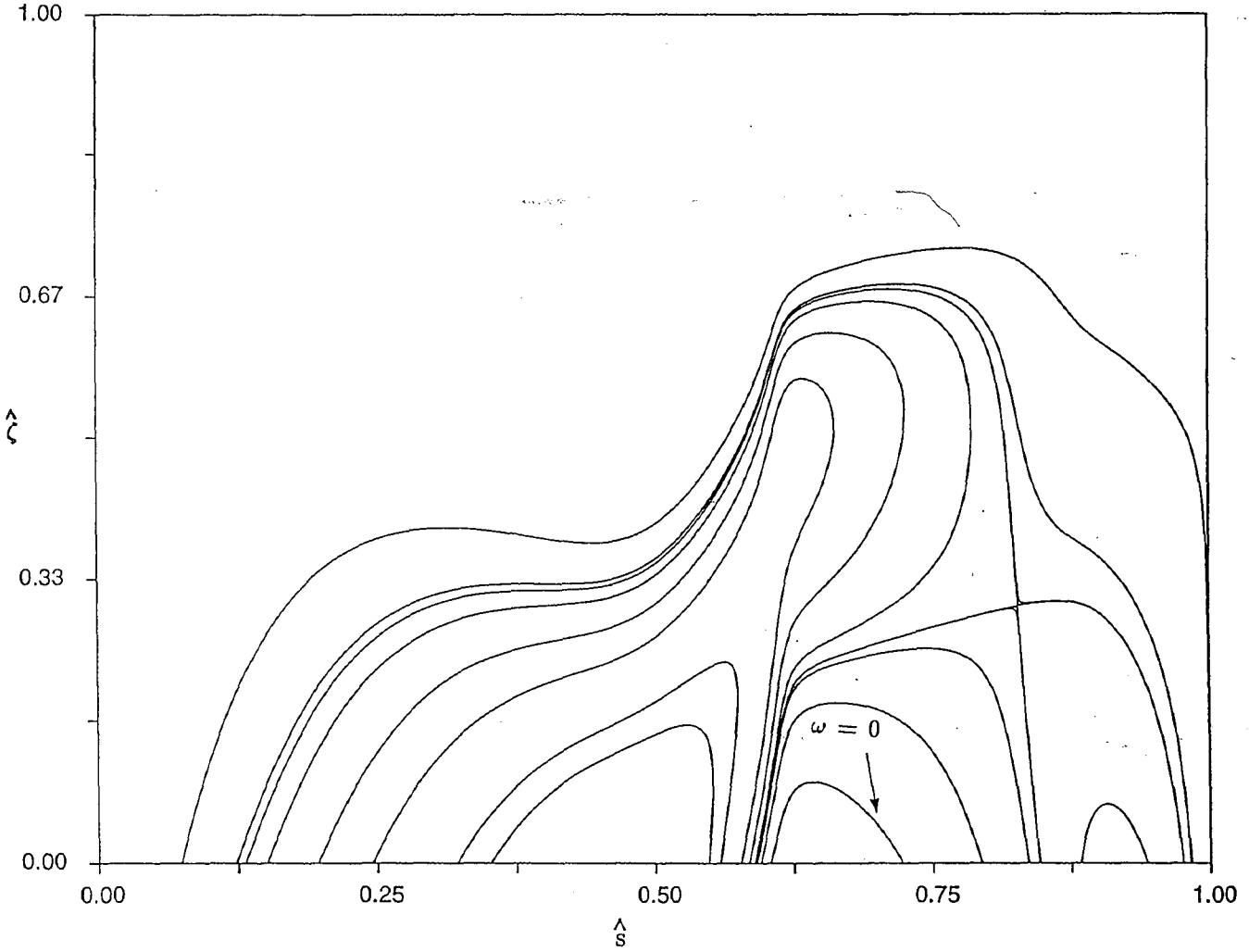

3.10 (d) t = 4.4

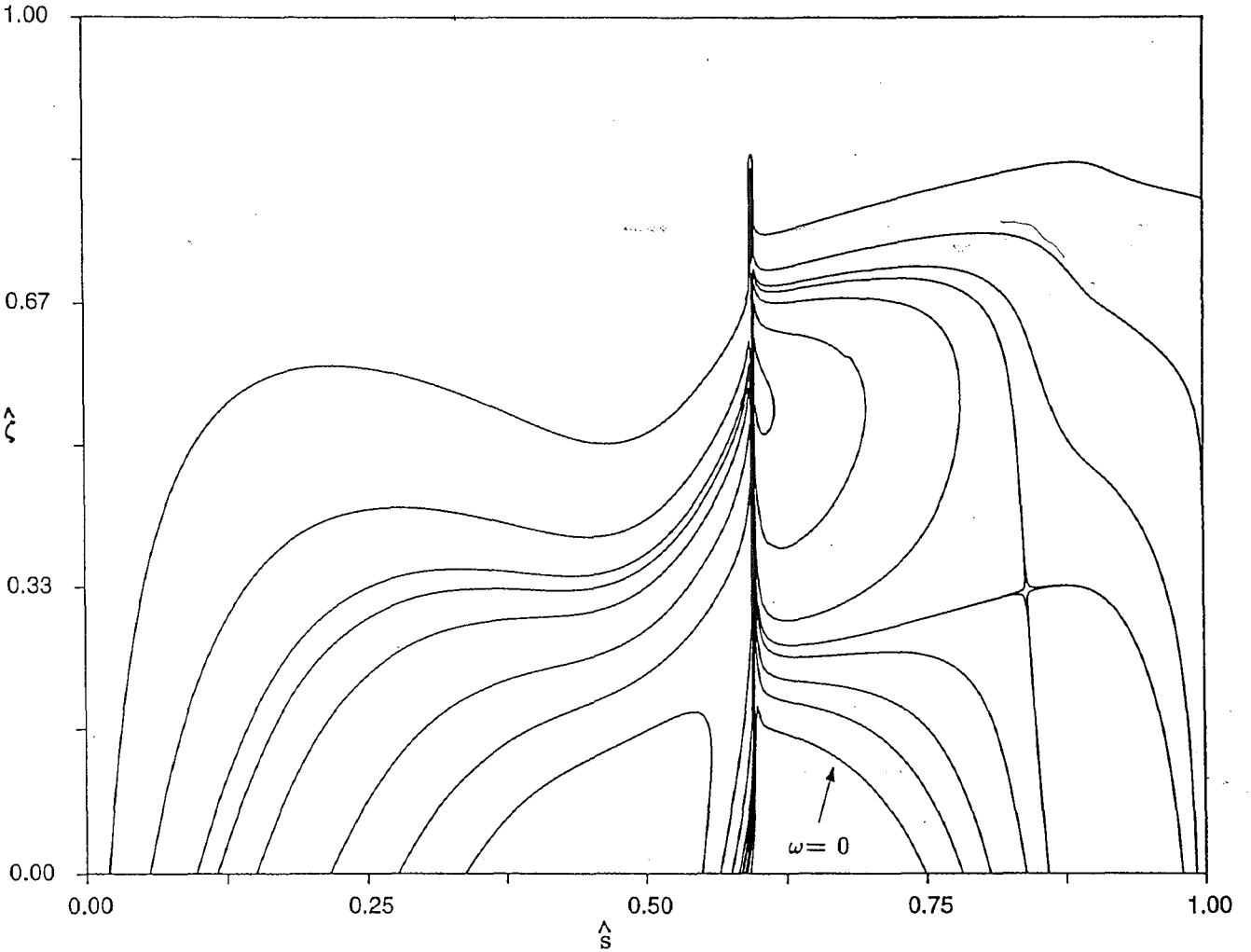

3.10 (e) $t = t_s = 4.752$

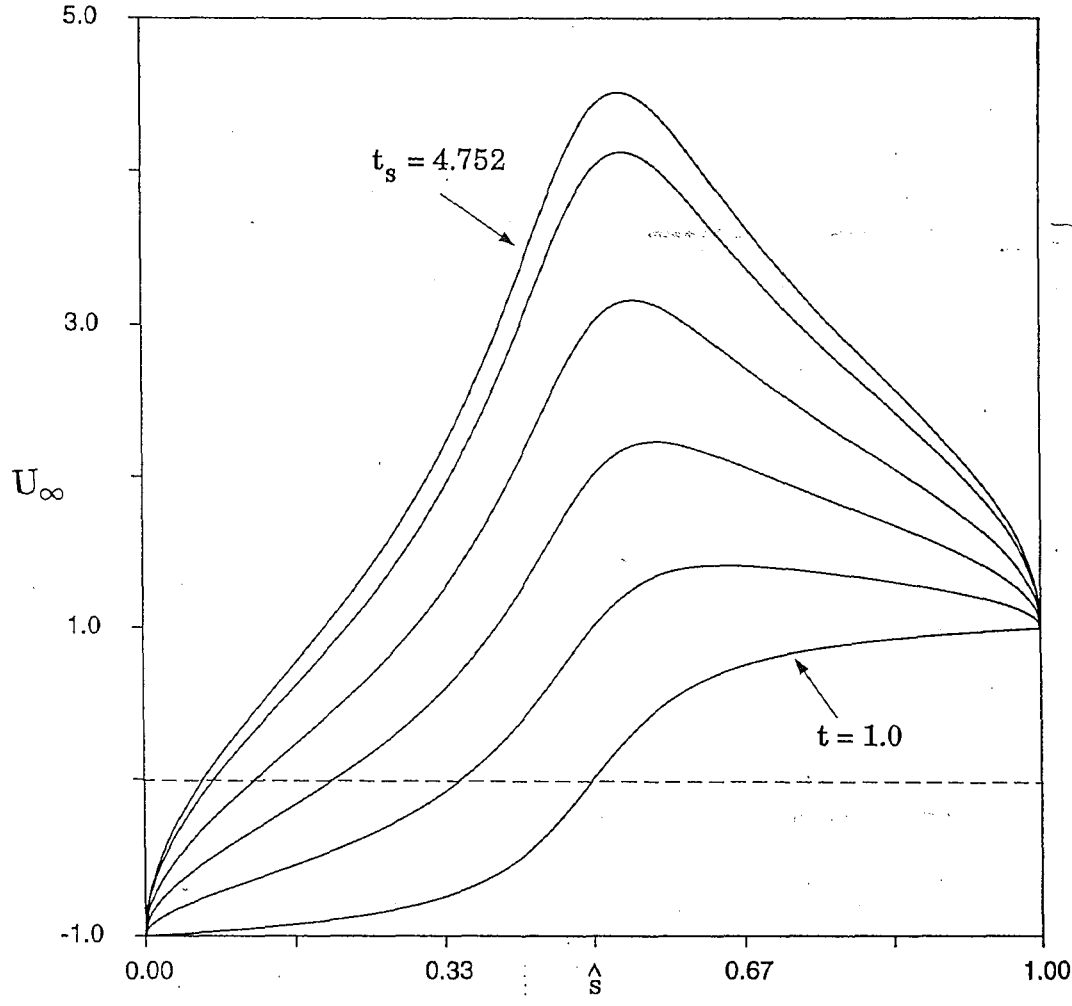

Figure 3.11 - Distribution of external velocity U_∞ at selected times: t = 1.0, 2.0, 3.0, 4.0, 4.4, 4.752

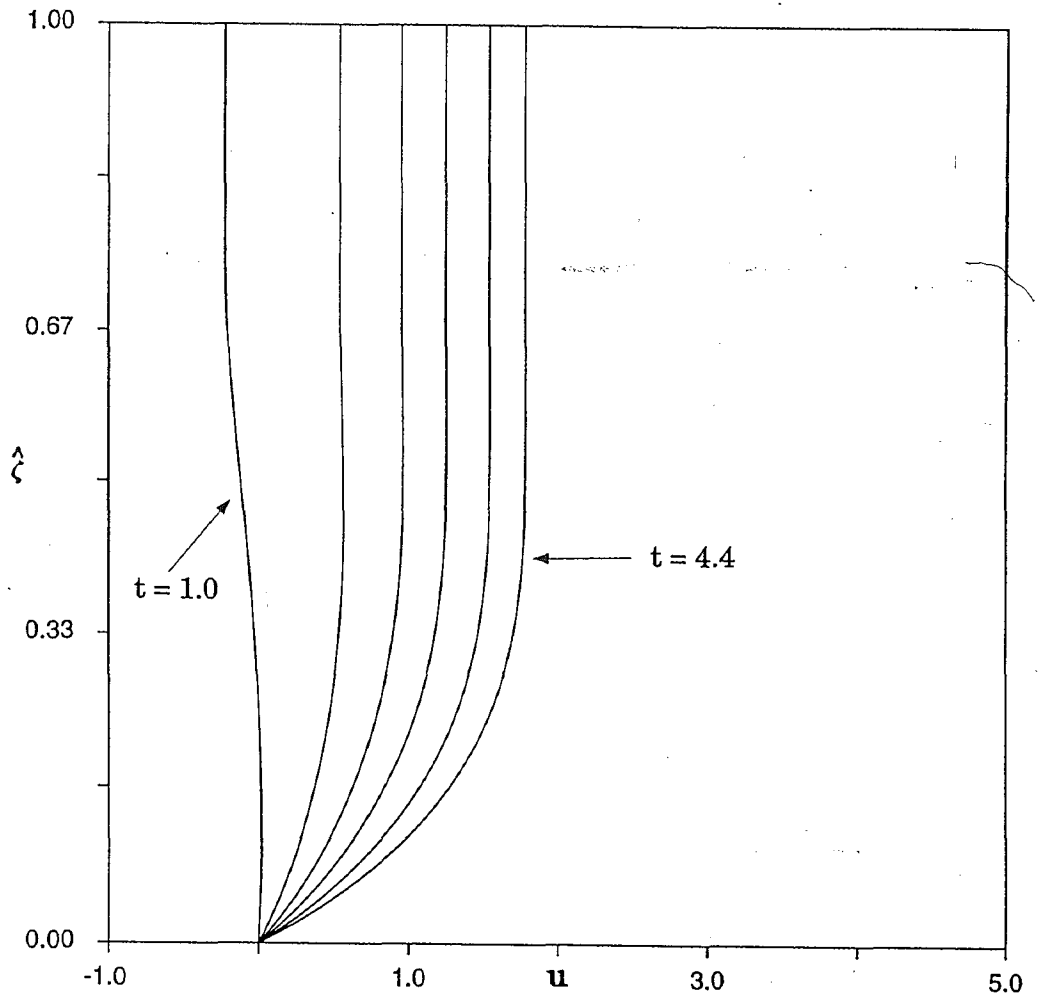

Figure 3.12 - Profiles of velocity **u** at selected $\hat{s}$ locations in the boundary layer at times t = 1.0, 2.3, 3.0, 3.5, 4.0, 4.4

3.12 (a) $\hat{s} = 0.3$

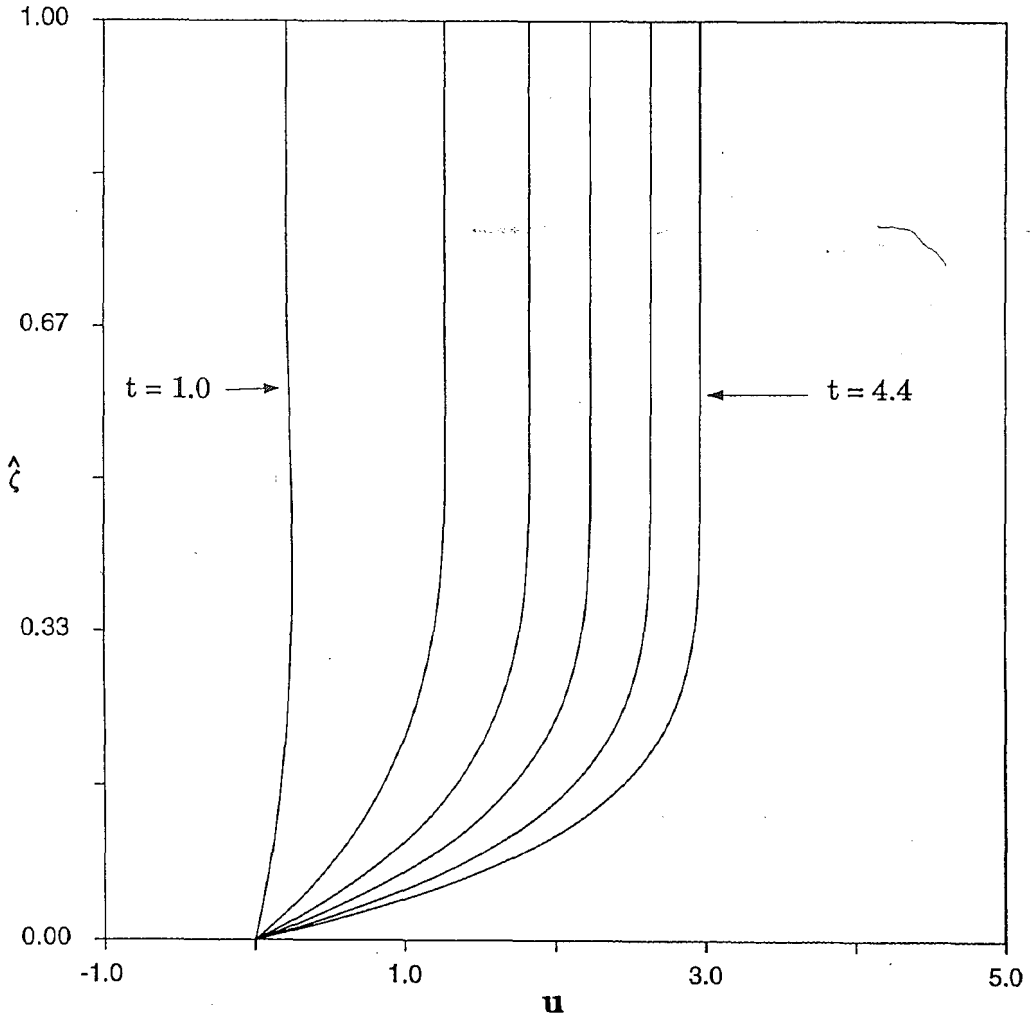

3.12 (b) $\hat{s} = 0.4$

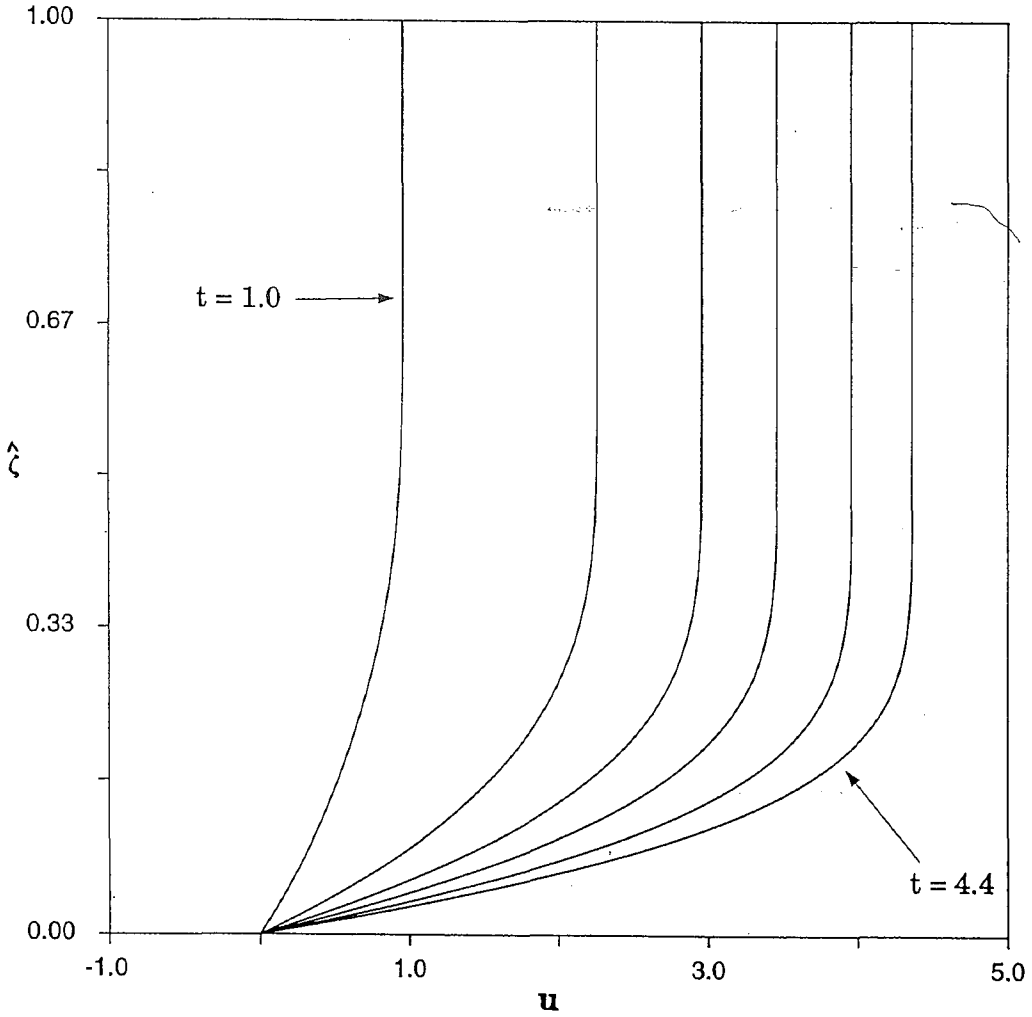

3.12 (c) $\hat{s} = 0.5$

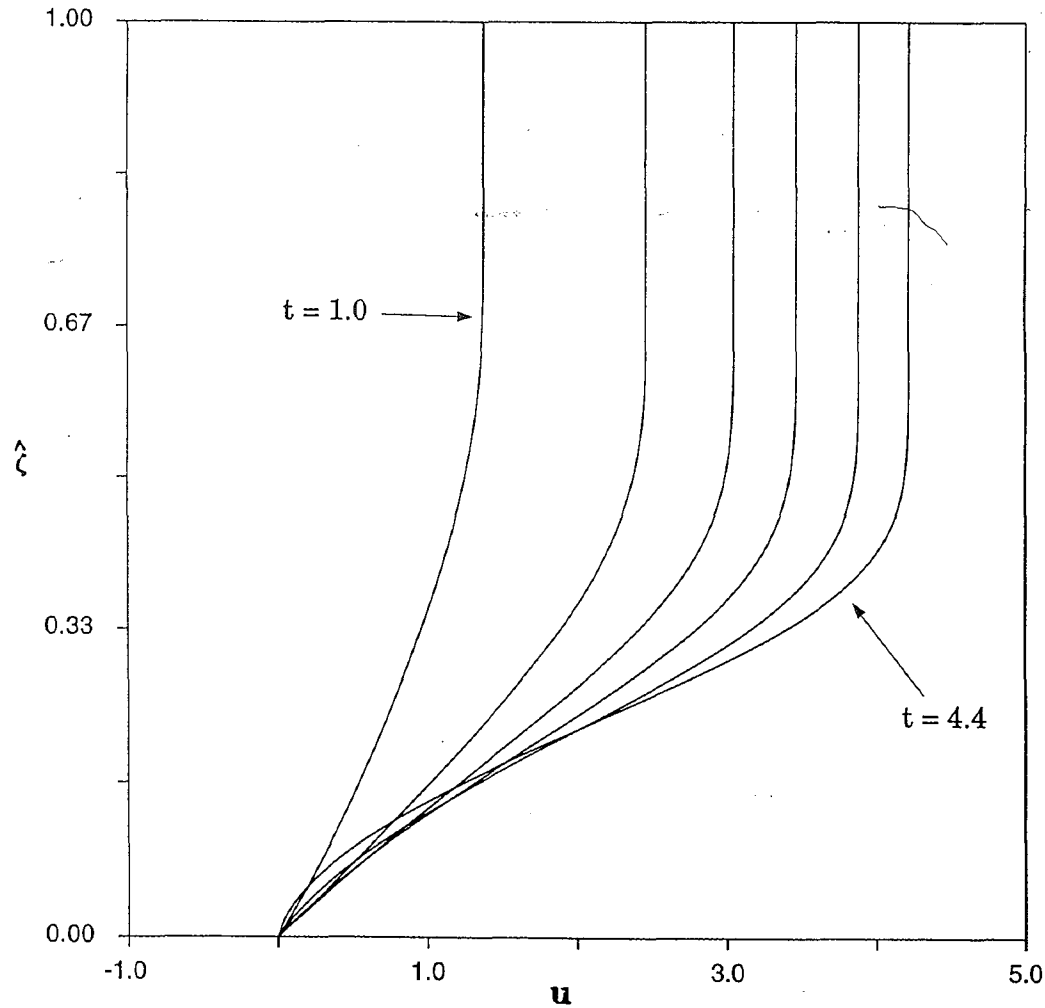

3.12 (d) $\hat{s} = 0.6$

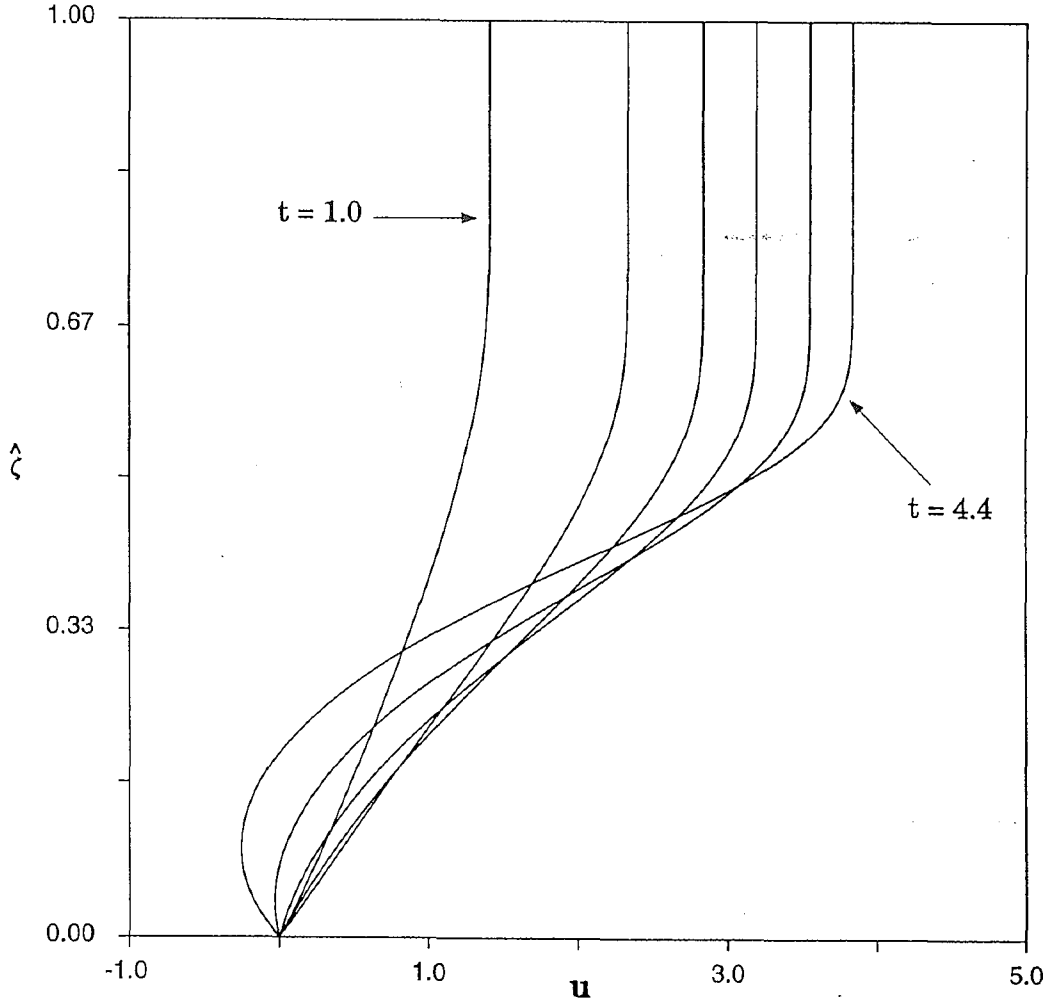

3.12 (e) $\hat{s} = 0.65$

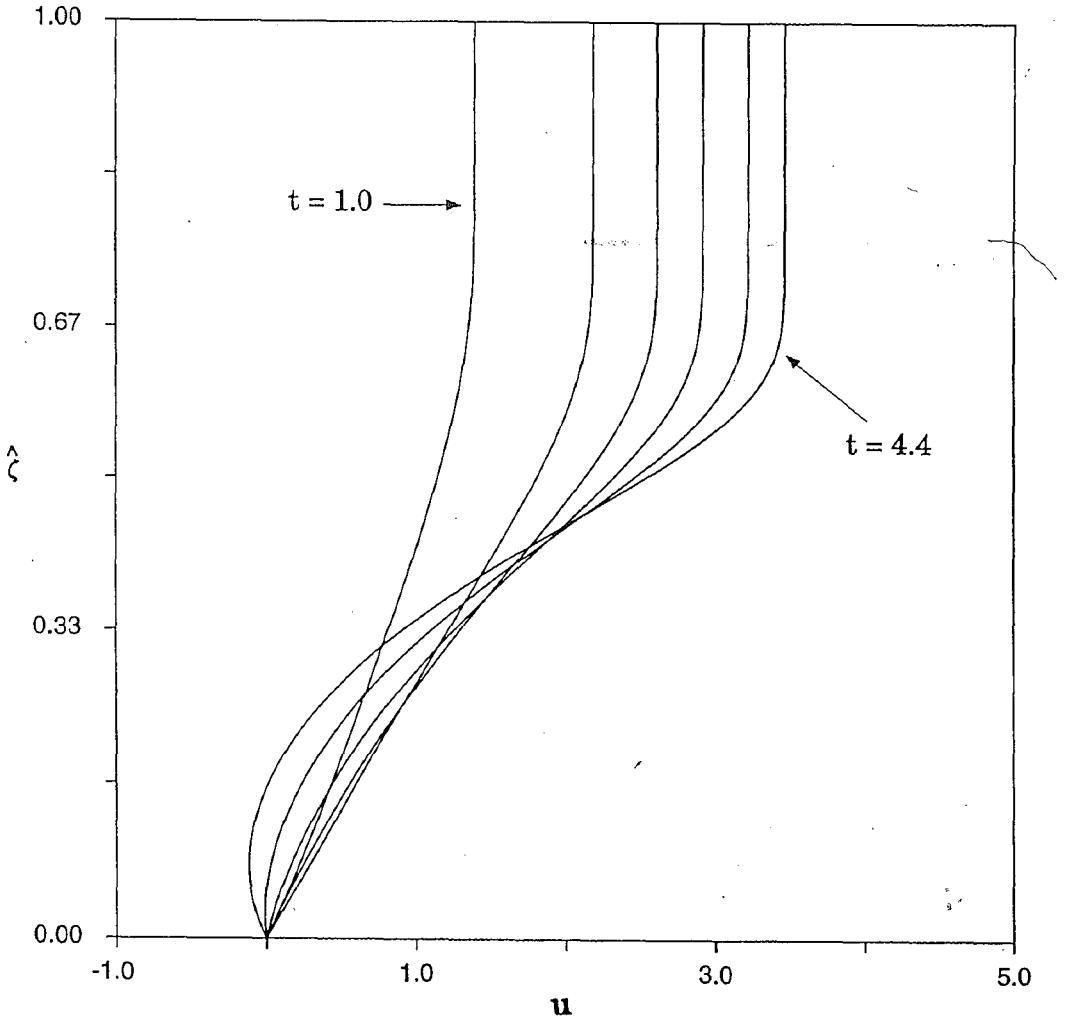

3.12 (f) $\hat{s} = 0.7$

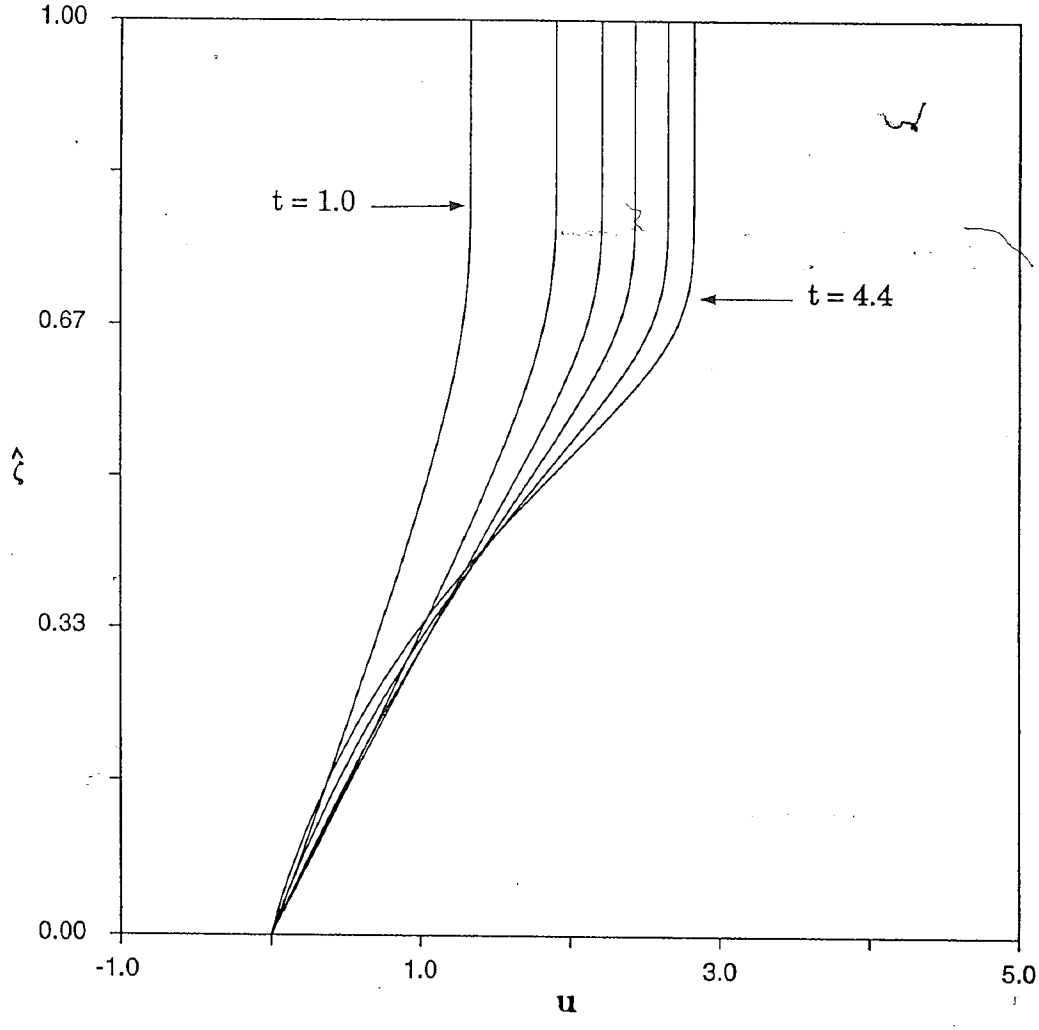

3.12 (g) $\hat{s} = 0.8$

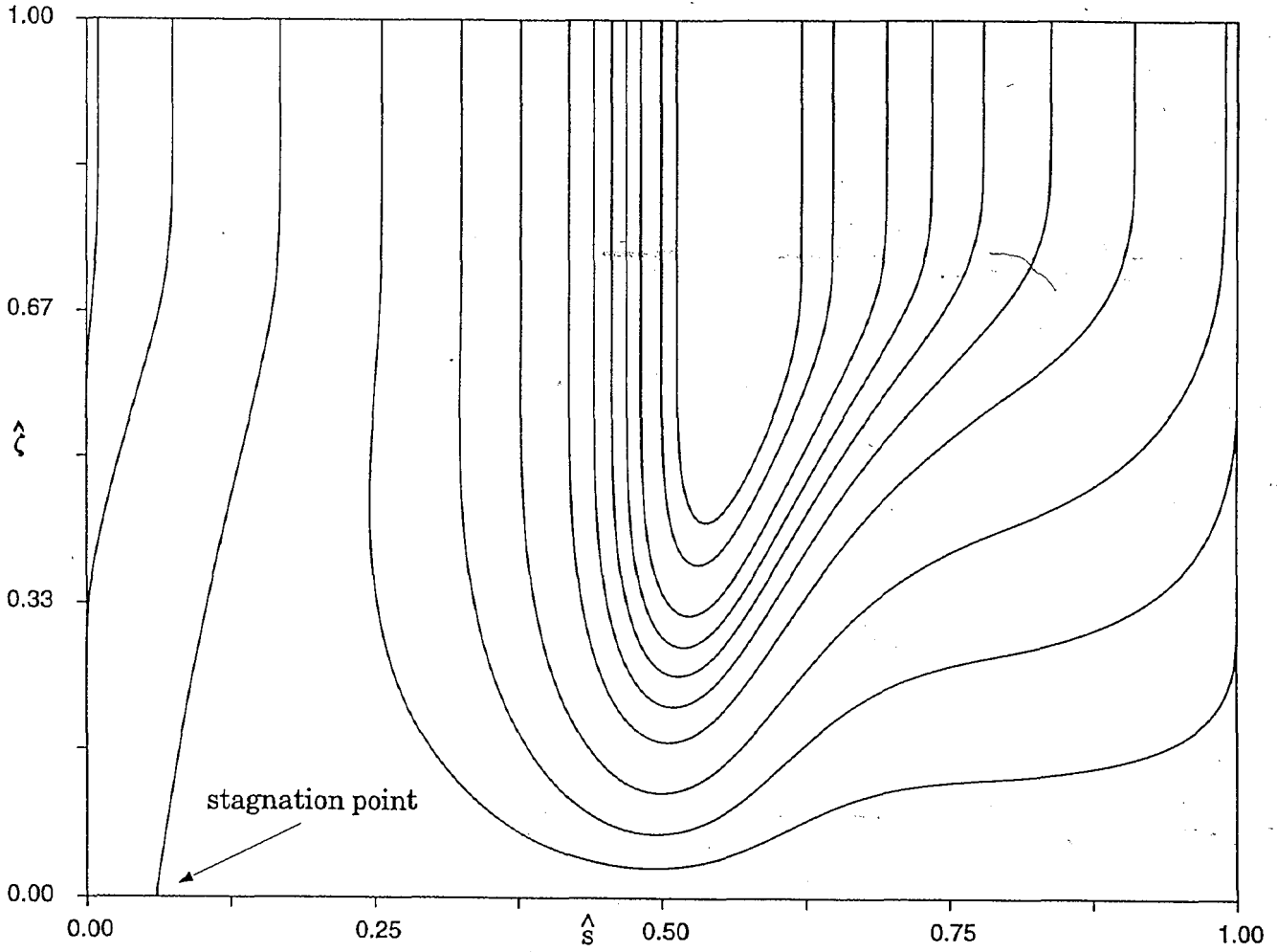

Figure 3.13 - Evolution of the constant line contours of velocity U in Lagrangian calculation

3.13 (a) t = 2.4

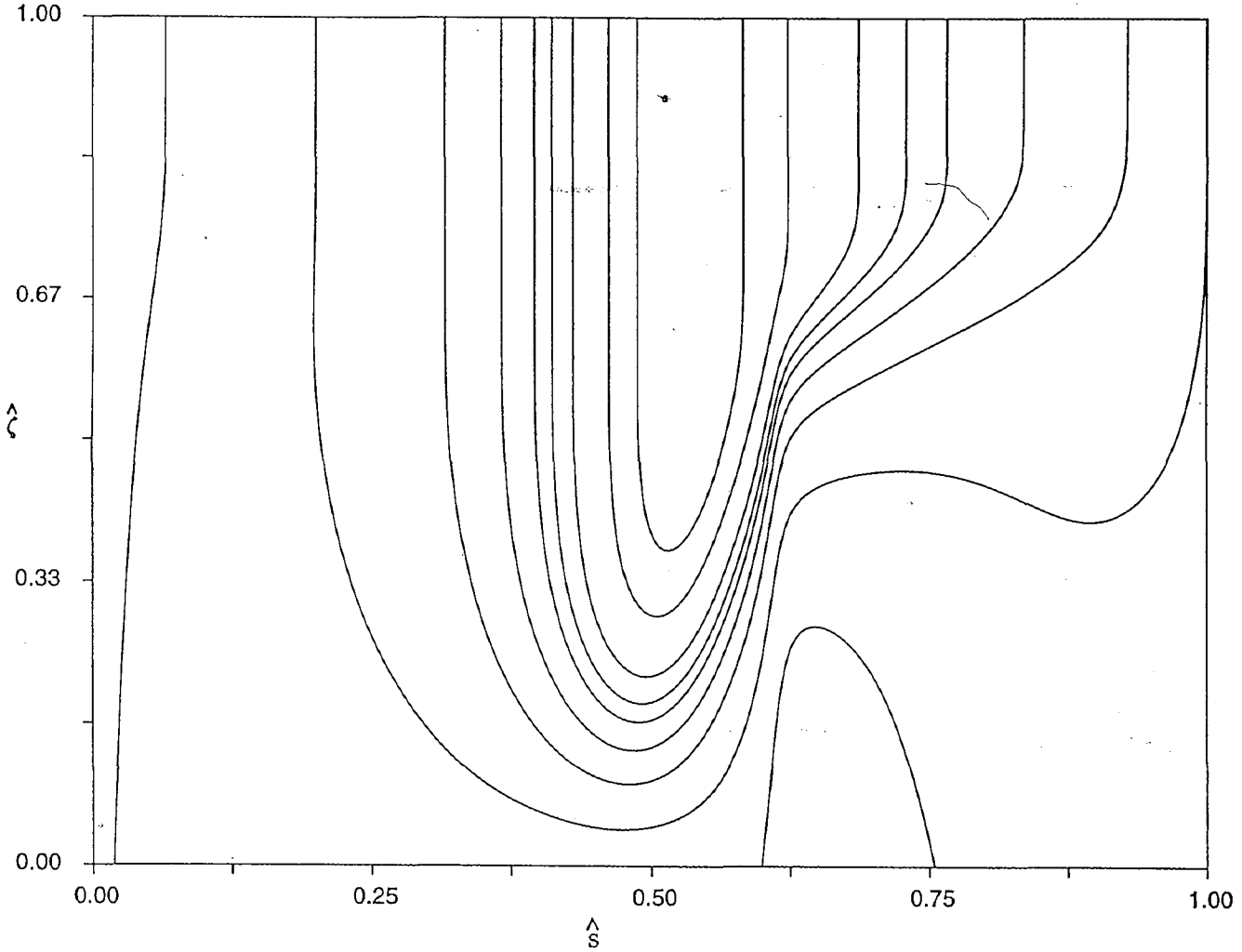

3.13 (b) t = 4.4

3.3 REVERSAL OF THE PITCHING RATE

In some situations, it is desirable to avoid the evolution of the primary stall vortex, and it is evident from the results of the preceding section that the principal control action would have to occur in the leading nose region where the phenomenon originates. Here, one possible control measure for suppressing or delaying boundary-layer separation is the reversal of the pitching rate at some time t_{rev} which is less than the singularity time t_s. Werle and Davis (1972) indicated that a steady boundary-layer solution is not possible for $A > 1.158$, and Ruban (1981) has refined the estimate to $A(t) > 1.1556$. Recently, Degani et al (1994) have shown that unsteady separation occurs for values of A greater than this critical value when the angle of attack is changed abruptly from zero to a constant positive value. As described in the previous section, similar results pertain when the angle of attack A(t) is increased smoothly. In this section, the question of what happens when the pitching rate is suddenly reversed is addressed.

First, the problem for continuously increasing the angle of attack was solved for several different linear pitching rates with $A(t) = bt$, and b lying in the range of $0.5 \leq b \leq 50$. Figure 3.14 shows the curve produced by plotting the parameter A(t) at $t = t_s$ for the different angles of attack. This asymptotic curve represents the limiting angle to which an airfoil can be pitched up to before a separation singularity (and the onset of the primary stall) develops. Figure 3.15 provides a few examples of A(t) as time t increases. The straight

lines indicate the instantaneous angle of attack as the airfoil pitches up linearly from zero angle of attack and show the maximum angle reached at separation. The dashed line is the critical angle of $A = 1.16$ as obtained by Werle and Davis (1972). A steady boundary-layer solution is not possible while an angle of attack is located in the region between $A = 1.16$ and the curve of $A(t_s)$, and separation will occur when the airfoil configuration is within this zone for a sufficient period of time.

To consider the influence of reversing the pitching rate to remove the airfoil from the separation zone, the parabola was pitched up linearly at a rate of $A(t) = t$ until a time $t = t_{rev} < t_s$. Then the influence of decreasing the angle of attack linearly at different rates was investigated. Two cases were considered where: (1) the pitching rate was reversed at $t_{rev} = 4.6$, a time well after the recirculation bubble had formed and shortly before boundary-layer separation, and (2) at $t_{rev} = 4.0$, a time immediately after the recirculation zone first appeared. Table 3.1 shows the results of several different computer runs where that angle of attack was reversed at $t_{rev} = 4.6$ according to the linear rate

$$A(t) = 4.6 - C \times (t - 4.6). \tag{3.23}$$

Here, the constant C was used to vary the decreasing pitching rate, and a value of $C = 1$ corresponds to decreasing the angle of attack at the same rate as increasing the angle with $A(t) = t$. The values in table 3.1 were obtained using the coarse 201 by 101 computational mesh since previous computational experiments established that this mesh yields good accuracy. The table

illustrates that separation may be delayed somewhat by choosing the constant in the range $0 < C \leq 7$, but the delay is very small and virtually insignificant. There is a value of the constant in the range $0 \leq C \leq 1$ where the maximum delay is possible. For $C > 7$, the pitching rate decreases at such a fast rate that the time to separation is actually decreased instead of delayed. The values of $A(t_s)$ for all the cases shown in table 3.1 are still greater than the critical value $A = 1.16$, and sufficient time has not elapsed for the angle to drop below the critical angle and separation occurs. It is evident, therefore, that it is not possible to have a major influence on inhibiting separation when the pitching rate is reversed too close to the time when separation would occur without reversing the pitching rate.

C	t_s	$A(t_s)$
−1.0	4.770	4.77
0.5	4.781	4.51
1.0	4.780	4.42
4.0	4.777	3.89
7.0	4.771	3.40
10.0	4.765	2.95
20.0	4.755	1.51

Table 3.1 - Pitching rate $A(t) = t$ for a parabola is reversed at $t = 4.6$; the angle of attack decreases linearly according to $A(t) = 4.6 - C \times (t - 4.6)$, where C is a constant.

To understand the flow development, instantaneous streamline patterns for some of these cases are considered. Recall that the instantaneous streamlines at $t = 4.6$ are shown in figure 3.3(e) corresponding to the fluid motion at the beginning of reversal of the pitching rate. Figure 3.16 shows the instantaneous streamlines for $C = 0.5$ where it may be seen that the stagnation point now attaches to the lower surface of the parabola in a different manner, reflecting the reversal of the pitching rate. The streamline $\psi = 0$ bends near the surface and is now deflected towards the vertex of the parabola. As in the case of $A(t) = t$ studied in section 3.2, a spike develops on the upstream side of the recirculation zone. However, by comparing figures 3.16 and 3.3(f), the region of recirculating fluid is somewhat larger in both spatial dimensions and the separation point is closer to the vertex of the parabola in figure 3.16.

Figure 3.17 shows the instantaneous streamlines at $t = t_s = 4.777$ for $C = 4$. The point of attachment for the zero streamline has moved closer to the vertex than in the previous case (note the angle of attack $A = 3.89$ at $t_s = 4.777$ is somewhat smaller). In addition, the recirculation zone has expanded and the point of re-attachment for the zero streamline defining the recirculation zone has moved significantly downstream on the upper surface of the parabola.

Figure 3.18 illustrates the instantaneous streamlines at $t = t_s = 4.765$ for $C = 10$. The stagnation point is still located on the surface but now is almost at the vertex and very close to the zero streamline defining the edge of the eddy. The recirculation zone is larger than in the previous cases and actually stretches along the upper surface before the zero streamline attaches to the

parabola relatively far downstream. This phenomenon appears to produce an elongated pocket of recirculating fluid.

The results just described suggest that it is not possible to inhibit separation when reversal of the pitching rate is started too late and near the time the boundary layer would separate if the angle of attack were continually increased. Consequently, the influence of initiating reversal of the pitching rate at an earlier stage at $t_{rev} = 4.0$ is now considered. Table 3.2 shows the results of reversing the angle of attack at $t_{rev} = 4.0$. The value of the decreasing rate is controlled by the constant B in

$$A(t) = 4.0 - B \times (t - 4.0). \tag{3.24}$$

Recall from section 3.2 that the recirculation bubble first appears at a time in the range $3.6 < t < 3.8$ and, therefore, $t = 4.0$ is at a time just after the eddy has formed. The results in table 3.2 demonstrate that separation is not delayed, but now occurs earlier; note again, however, that the decrease in t_s is not very large.

B	ts	$A(t_s)$
−1	4.770	4.77
0.05	4.726	3.96
0.1	4.724	3.93
0.25	4.719	3.82
0.5	4.710	3.65
1.0	4.690	3.31
5.0	4.558	1.06

Table 3.2 - Pitching rate $A(t) = t$ for a parabola is reversed at $t = 4.0$; the angle of attack decreases linearly according to $A(t) = 4.0 - B \times (t - 4.0)$, where B is a constant.

Figures 3.19(a) through 3.19(c) show the instantaneous streamlines for $B = 1$, corresponding to a decreasing rate equal to the original rate of increase of A(t). Figure 3.19(a) illustrates the streamlines at time $t = 4.1$ where $A = 3.9$. The zero streamline attaches to the lower surface in a direction toward the vertex and the recirculation bubble has grown a significant amount after only $\Delta t = 0.1$. In fact, comparing to figure 3.3(d), it may be seen that the bubble is now thicker in the streamwise direction than the bubble at $t = 4.4$ for $A(t) = t$. Figure 3.19(b) shows the streamlines at $t = 4.5$ where the

instantaneous angle of attack is $A = 3.5$. The bubble is now even larger and the shape is distorted. Figure 3.19(c) shows the spike that has subsequently developed at $t = t_s = 4.69$ $(A = 3.31)$. The recirculation bubble is much larger in both the streamwise and normal directions than the bubble in figure 3.3(f). In summary, there are two important conclusions from comparing the results for continuous upward pitching $A(t) = t$ with those obtained by reversing the pitching rate at $t_{rev} = 4.0$ according to $A(t) = 4.0 - (t - 4.0)$: (1) boundary-layer separation occurs sooner for the latter case even though the angle of attack decreases for $t > t_{rev}$; and (2) the zone of recirculating fluid is larger in both dimensions for the latter case.

Figures 3.20(a) and 3.20(b) show the instantaneous streamlines for a case $B = 5$ where the reversed pitching rate is significantly increased. In figure 3.20(a), it is seen that the stagnation point is almost at the vertex and almost intersects the recirculation zone at $t = 4.5$, where $A = 1.5$. The bubble is stretched out in a similar manner as seen in figure 3.18. Figure 3.20(b) shows that the stagnation point is no longer attached to the surface of the parabola at $t_s = 4.588$. The bubble is stretched out even more and connects to the upper surface of the parabola at a point far downstream. Although not visible in figure 3.20(b), there is a saddle point aloft above the wall near the vertex. The exact location and limiting streamline is difficult to plot in the physical plane but are easily shown in the computational plane as in figure 3.20(c). The streamlines do not appear as smooth near the wall because the majority of points were used to resolve the "spike." Note that the parameter $A = 1.06$ is less than the critical value of $A = 1.16$ (Werle and Davis, 1972), but that a

singularity still develops because of the prior presence of a recirculation zone in the boundary layer.

Figures 3.21(a) through 3.21(d) illustrate the temporal development of the instantaneous streamline patterns for an even larger rate of decrease $B = 10$. At $t = 4.1$, $A = 3.0$ and the stagnation point has almost reached the vertex. Figure 3.21(b) shows that the zero streamline has again detached from the surface at $t = 4.3$ where $A = 1.0$; again a saddle point occurs in the streamlines near the vertex although this is not shown in figure 3.21(b). Figure 3.21(c) illustrates the streamlines when $A = 0.0$ at $t = 4.4$, for the airfoil has now returned to zero incidence. The zero streamline attaches to the parabola far downstream and the saddle point has moved farther from the wall. The limiting streamline through the saddle point bounds a zone of very weak recirculation. Figure 3.21(d) shows that a singularity does indeed develop at $t_S = 4.559$ where parameter $A = -1.59$; thus the airfoil is now at negative incidence. With the parabola pitched below zero incidence, the streamlines now appear to impinge the upper surface. However, the streamlines to the left of the vertex are focussed into a "spike." However, the spike does not attach to the surface and some fluid is capable of traveling through the region near the vertex and down along the lower surface of the parabola. The zero streamline $\psi = 0$ is deflected away from the upper surface and is not seen to attach on the scale of figure 3.21(d).

Figure 3.22 illustrates the normal perturbation $\widetilde{A}$ at selected times for $B = 10$ in equation (3.24). Note that the values in the vicinity of the vertex are somewhat larger than for those for the continuously pitched airfoil with

$A(t) = t$ shown in figure 3.8. Therefore, reversing the pitching rate causes the boundary layer to induce somewhat larger perturbation velocities in the outer flow near the vertex. Close examination of figures 3.21(d) and 3.22 suggests that the "spikey" response of the boundary layer is much weaker, however, than for that shown in figure 3.8, with the events that develop in figure 3.22 taking place over a narrower streamwise region.

Figures 3.23(a) through 3.23(b) show the evolution of the constant vorticity contours in computational coordinates for a reverse pitching rate $B = 10$. Figure 3.23(a) shows that there are two zero vorticity contours $\omega = 0$ which attach to the surface. The vorticity between the lines $\omega = 0$ and the surface is positive; everywhere else it is negative. The line $\omega = 0$ attached to the upper surface ($\hat{s} > 0.5$) corresponds to that associated with the recirculation zone on the upper surface. As shown in figure 3.23(b), by $t = 4.3$ there is now only one constant contour $\omega = 0$, and that it is located above the surface and only connects to the surface near downstream infinity; in the intervening period between 4.1 and 4.3, the two $\omega = 0$ lines have merged at the surface and then moved away from the wall. Again, all constant vorticity contours below this line are positive. Figure 3.23(c) indicates that the zero contour has moved further from the surface by $t = 4.4$ and now attaches to the surface closer to downstream infinity. Figure 3.23(d) then shows that a spike-like behavior develops on the zero vorticity line by $t = t_S = 4.559$. The zero contour is much further from the surface at this stage, and the focussed spike corresponds to the eruption developing in the streamlines shown in figure 3.21(d). Note, however, that this developing eruption is considerably weaker than those

observed on the upper surface when the pitching rate was always positive.

The next case considered corresponded to reversing the pitching rate at $t = 4.0$, decreasing the angle of attack by $A(t) = 4.0 - 10 \times (t - 4.0)$ to $A = 0$, and then holding the parabola fixed at zero incidence thereby not allowing the configuration to move to negative incidence. Figure 3.24(a) shows the instantaneous streamlines at $t = 4.5$ where $A = 0.0$. The recirculation zone is stretched far upstream and the zero streamline is deflected along the upper surface in a similar fashion to figure 3.21(c). Figure 3.24(b) shows that the streamlines are focussed together along the bottom of the recirculation zone at $t = t_s = 4.556$ and again a singularity develops. The flow in the recirculation region is driven by the streamlines coming in from upstream (which are sharply bent back) and by streamlines going around the right part of the recirculation zone and under it before being bent back to follow the lower surface of the parabola. Also, the zero streamline attaches to the parabola at a stagnation point far downstream on the upper surface. There is a saddle point of stagnation which is not shown in figure 3.24(b) because it proved difficult to draw this limiting streamline in the physical coordinates. The pattern is more easily drawn in computational coordinates, and figure 3.25 illustrates the flow topology in computational coordinates at $t = t_s = 4.556$. A saddle point exists on the left side of the recirculation region.

The last situation studied here corresponds to reversing the pitching rate at $t = 3.5$, which for $A(t) = t$ is a time just before the formation of the recirculating eddy. Figure 3.26 shows the streamlines for reversed pitching rate of $B = 1$ with $A(t) = 3.5 - (t - 3.5)$ at $t = t_s = 4.657$ where $A = 2.34$. A

recirculation bubble does form during the reversal of the pitching and again a separation singularity occurs. If the reversed pitching rate is increased to $B = 10$, again a separation singularity occurs as shown in figure 3.27. Here, the instantaneous streamlines are shown at $t = t_s = 4.616$ for a case where $A(t) = 3.5 - 10(t - 3.5)$ when $t < 3.85$ and and for which incidence was maintained at $A(t) = 0.0$ for $t \geq 3.85$. The angle of attack is zero at $t = t_s$ and the zero streamline $\psi = 0$ attaches to the upper surface of the parabola this time near the vertex. The spike again is relatively weak but is now located somewhat to the left of the vertex.

Figures 3.28 shows the temporal development of the instantaneous streamline patterns when the reversed pitching rate is increased to $B = 35$ with $A(t) = 3.5 - 35(t - 3.5)$ when $t < 3.6$ and $A(t) = 0.0$ for $t \geq 3.6$. The reversal rate is much faster than all of the previous cases studied. Figure 3.28(a) illustrates the streamlines at $t = 3.51$ where $A = 3.15$. A recirculation bubble is present after only $\Delta t = 0.01$. Figure 3.28(b) shows the streamlines at $t = 3.6$ where parameter A has just reached $A = 0.0$. The recirculation region is now located just off of the upper surface near the vertex, and the zero streamline is deflected around this region and over the top surface. Figure 3.28(c) illustrates that the recirculation zone has shrunk and $\psi = 0$ now attaches to the upper surface at $t = 4.0$. By the time $t = 4.5$, the recirculation region has decreased in size and the stagnation point has moved closer to the vertex as seen in figure 3.28(d). Figure 3.28(e) shows that the recirculation region has decreased and attached itself to the upper surface as a bubble at $t = 5.0$. The zero streamline has its stagnation point at the vertex. Figure 3.28(f)

illustrates that the recirculation bubble of fluid has disappeared altogether by $t = 5.8$. The zero streamline is straight and connects to the parabola at the vertex as it would if the flow were impulsively started with A being held constant at $A = 0.0$. As time increases, the flow over the top surface will approach the steady state were the flow topology is identical over the top and bottom surfaces and it will remain in that form as long as angle of attack remains at $A = 0.0$.

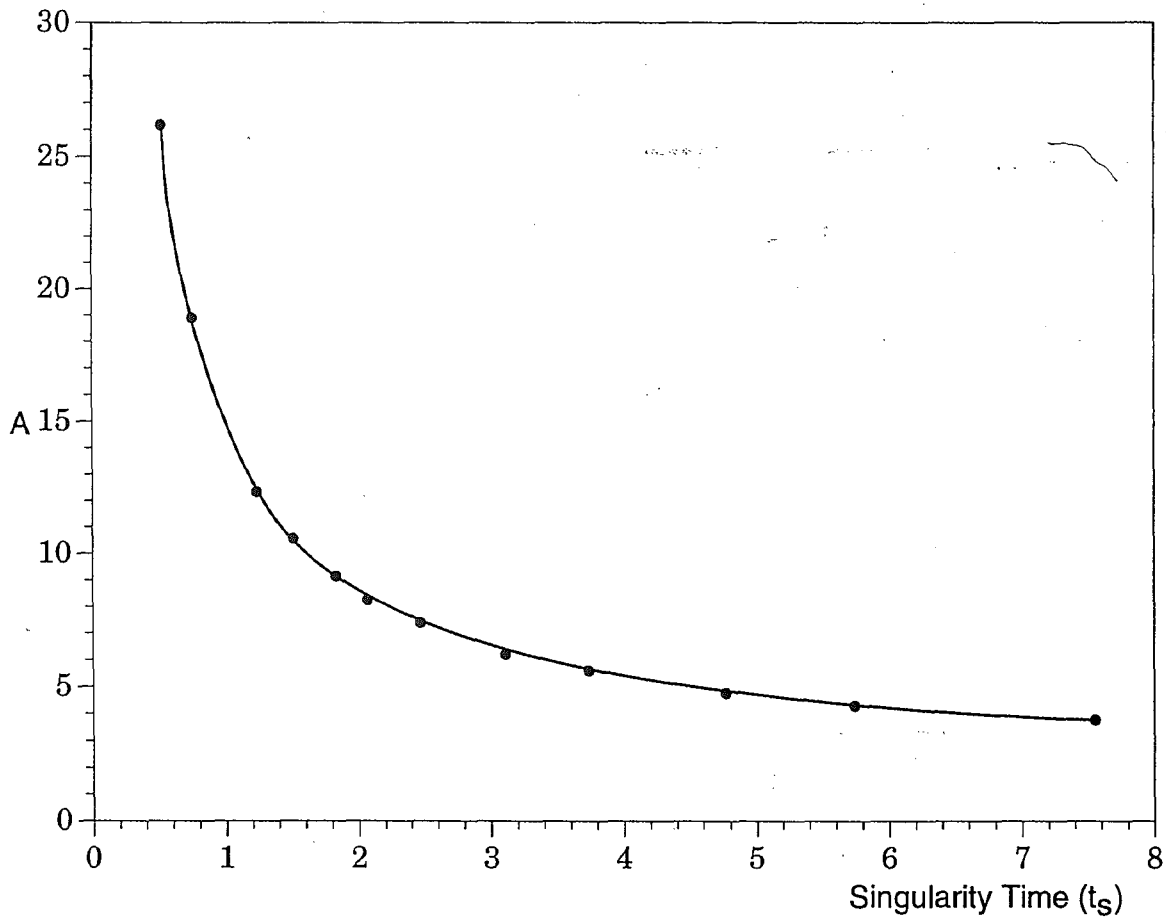

Figure 3.14 - Parameter A at the singularity time t_S for different angles of attack

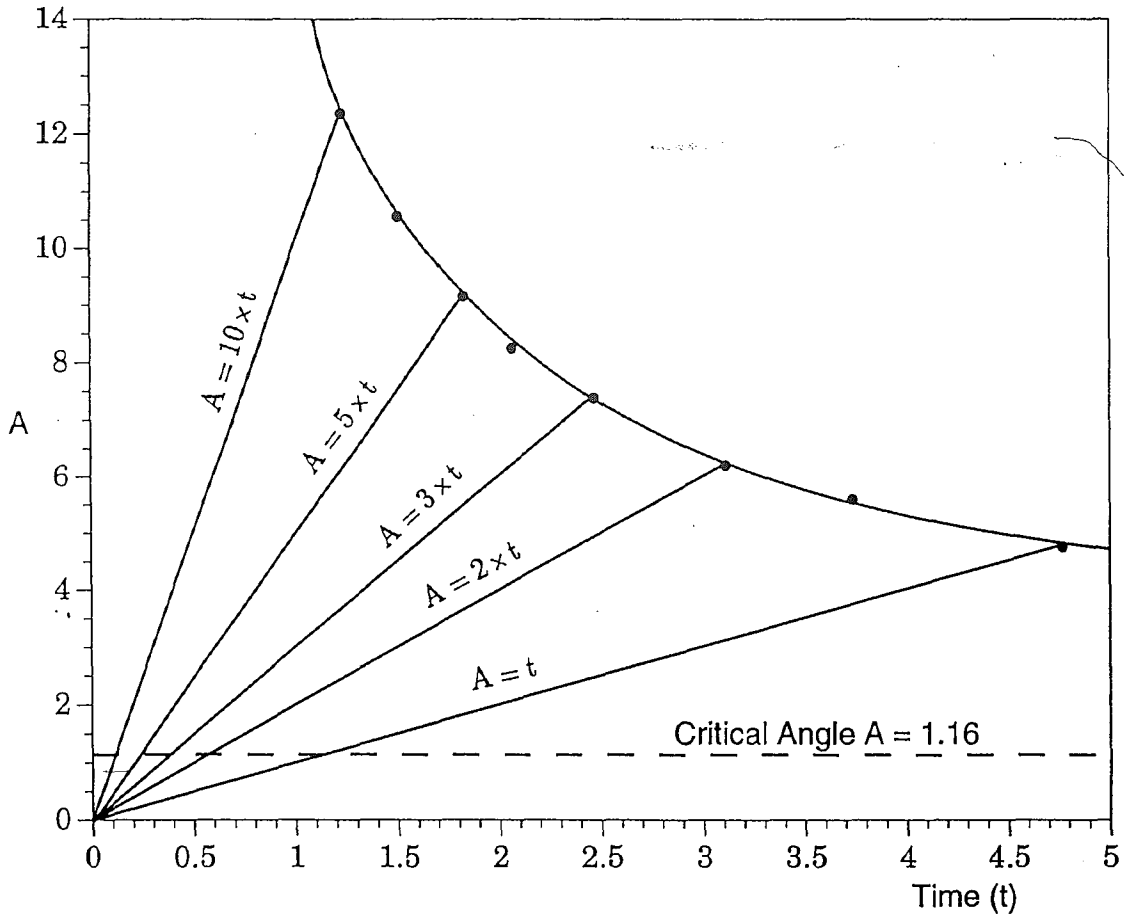

Figure 3.15 - Parameter A(t) vs time t for selected angles of attack

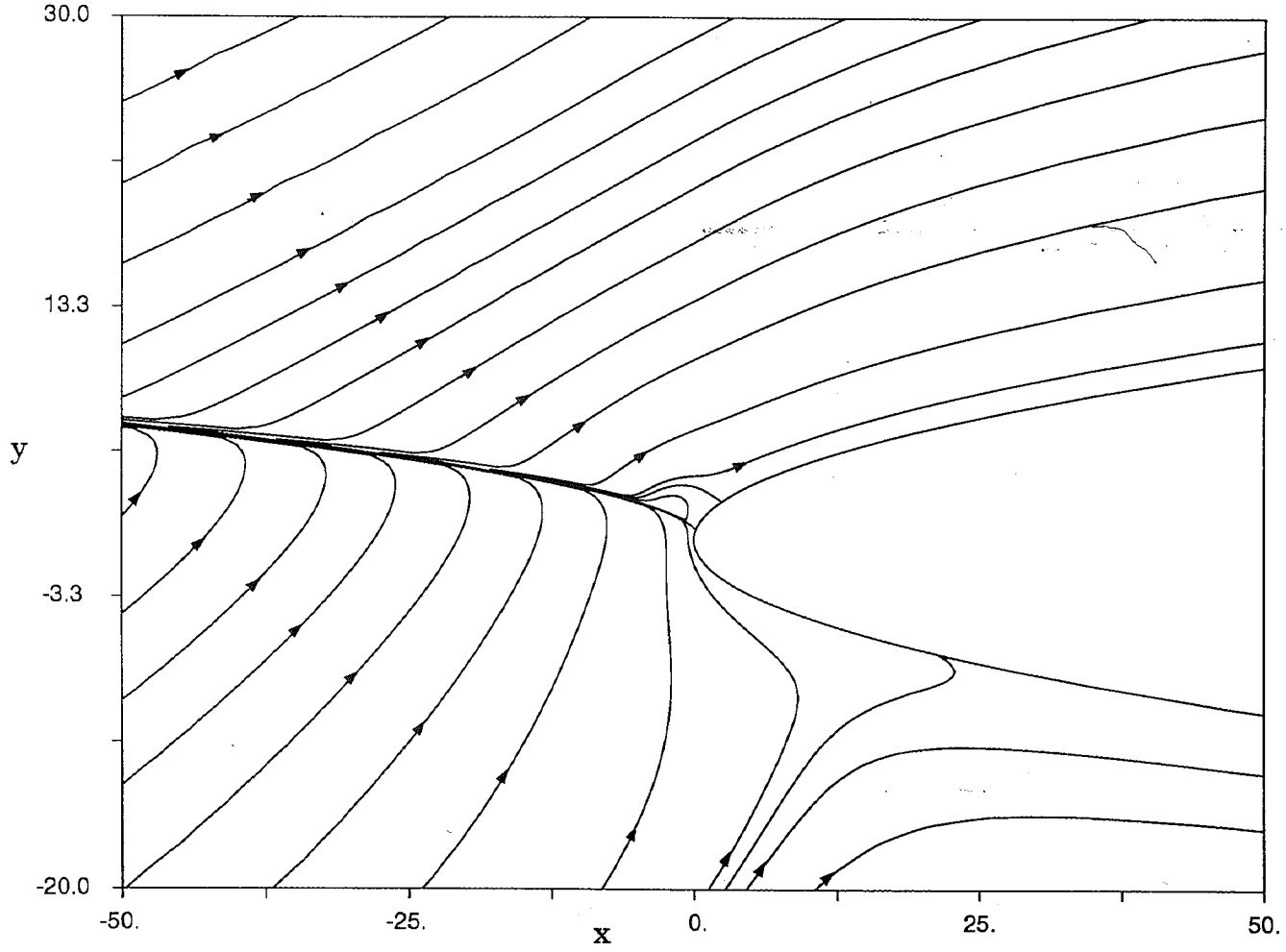

Figure 3.16 - Instantaneous streamlines for A(t) = 4.6 - 0.5 (t - 4.6)
at $t = t_s = 4.781$; $A(t_s) = 4.51$

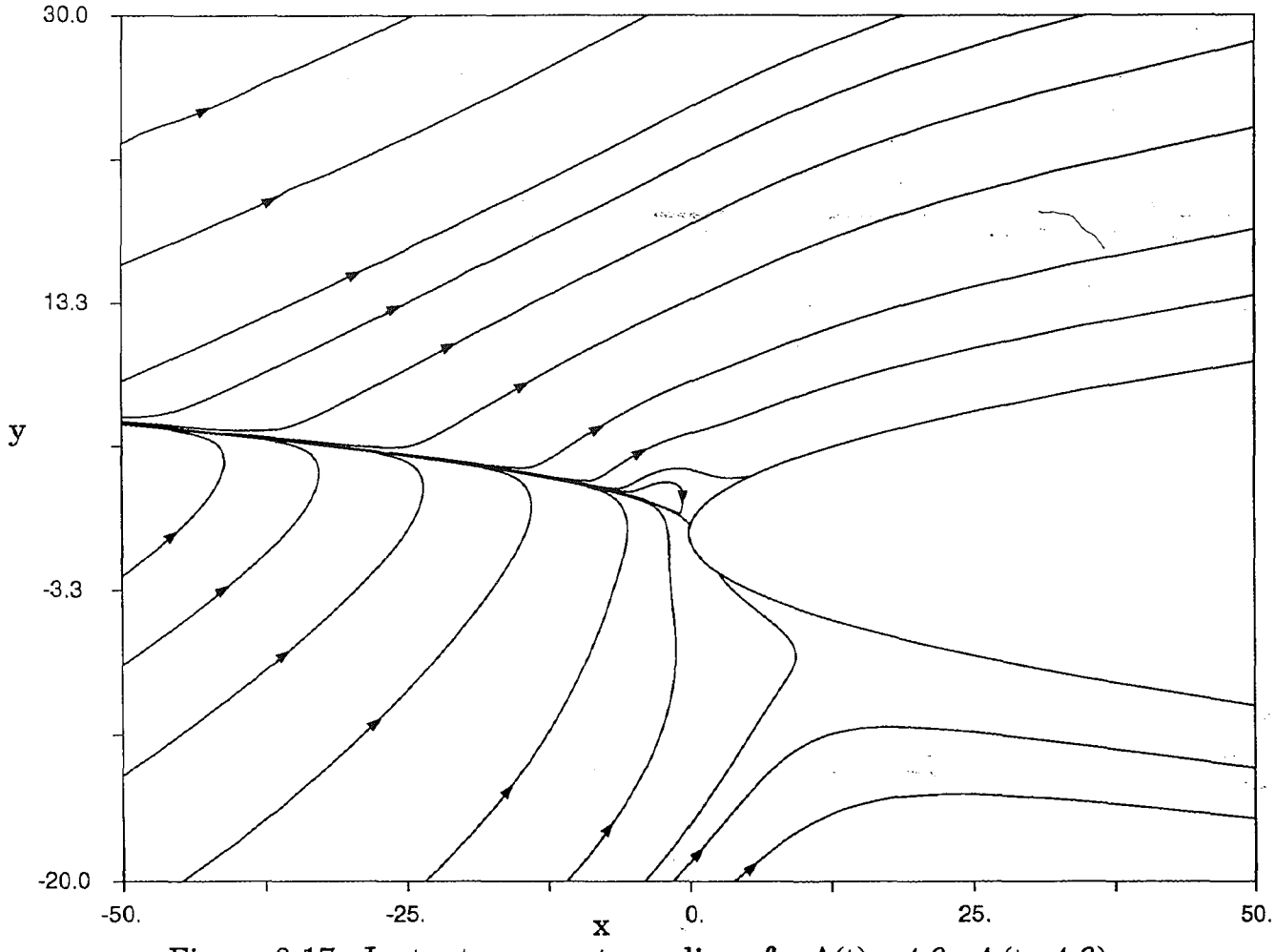

Figure 3.17 - Instantaneous streamlines for A(t) = 4.6 - 4 (t - 4.6)
at $t = t_s = 4.777$; $A(t_s) = 3.89$

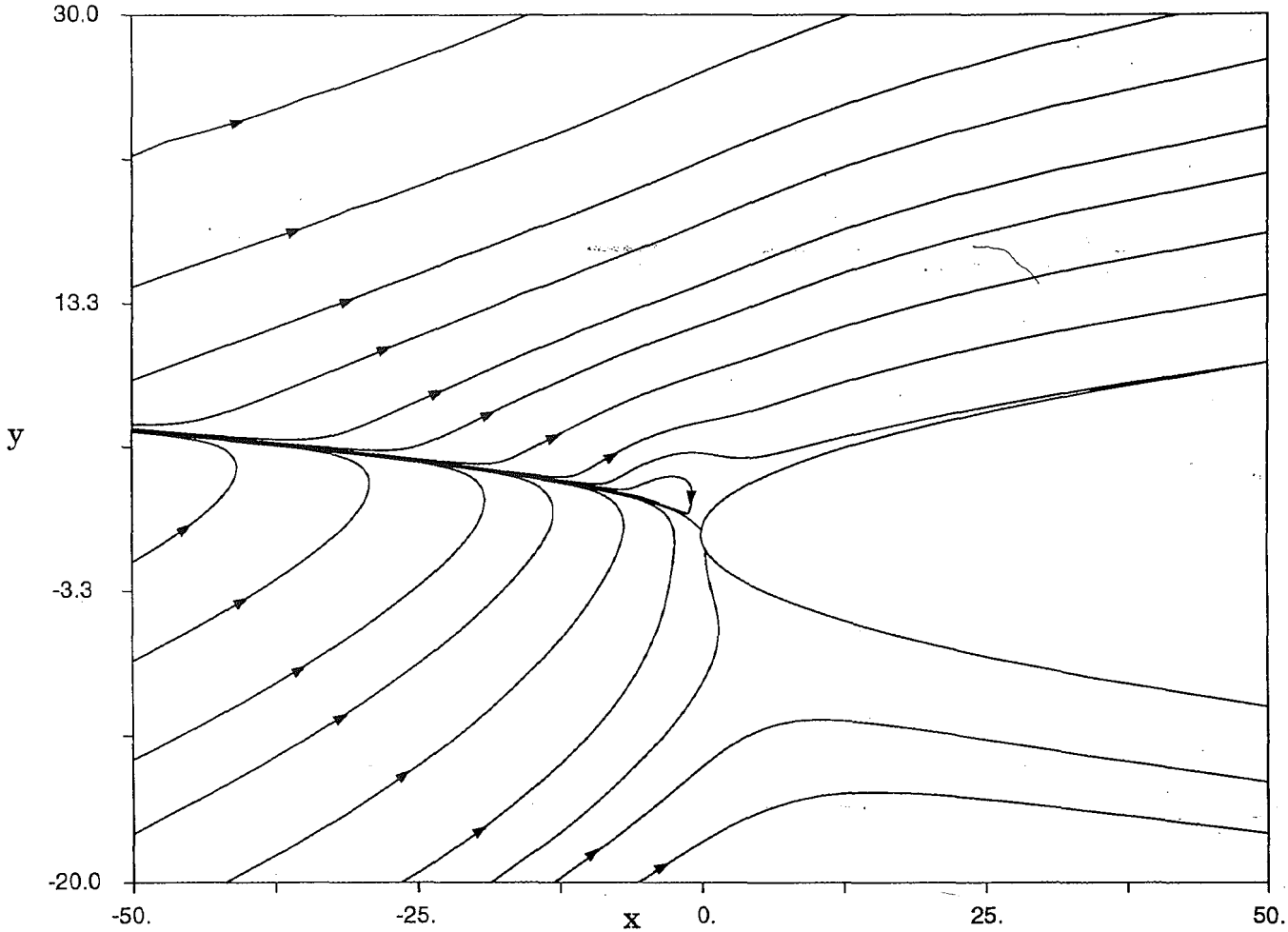

Figure 3.18 - Instantaneous streamlines for A(t) = 4.6 - 10 (t - 4.6)
at $t = t_s = 4.765$; $A(t_s) = 2.95$

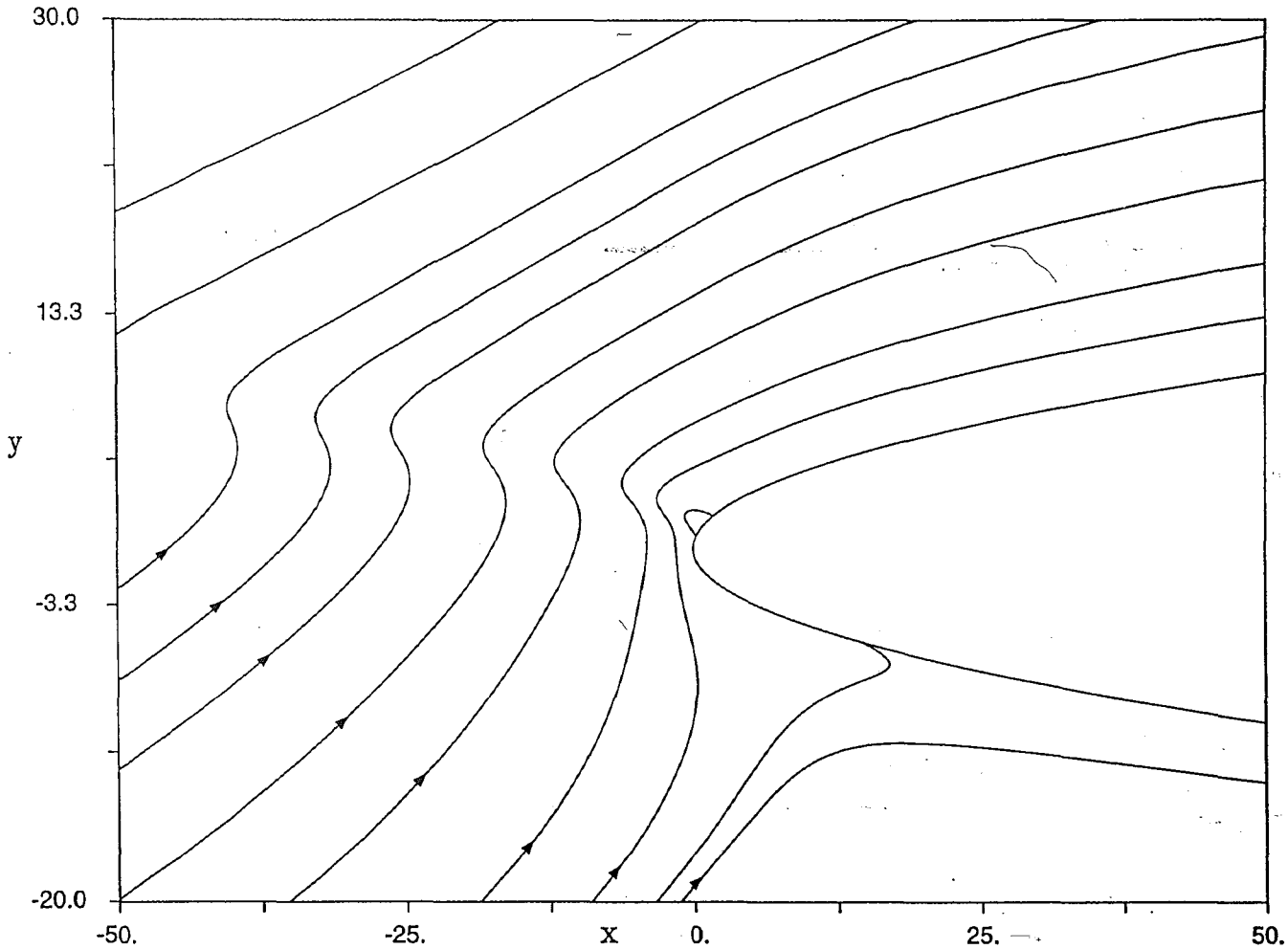

Figure 3.19 - Temporal development of the instantaneous streamline patterns for A(t) = 4.0 - (t - 4.0)

3.19 (a) t = 4.1; A = 3.9

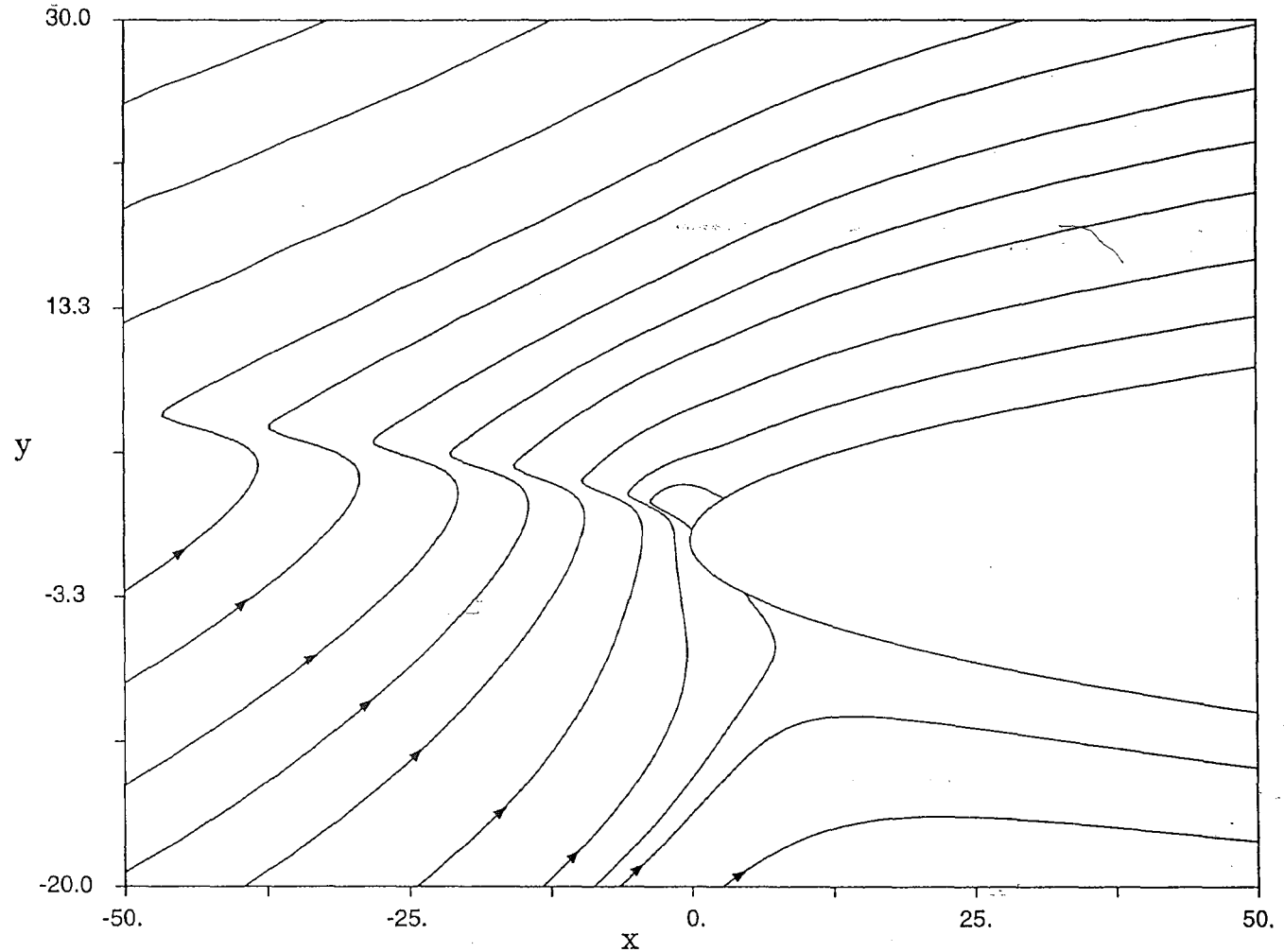

3.19 (b) t = 4.5; A = 3.5

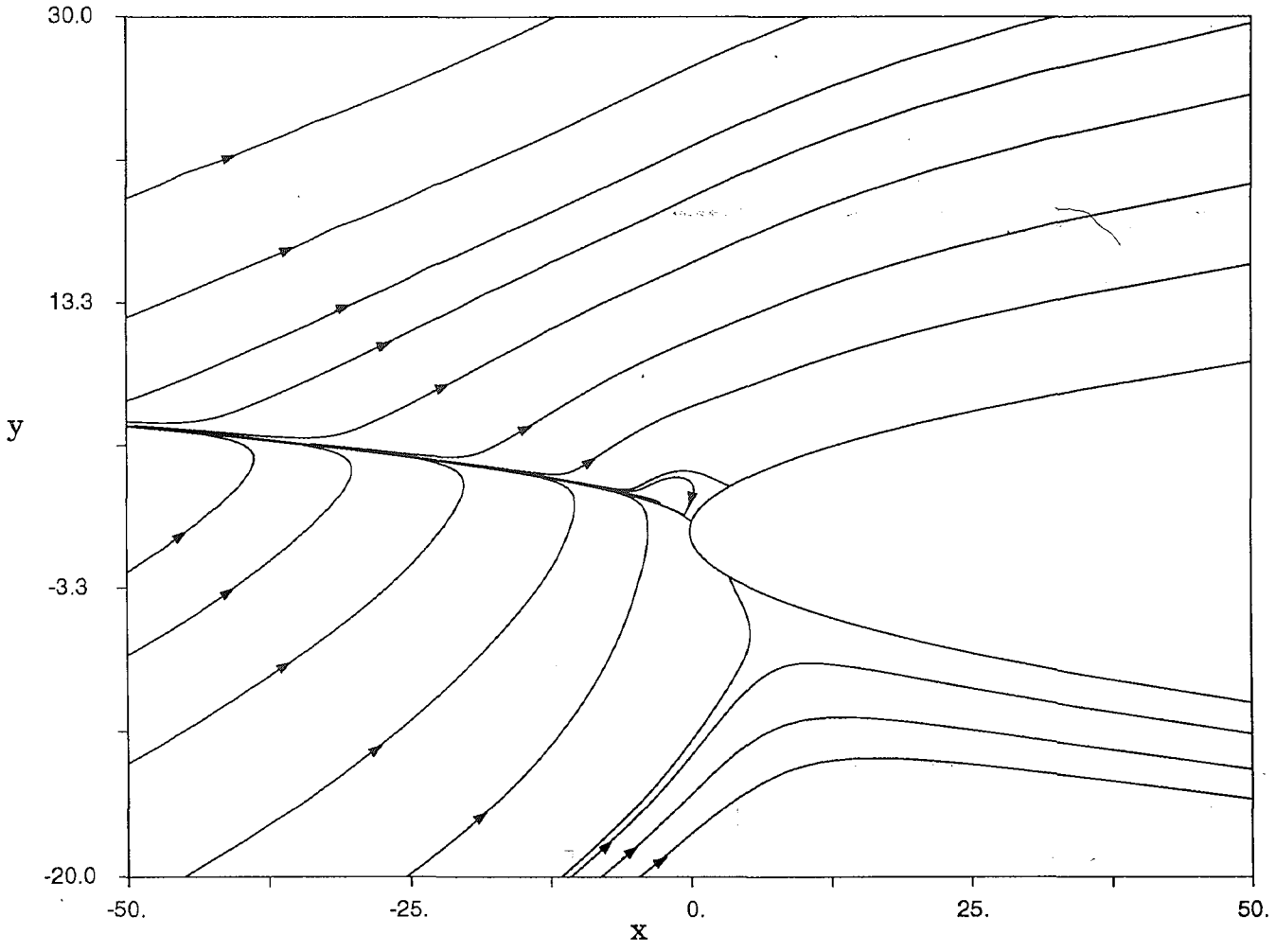

3.19 (c) $t = t_s = 4.69$; $A = 3.31$

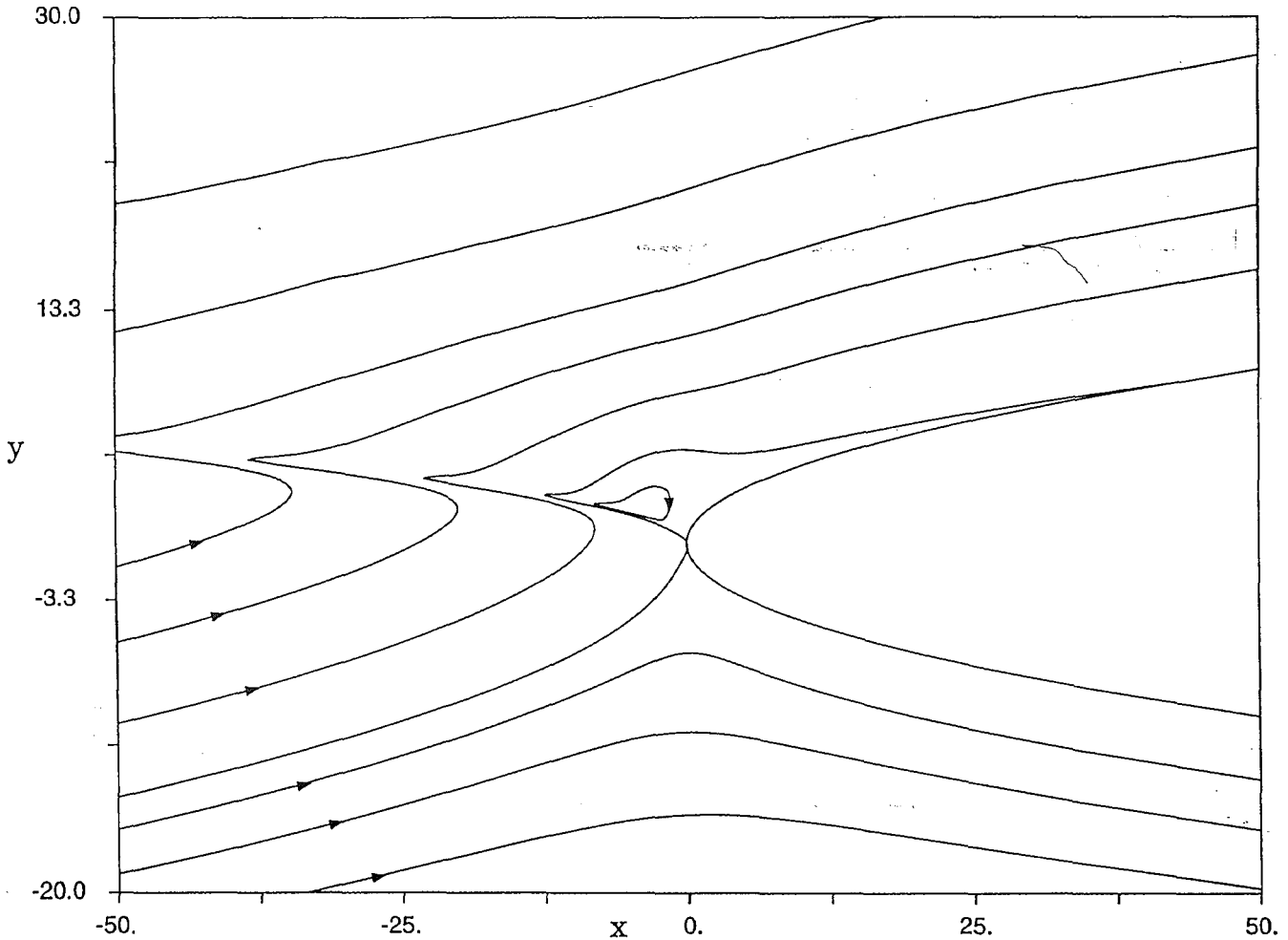

Figure 3.20 - Temporal development of the instantaneous streamline patterns for A(t) = 4.0 - 5 (t - 4.0)

3.20 (a) t = 4.5; A = 1.5

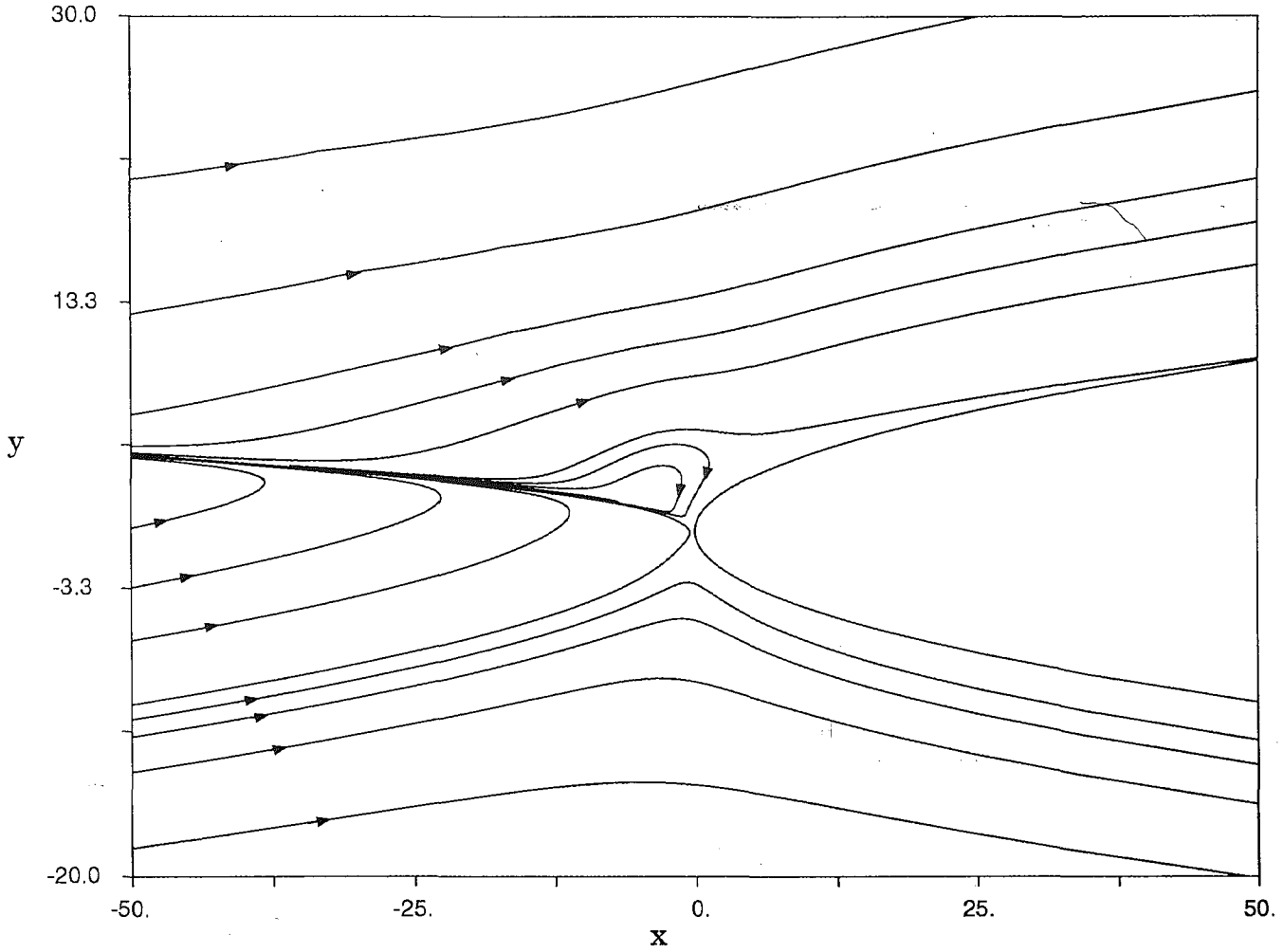

3.20 (b) $t = t_s = 4.588$; $A = 1.06$

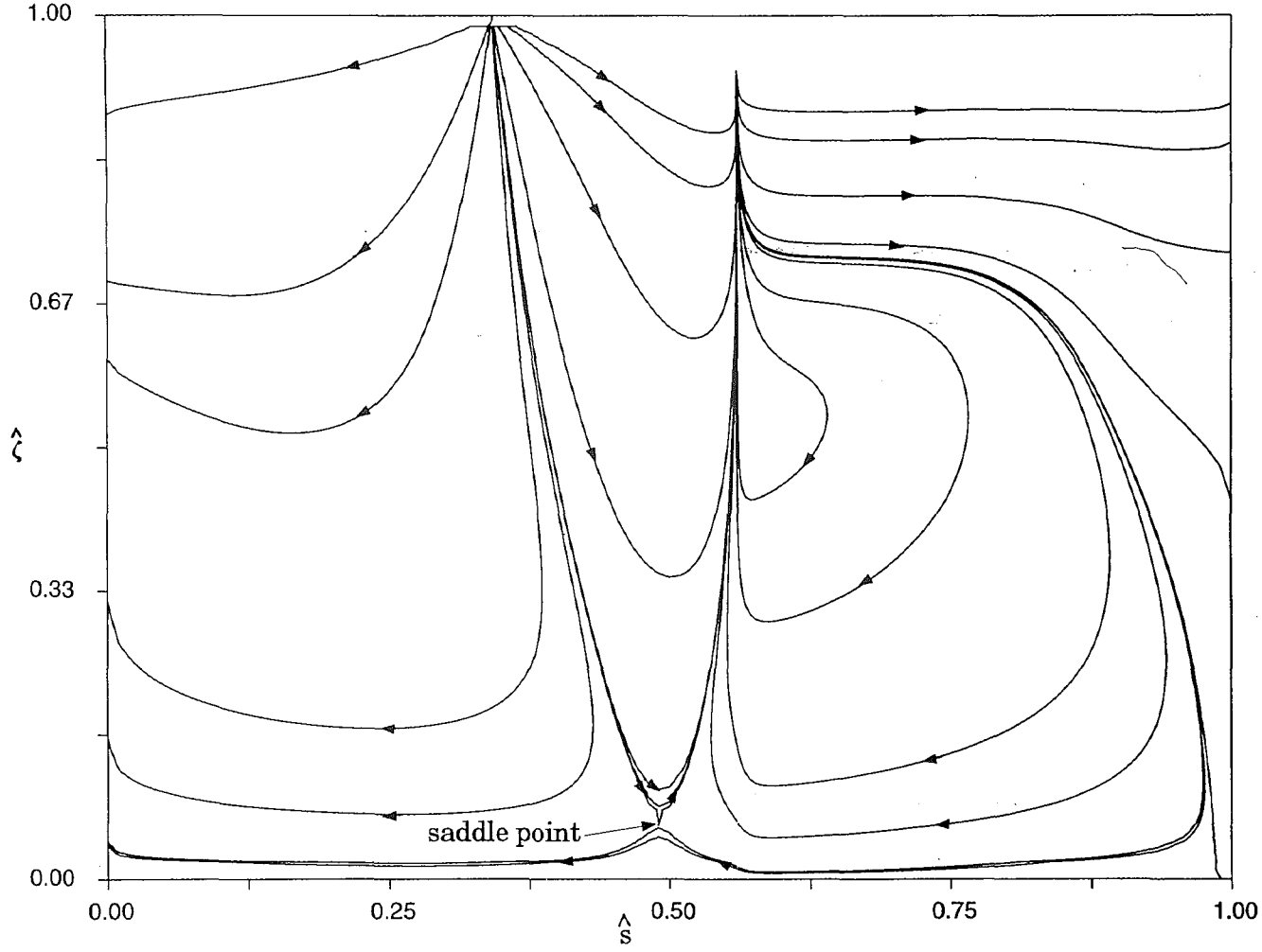

3.20 (c) computational domain: $t = t_s = 4.588$; $A = 1.06$

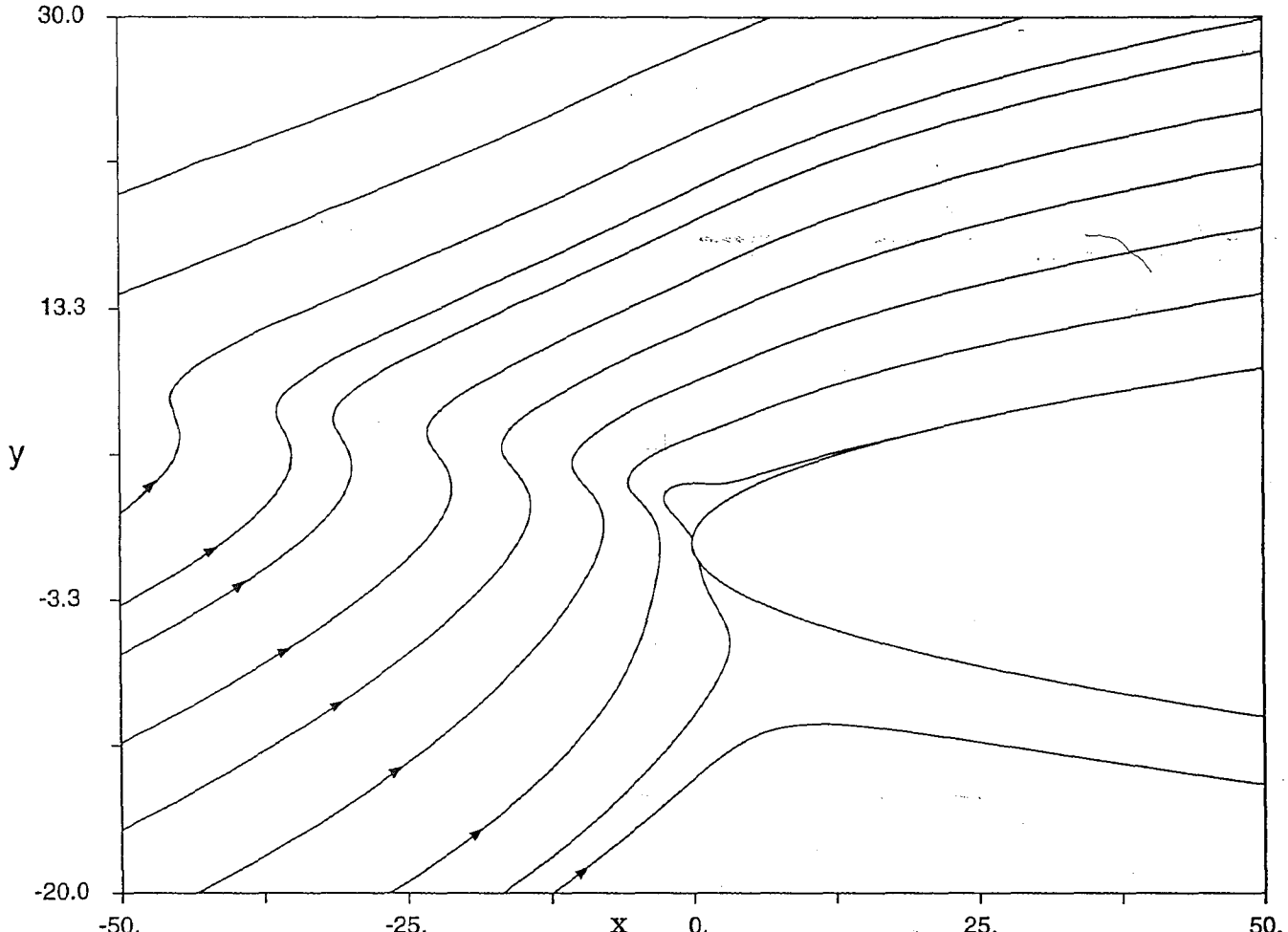

Figure 3.21 - Temporal development of the instantaneous streamline patterns for A(t) = 4.0 - 10 (t - 4.0)

3.21 (a) t = 4.1; A = 3.0

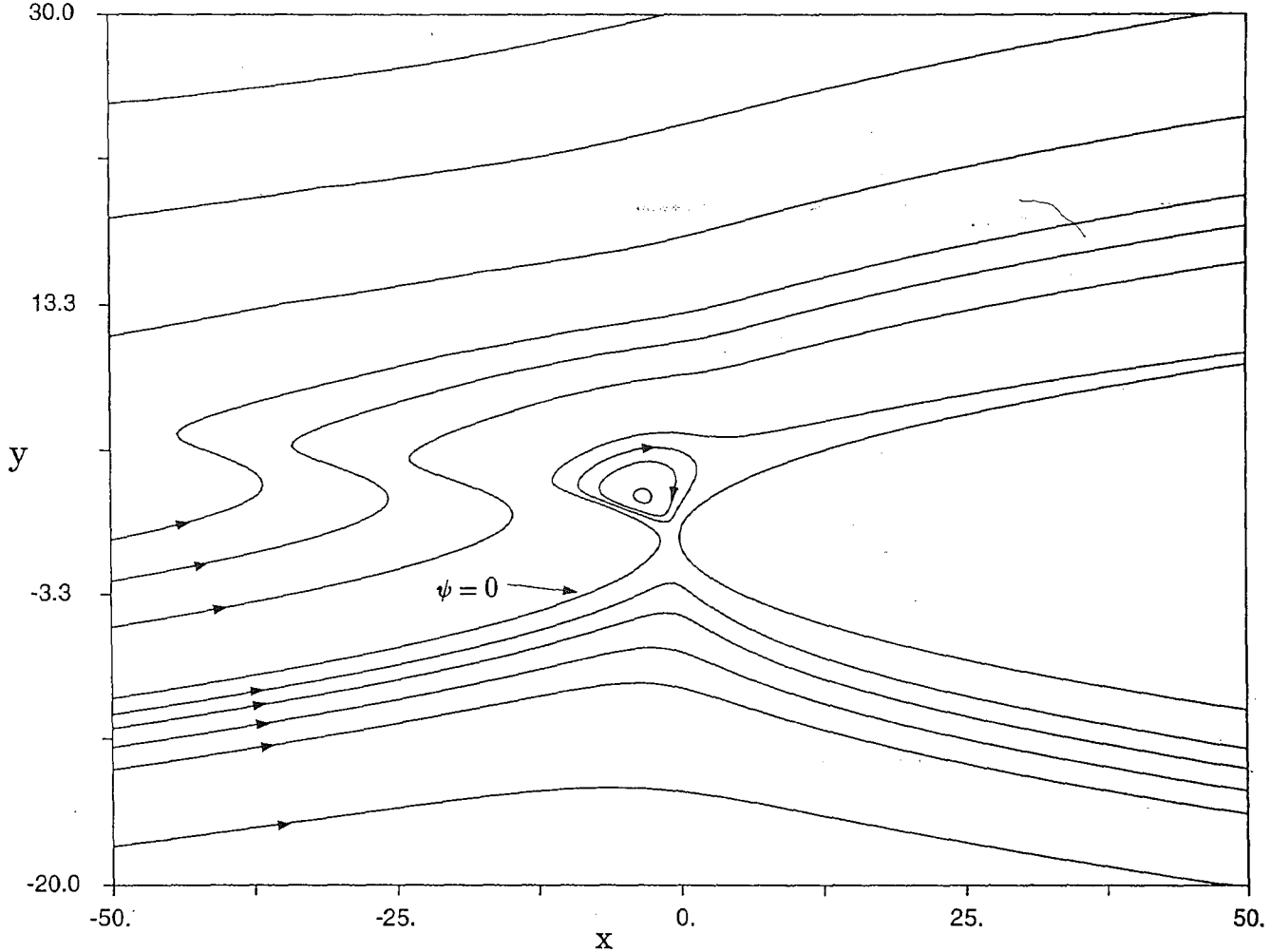

3.21 (b) t = 4.3; A = 1.0

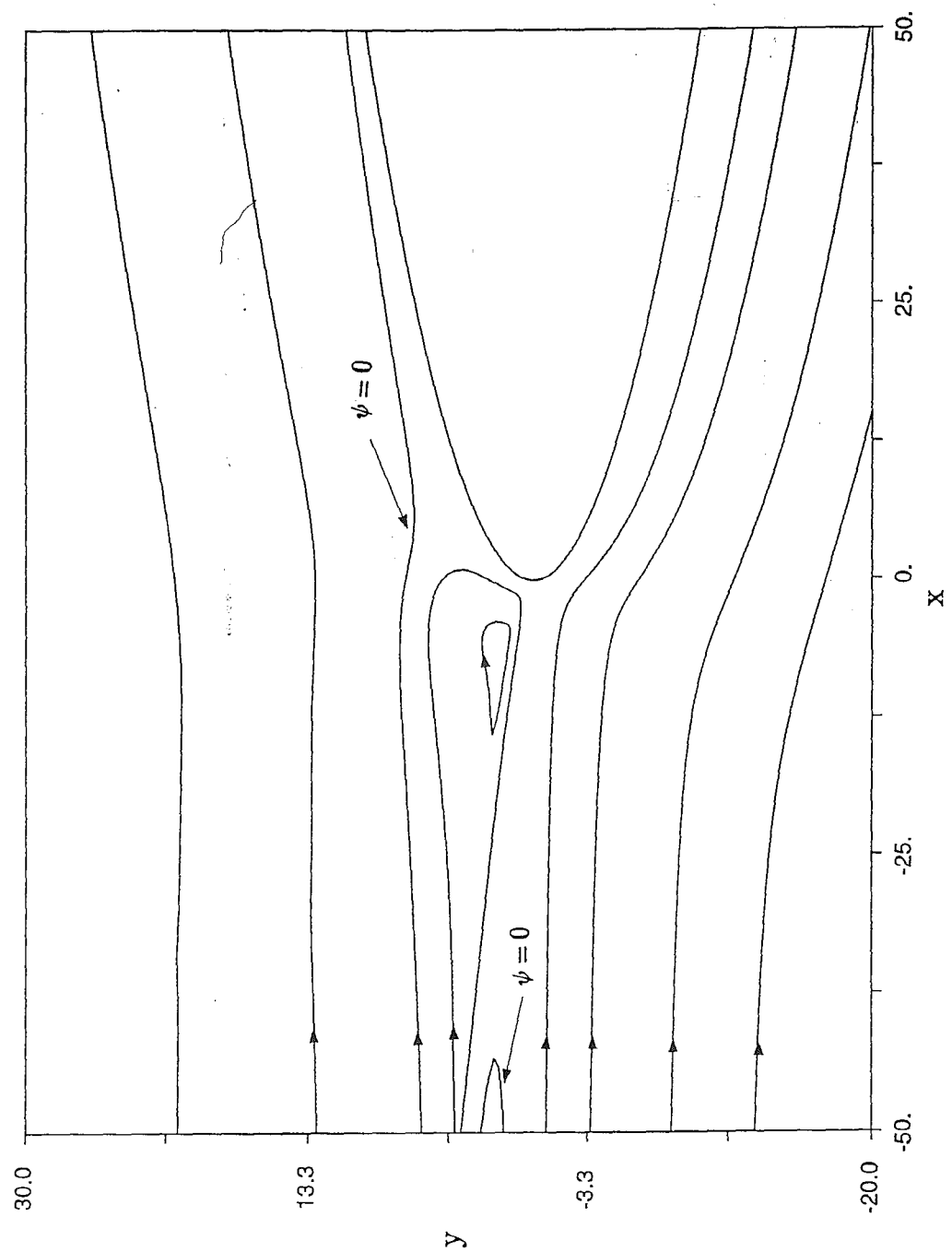

3.21 (c) t = 4.4; A = 0.0

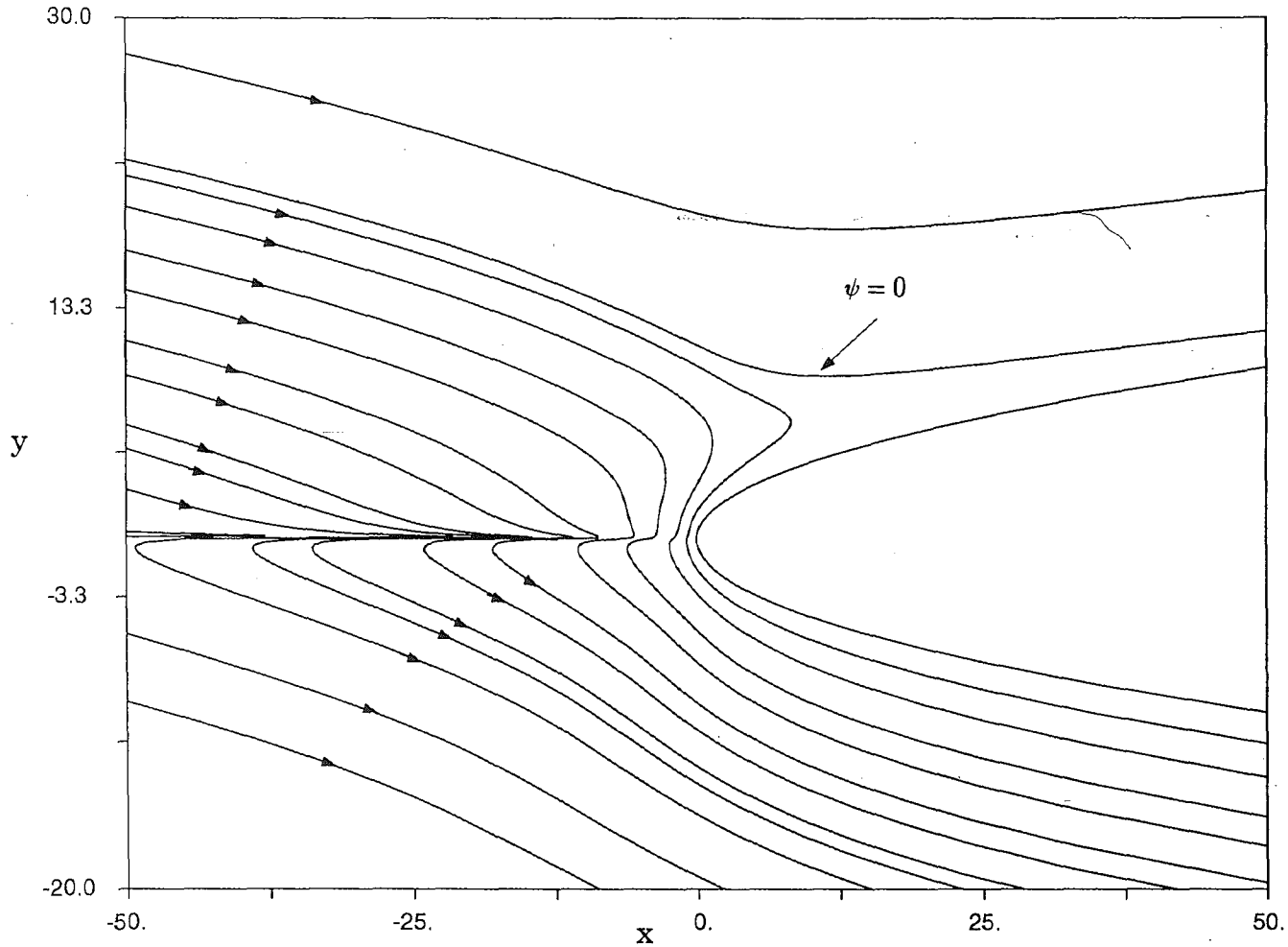

3.21 (d) $t = t_s = 4.559$; $A = -1.59$

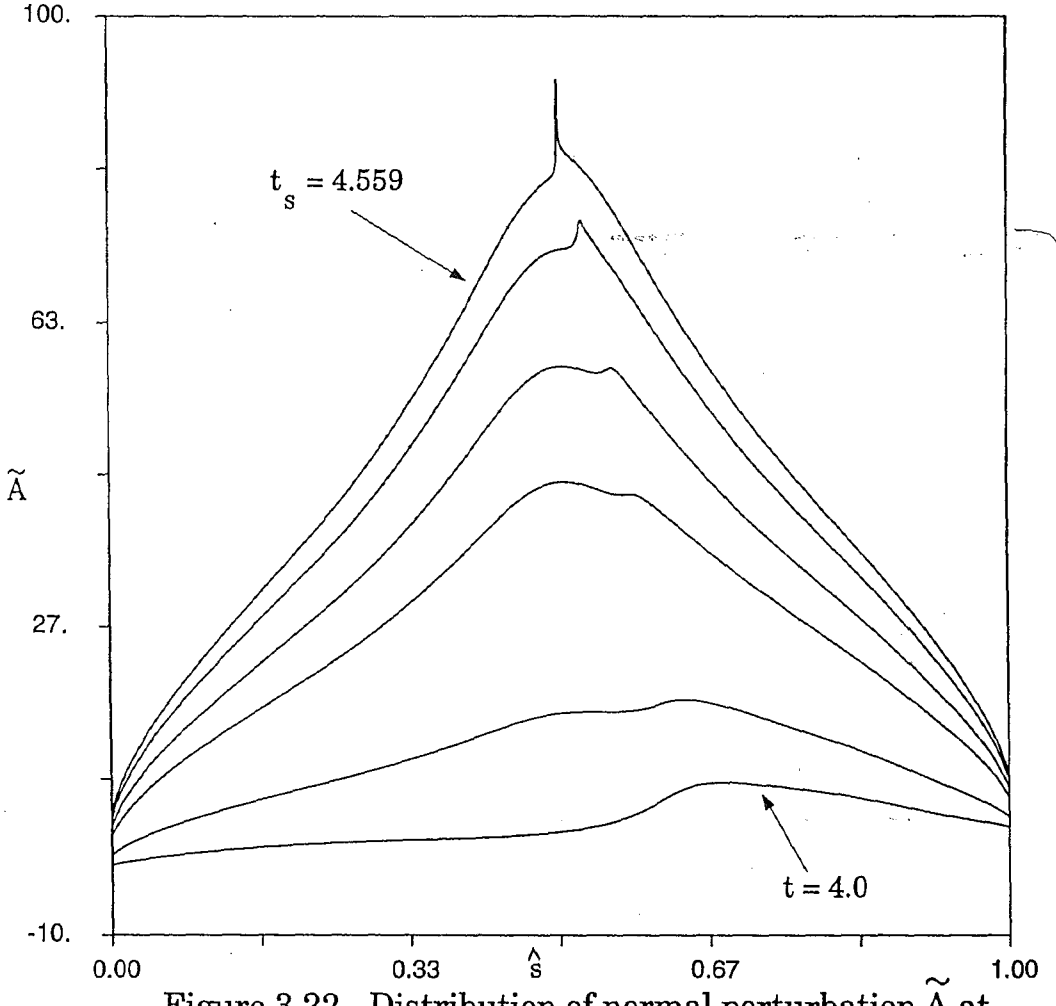

Figure 3.22 - Distribution of normal perturbation $\tilde{A}$ at selected times for A(t) = 4.0 - 10 (t - 4.0): t = 4.0, 4.1, 4.3, 4.4, 4.5, 4.559

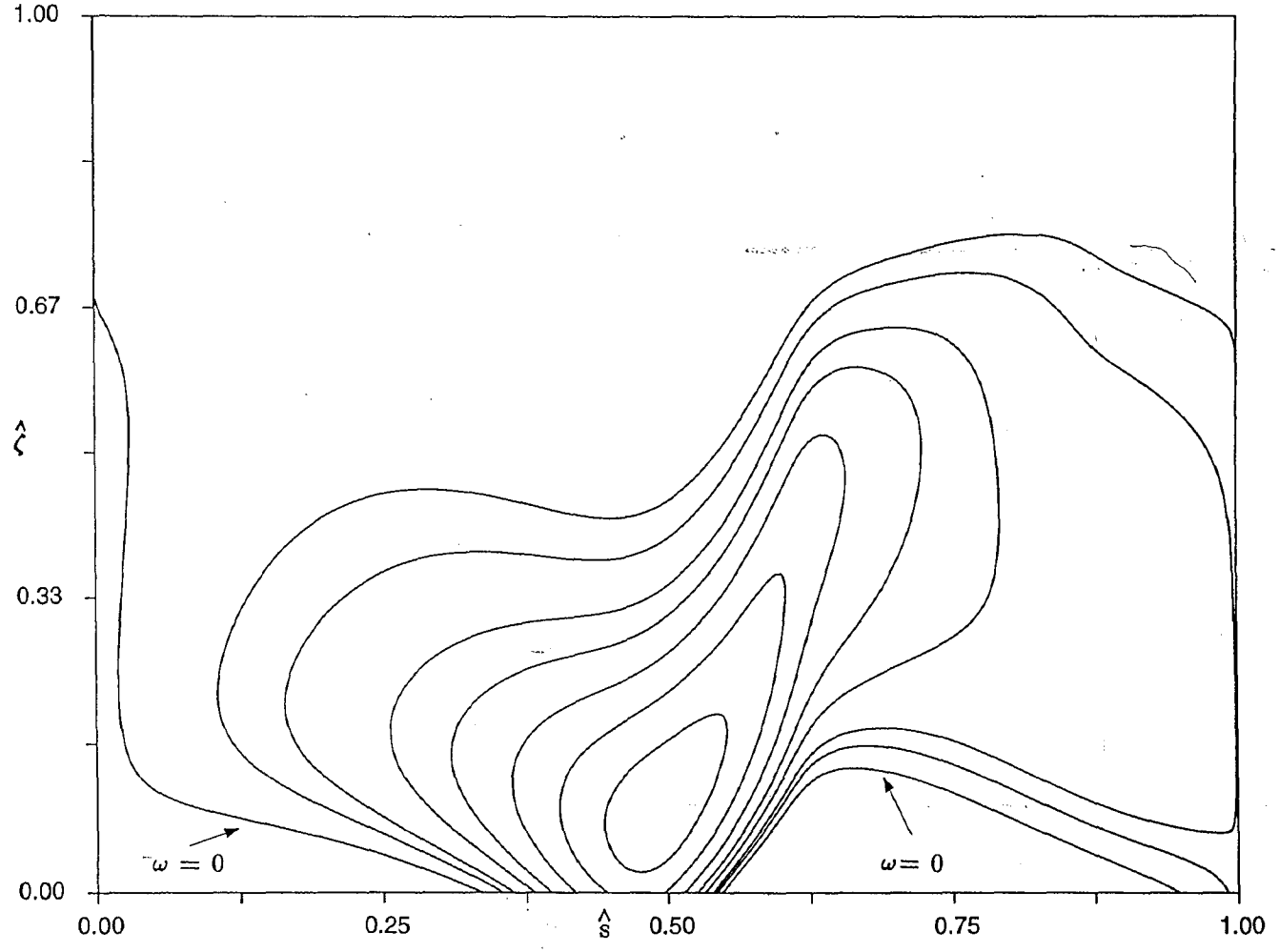

Figure 3.23 - Evolution of the constant vorticity contours in computational coordinates for A(t) = 4.0 - 10 (t - 4.0)

3.23 (a) t = 4.1; A = 3.0

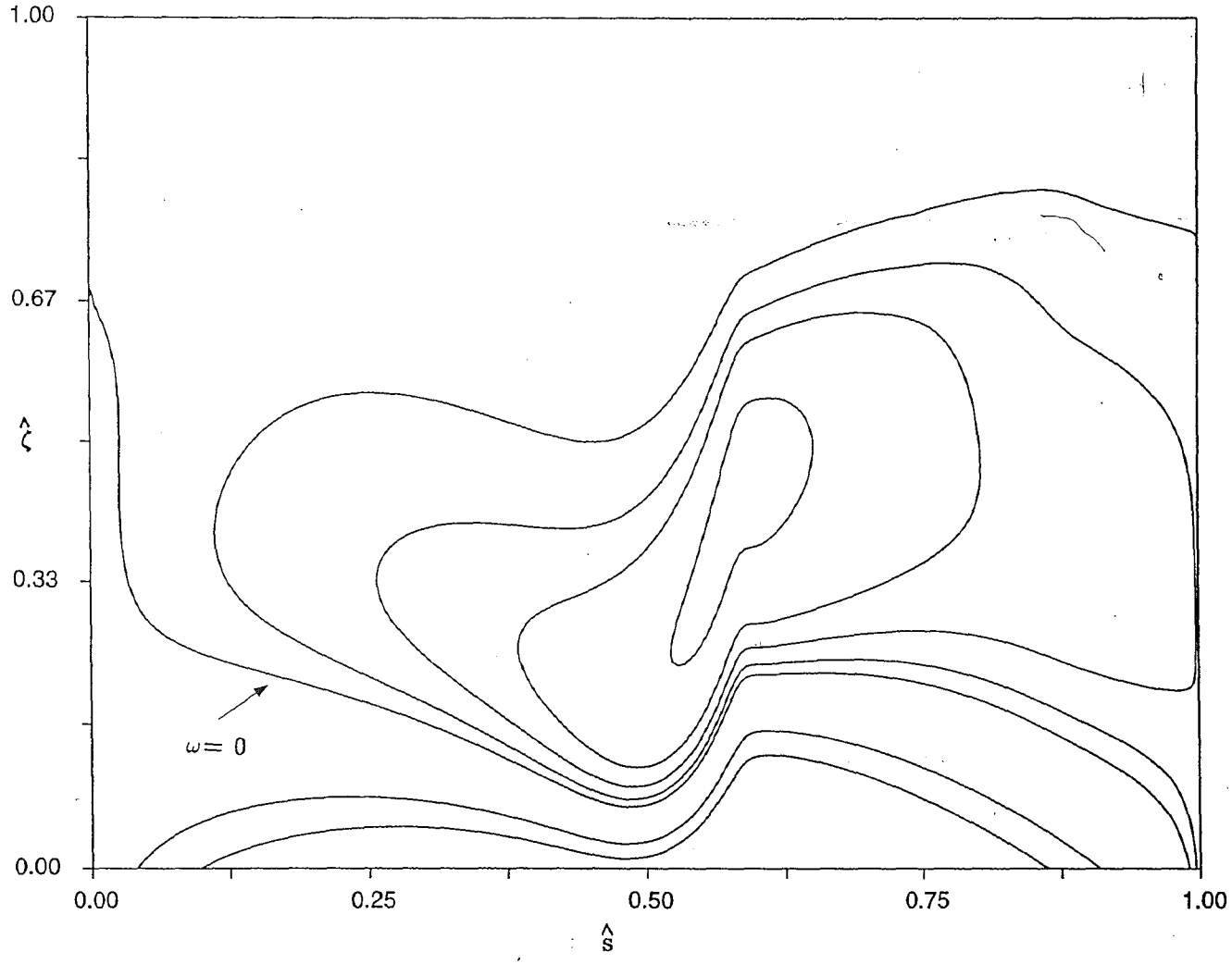

3.23 (b) t = 4.3; A = 1.0

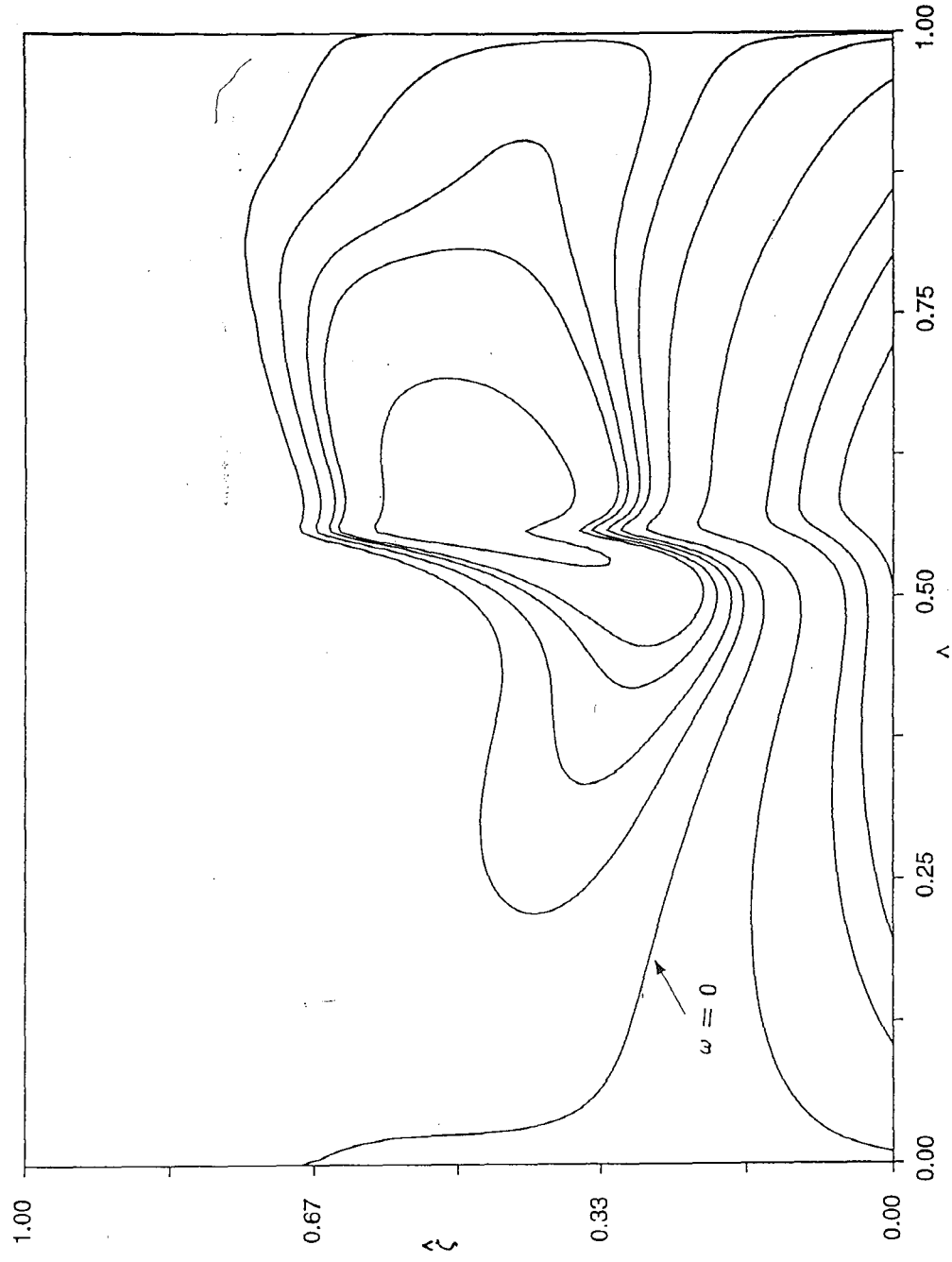

3.23 (c) t = 4.4; A = 0.0

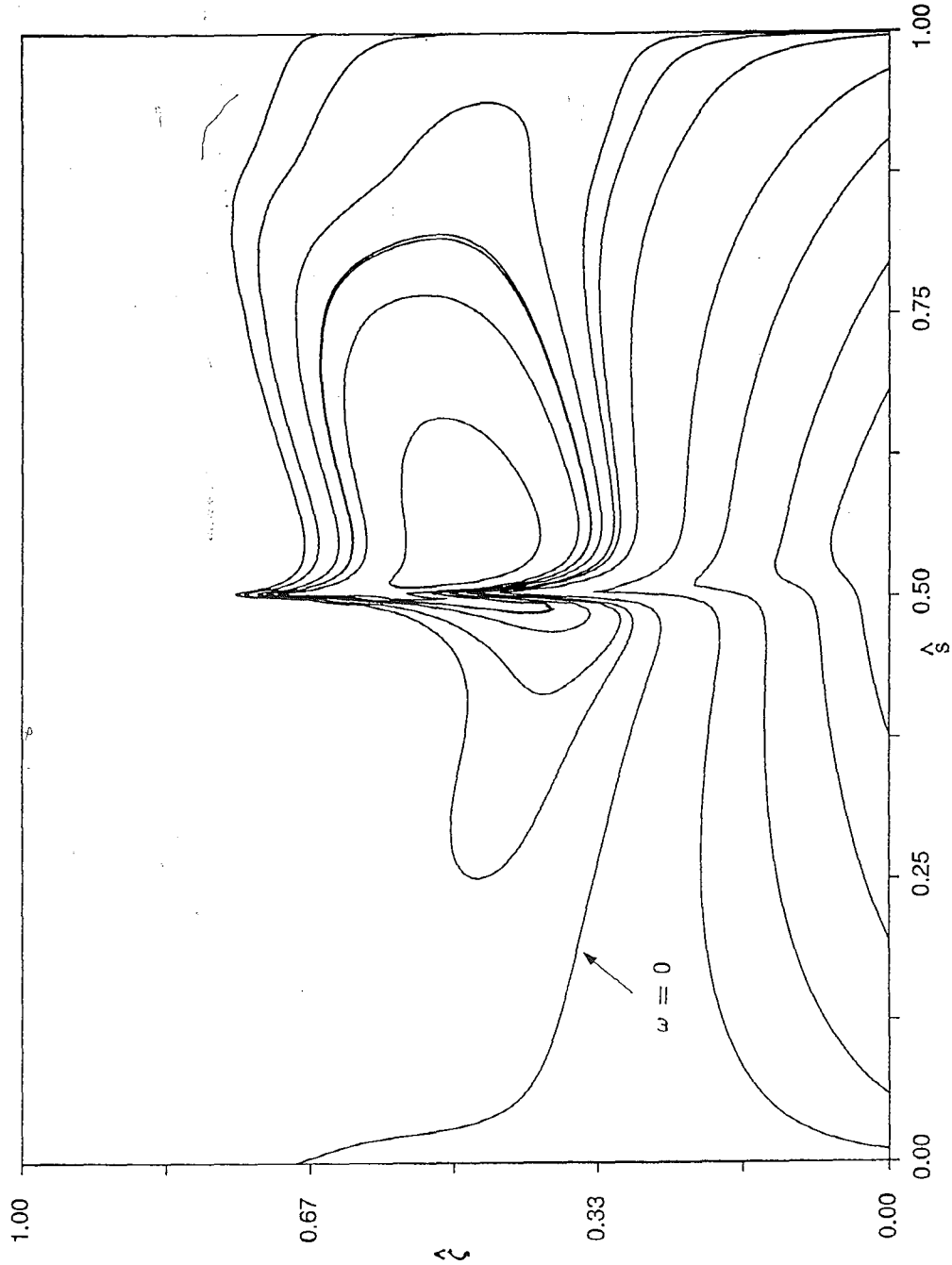

3.23 (d) $t = t_s = 4.559$; $A = -1.59$

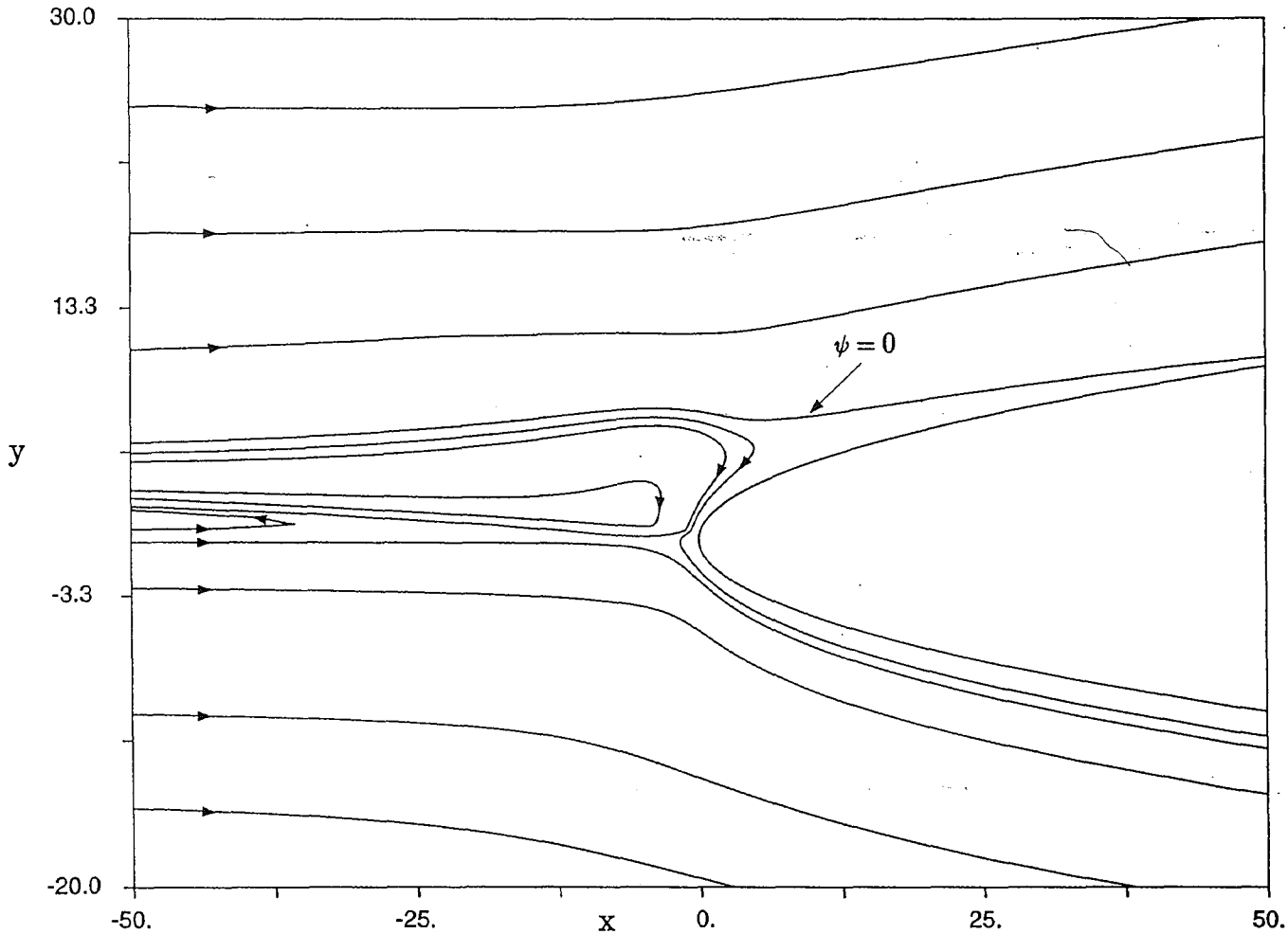

Figure 3.24 - Temporal development of the instantaneous streamline patterns for A(t) = 4.0 - 10 (t - 4.0) when t < 4.4; A(t) = 0.0 when t ≥ 4.4

3.24 (a) t = 4.5

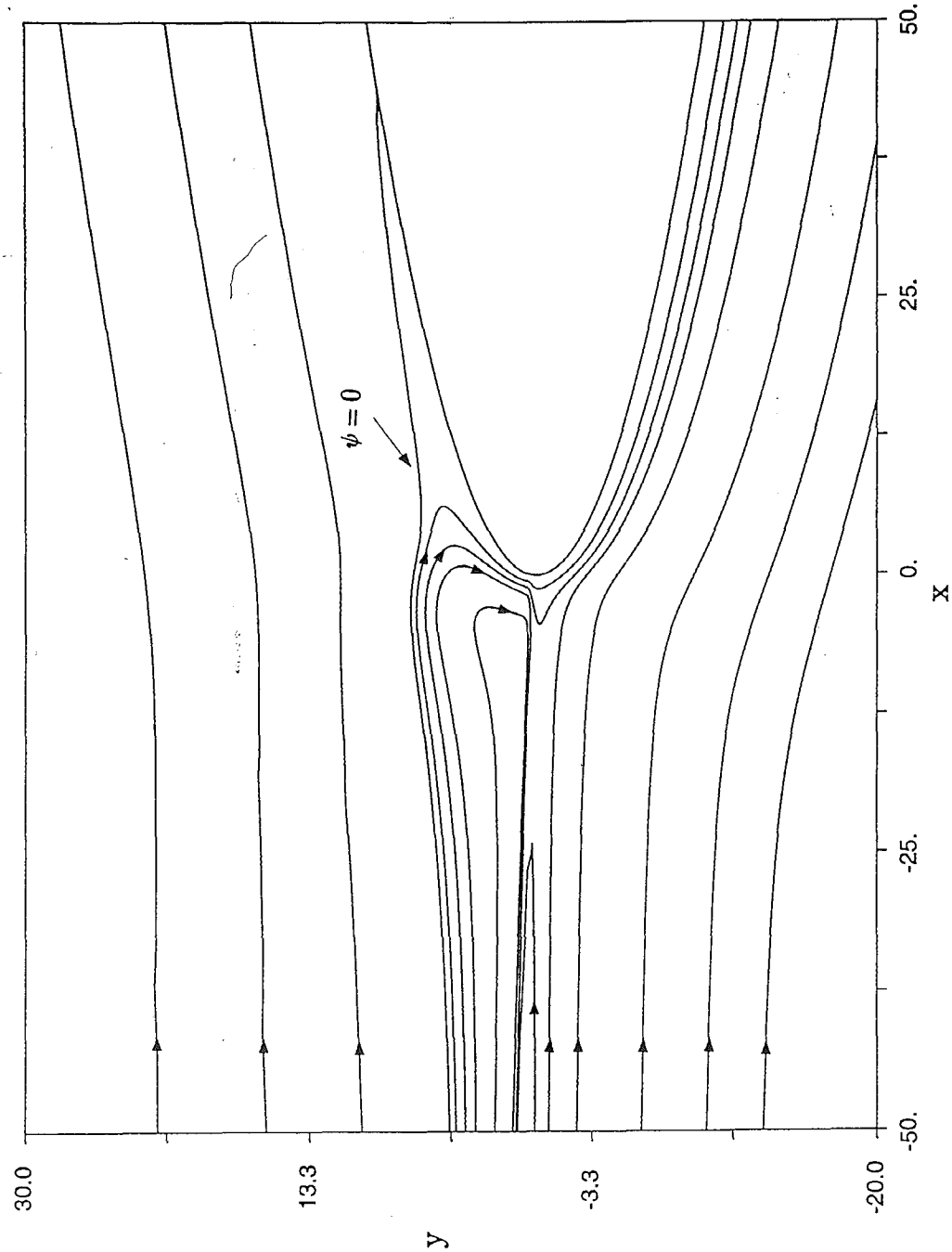

3.24 (b) $t = t_s = 4.556$

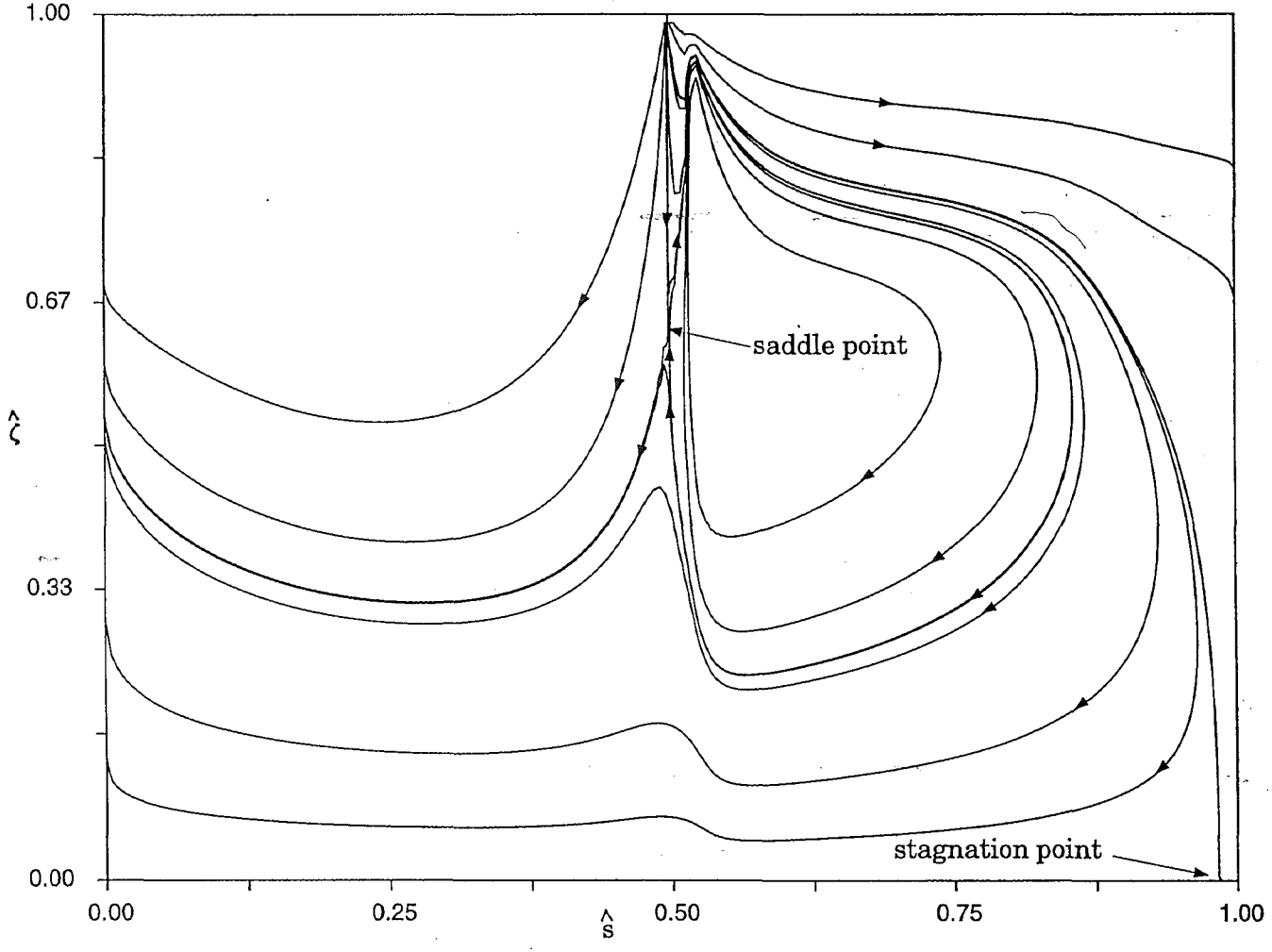

Figure 3.25 - Instantaneous streamlines in computational coordinates at $t = t_s = 4.556$; $A = 0.0$

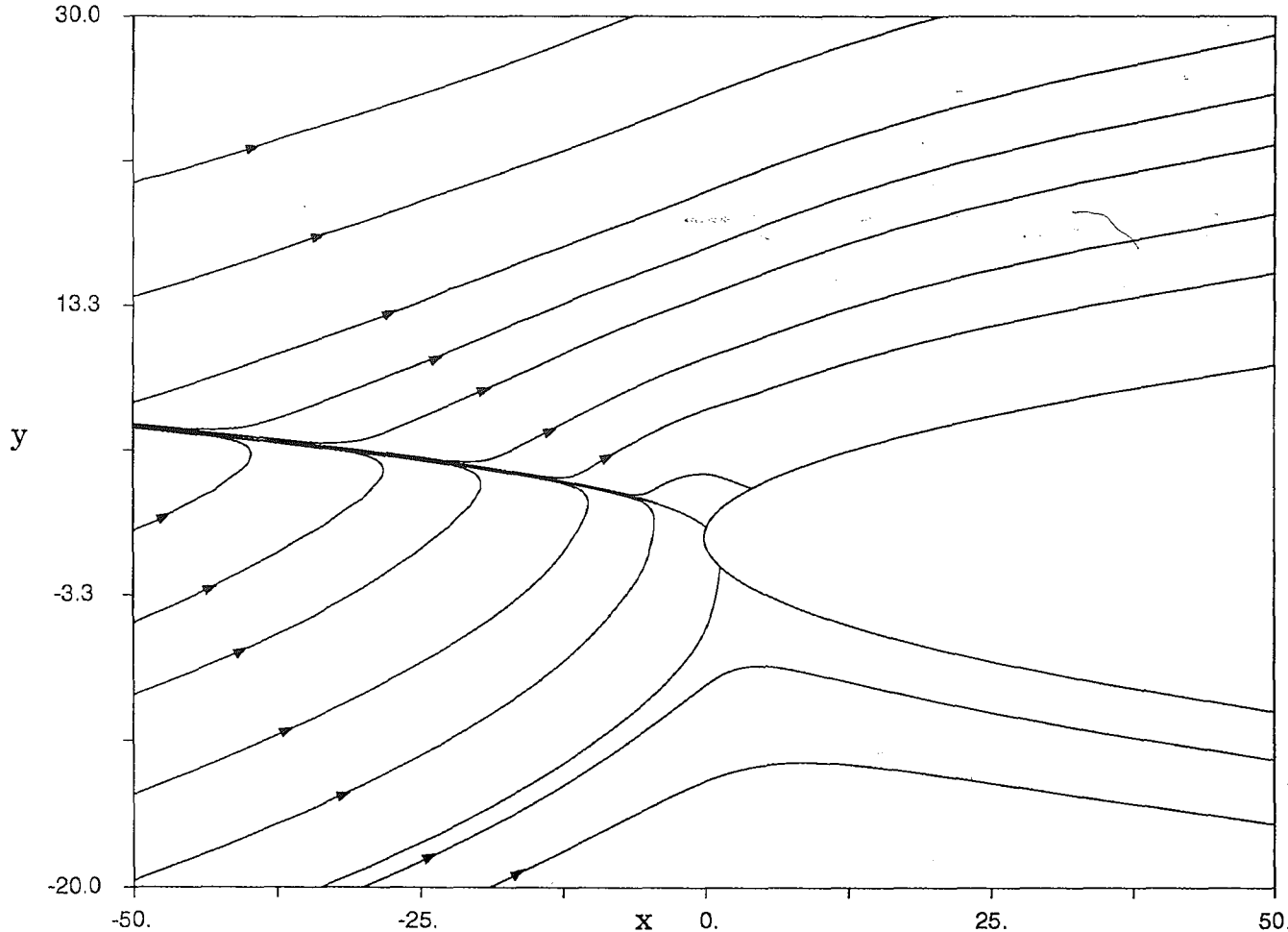

Figure 3.26 - Instantaneous streamlines for A(t) = 3.5 - (t - 3.5)
at $t = t_s = 4.657$; $A(t_s) = 2.34$

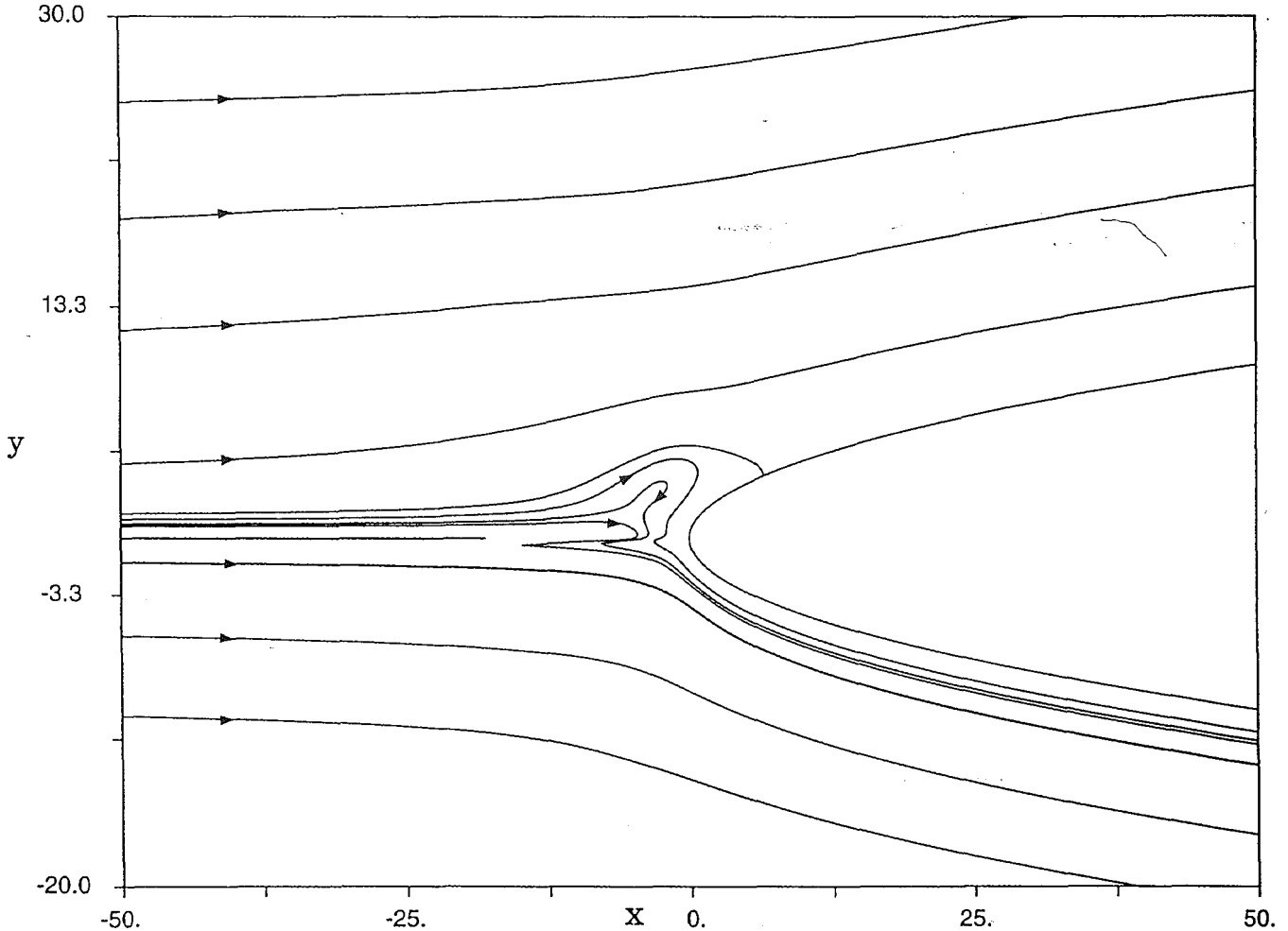

Figure 3.27 - Instantaneous streamlines at $t = t_s = 4.616$ for
$A(t) = 3.5 - 10\,(t - 3.5)$ when $t < 3.85$;
$A(t) = 0.0$ when $t \geq 3.85$

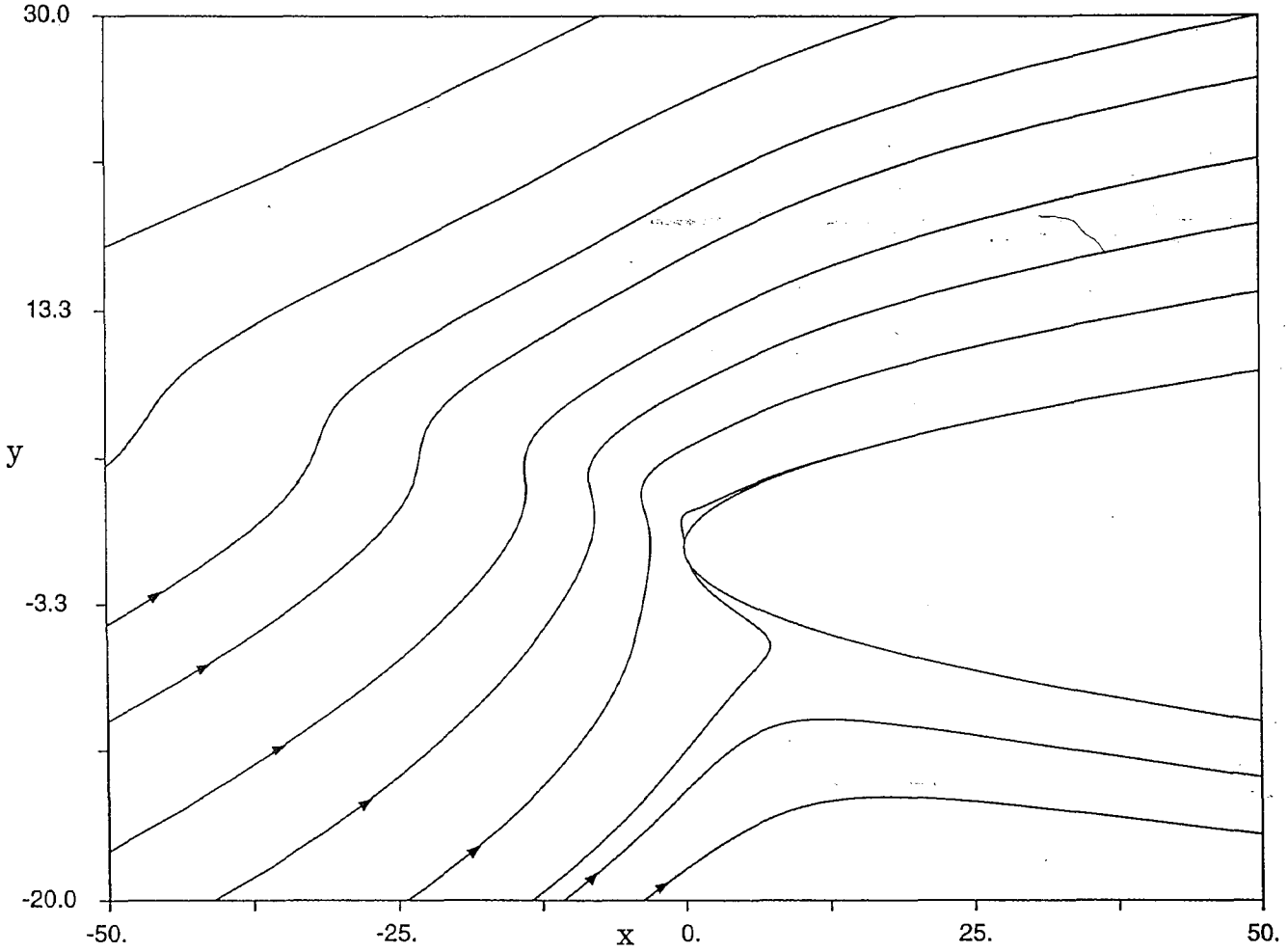

Figure 3.28 - Temporal development of the instantaneous streamline patterns for $A(t) = 3.5 - 35\,(t - 3.5)$ when $t < 3.6$; $A(t) = 0.0$ when $t \geq 3.6$

3.28 (a) $t = 3.51$; $A = 3.15$

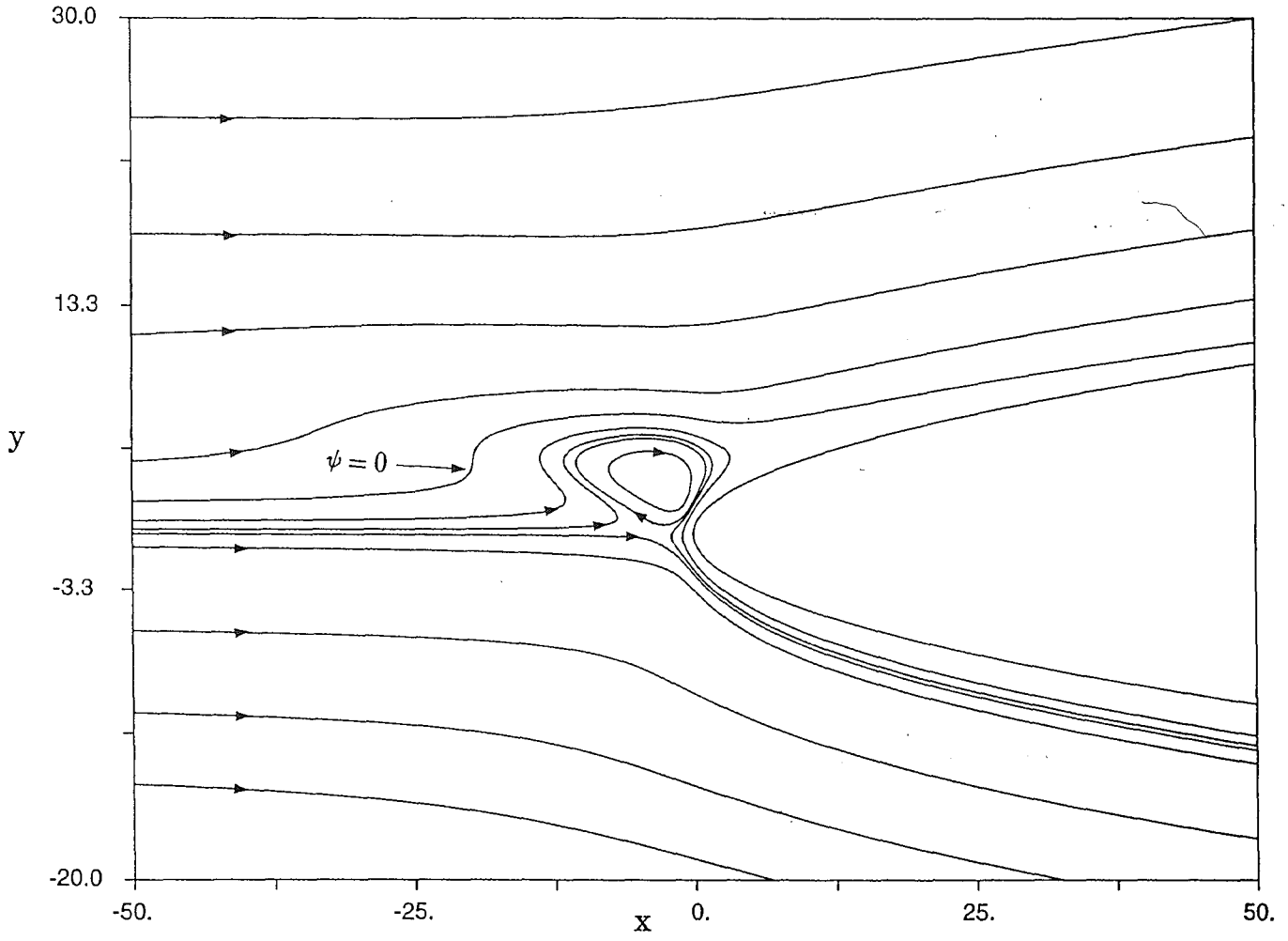

3.28 (b) t = 3.6; A = 0.0

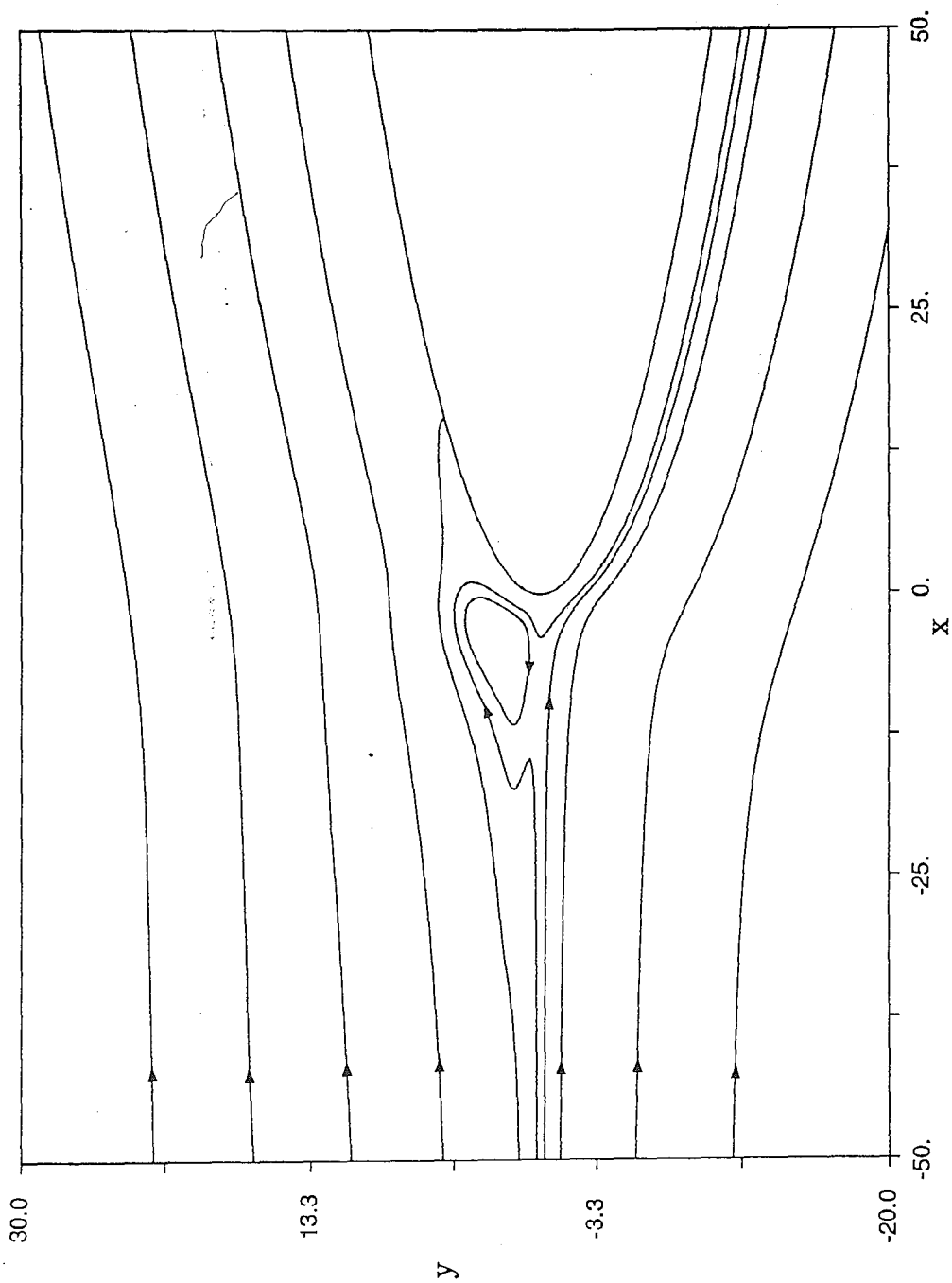

3.28 (c) t = 4.0; A = 0.0

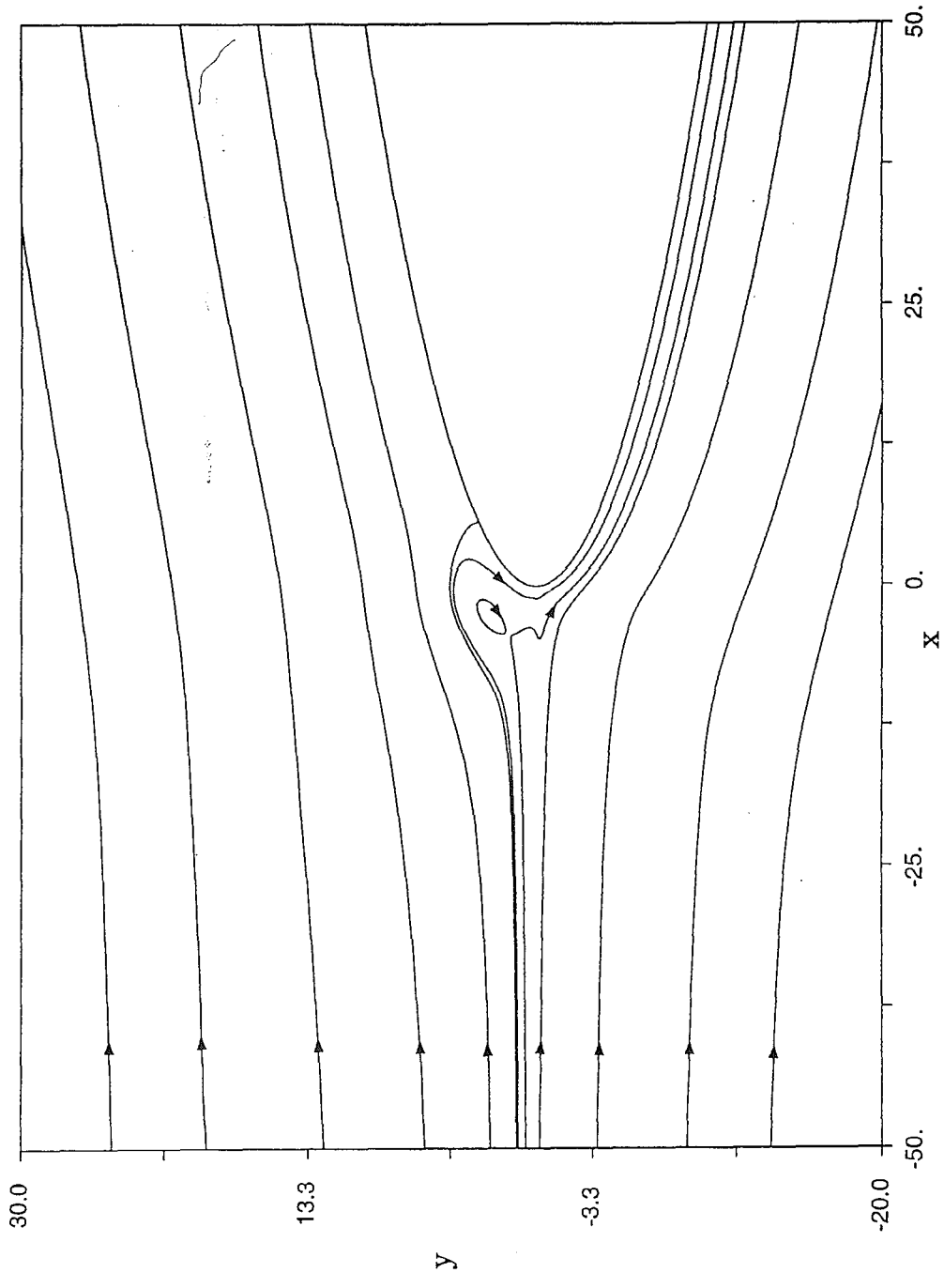

3.28 (d) t = 4.5; A = 0.0

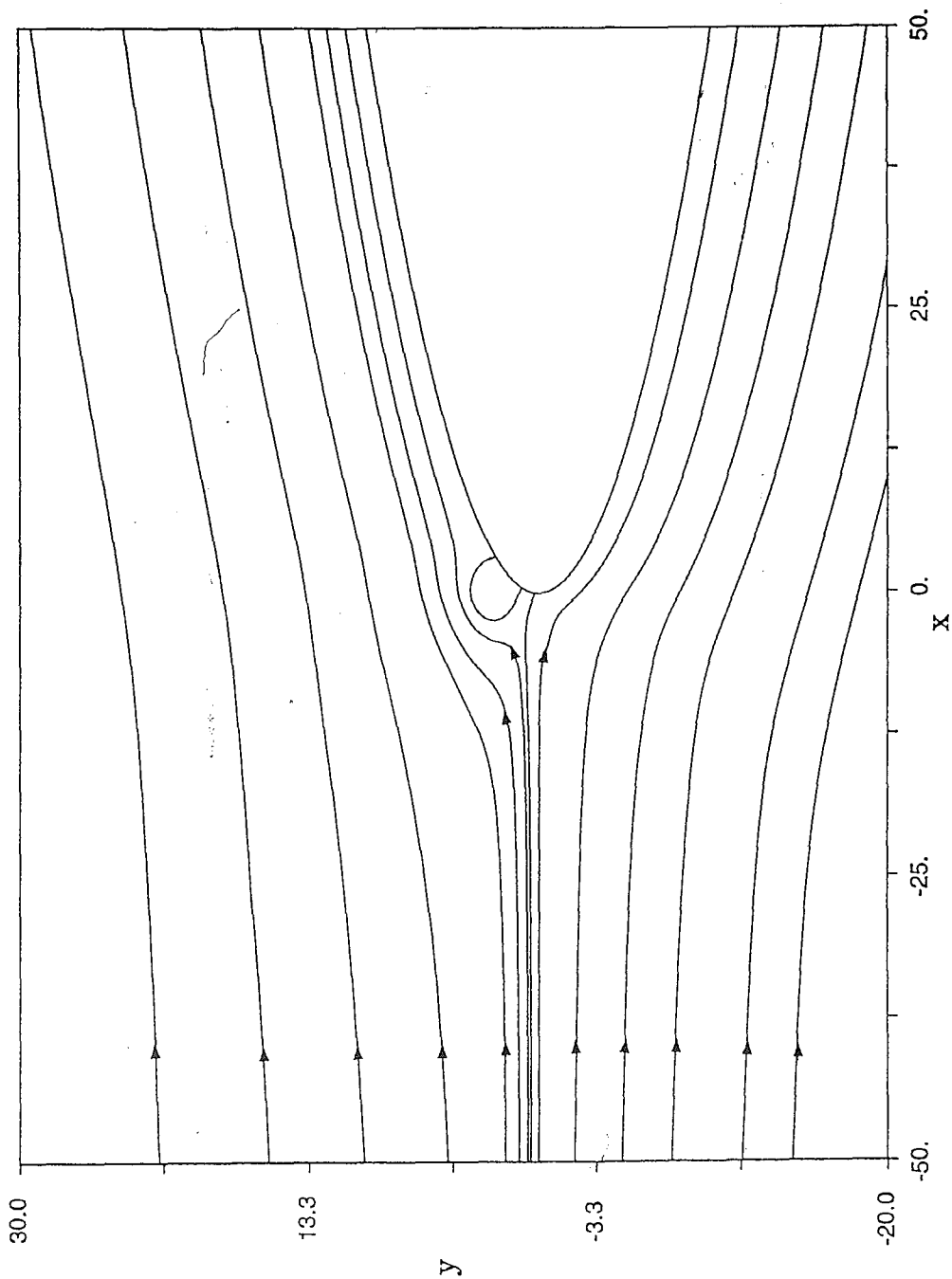

3.28 (e) t = 5.0; A = 0.0

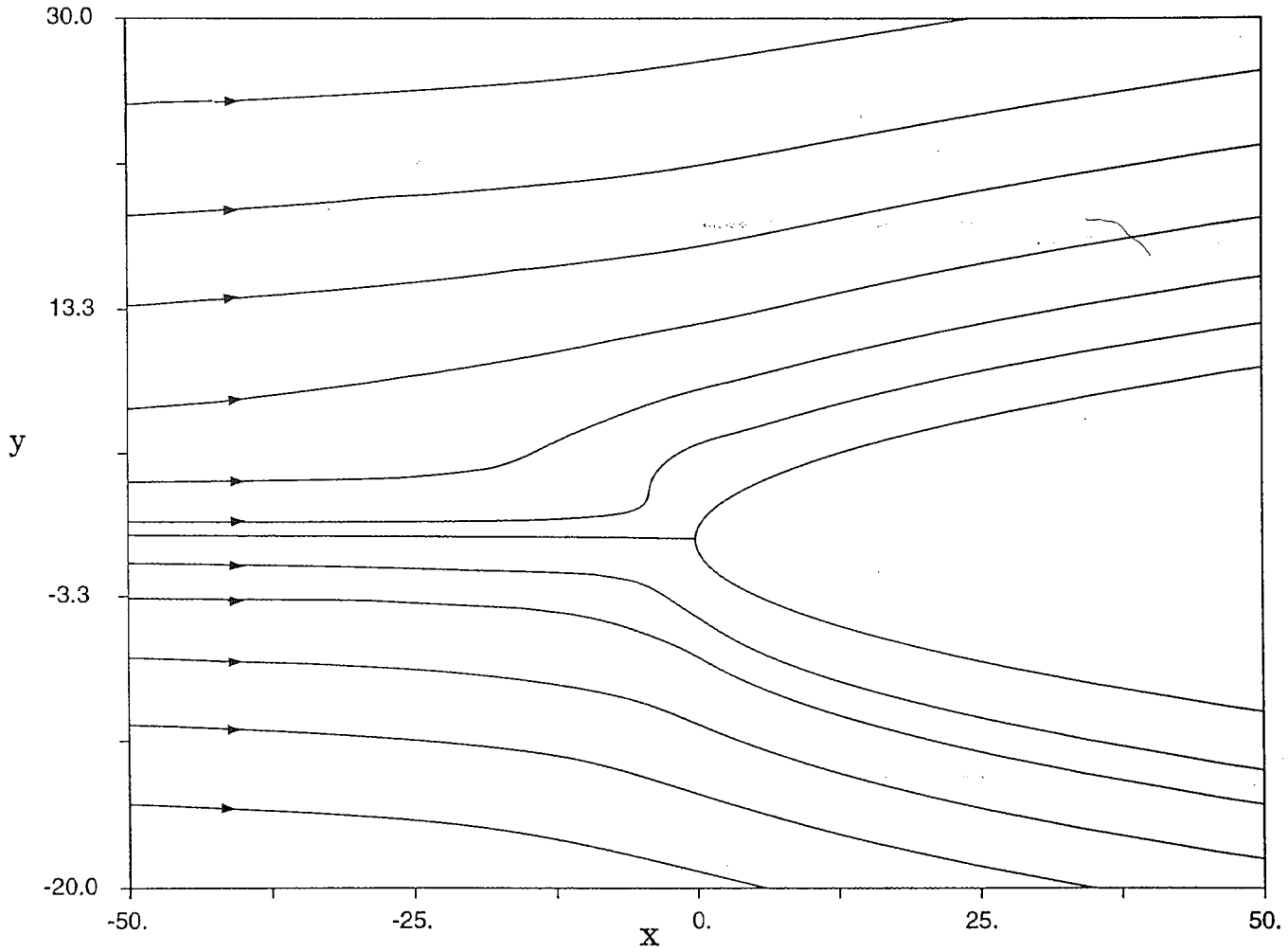

3.28 (f) t = 5.8; A = 0.0

CHAPTER 4
SUMMARY AND CONCLUSIONS

In this study, a model problem for a pitching, thin airfoil in a uniform stream has been developed. For all thin airfoils with rounded leading edges, the problem can be represented locally as flow with varying angle of attack about a parabola. The object of the investigation was to determine the circumstances under which boundary-layer separation would occur in the leading nose region. A combination of Eulerian and Lagrangian formulations were used for the boundary-layer problem. The Eulerian calculation started at $t = 0$ when the airfoil was oriented at zero angle of attack. Calculations were carried out for the angle of attack increasing linearly with time. As boundary-layer separation started to occur, it proved impossible to accurately resolve the flow using the Eulerian method and the calculation was continued using the Lagrangian formulation. Eventually a separation singularity developed in most cases, indicating the onset of a boundary-layer eruption, in which the boundary layer left the surface in an event believed to be the initiation of dynamic stall.

The first case considered was an angle of attack increasing linearly with time with $A(t) = t$; a separation singularity was found to occur at $t = t_s = 4.752$. The structure of the singularity is similar to that found for a parabola at a constant angle of attack (Degani et al, 1994). A recirculation

zone first forms on the upper surface of the parabola and then a sharply-focussed eruptive spike develops. Calculations were carried out for various pitching rates, and a general map determining the time to separation was evaluated for all pitching rates.

In some circumstances, it is desirable to attempt to suppress separation. As a possible means of control, the influence of reversing the pitching rate at a time prior to the occurrence of separation at $t = t_{rev} < t_s$ was considered. The angle of attack was increased linearly with $A(t) = t$ until $t = t_{rev}$, and then it was decreased linearly. The effect of reversing the pitching rate was found to depend on the time of reversal. Two examples considered involved reversal times when a recirculating eddy was present on the upper surface of the airfoil. It was found that in such cases separation still occurs, in different locations near the leading nose but at much the same time. It appears that boundary-layer separation is unavoidable after the recirculation zone of fluid develops. It does not appear to matter how fast or slow the parabola is pitched downward. Therefore, it may be concluded that pitch control is not a viable option for controlling separation once a recirculation region has developed in the boundary layer.

However, reversing the pitching rate before a region of recirculation develops appears more promising. Again, the rate at which the angle of attack is decreased is significant. In some cases, a separation is still encountered but in a considerably weaker form. For a high rate of reversal, it was possible to completely suppress separation.

At this stage, it may be concluded that reversing the pitching rate is not an effective means of suppressing separation. For future work, other means of control should be considered. Past research has shown that a moving wall or suction can be effective in controlling separation. Whether this is effective or not for an airfoil could be answered by investigating the nose region of a parabola where a small region of the surface either moves or utilizes suction. It is anticipated that surface movement, possibly due to a small rotor in the leading edge region or suction, will be able to control or even suppress separation.

REFERENCES

Batchelor, G.K. 1967. An Introduction to Fluid Dynamics. New York: Cambridge University Press, pp. 435-458.

Churchill, Ruel V. & Brown, James Ward. 1990. Complex Variables and Applications. New York: McGraw-Hill Publishing Co., pp. 207-246.

Degani, Ammar T. 1993. FORTRAN Computer Programs for Airfoil at Constant Angle of Attack. Department of Mechanical Engineering and Mechanics, Lehigh University, PA.

Degani, A.T., Li, Q. & Walker, J.D.A. 1994. "Unsteady Separation From the Leading Edge of an Airfoil." AIAA Paper FD-25.3: Conference on Fluid Dynamics, June 22.

Doligalski, T.L., Smith, C.R., & Walker, J.D.A. 1993. "Vortex Interactions With Walls." Annu. Rev. Fluid Mech. Vol. 26, pp. 573-616.

Doligalski, T.L. & Walker, J.D.A. 1984. "The Boundary Layer Induced by a Convected Two-Dimensional Vortex." J. Fluid Mech. Vol. 139, pp. 1-28.

Dyck, V.A., Lawson, J.D. & Smith, J.A. 1984. FORTRAN 77, An Introduction to Structured Problem Solving. Englewood Cliffs, NJ.: Prentice-Hall.

McCroskey, W.J. 1982. "Unsteady Airfoils." Ann. Rev. Fluid Mech. Vol. 14, p.285.

Mizrahi, Abe & Sullivan, Michael. 1990. Calculus & Analytic Geometry. Belmont, CA: Wadsworth Publishing Company.

Owczarek, Jerzy A. 1968. Introduction to Fluid Mechanics. Scranton, PA: International Textbook, pp. 494-500.

Panton, Ronald L. 1984. Incompressible Flow. New York: John Wiley & Sons.

Peridier, V.J. & Walker, J.D.A. 1988. "An Algorithm for Unsteady Flows with Strong Convection." NASA Technical Memorandum 100828, ICOMP-88-5, NASA Lewis Research Center.

Peridier, Vallorie J. 1989. Vortex Induced Boundary-Layer Separation. Ph.D. Dissertation, Lehigh University, PA.

Peridier, Vallorie J., Smith F.T. & Walker, J.D.A. 1991a. "Vortex Induced Boundary-Layer Separation. Part 1. The Unsteady Limit problem $Re \to \infty$." J. Fluid Mech. Vol. 232, pp.99-131.

Peridier, Vallorie J., Smith F.T. & Walker, J.D.A. 1991b. "Vortex Induced Boundary-Layer Separation. Part 2. Unsteady Interacting Boundary-Layer Theory. " J. Fluid Mech. Vol. 232, pp.133-165.

Press, William H., Flannery, Brian P., Teukolsky, Saul A. & Vetterling, William, T. 1989. Numerical Recipes, The Art of Scientific Computing (FORTRAN Version). New York: Cambridge University Press, pp. 77-101.

Ruban, A.I. 1981. "Singular Solution of Boundary-Layer Equations That Can Be Extended Continuously Through a Point of Zero Skin Friction." Izv. Akad. Nauk SSSR, Mekh. Zhidk. Gaza No6, p. 63.

Spiegel, Murray R. 1991. Mathematical Handbook of Formulas and Tables. New York: McGraw-Hill.

Van Dommelen, L.L. & Shen, S.F. 1982. "The Genesis of Separation." Proceedings of Symposium on Numerical and Physical Aspects of Aerodynamic Flow. (ed. T. Cebeci). Long Beach, CA, pp.283-311.

Van Dommelen, L.L. & Shen, S.F. 1980. "The Spontaneous Generation of the Singularity in a Separating Boundary Layer." J. Comp. Phys. Vol 38, pp. 125-140.

Van Dyke, Milton. 1975. Perturbation Methods in Fluid Mechanics. Stanford, CA: The Parabolic Press, pp. 1-76.

Van Dyke, Milton D. 1956. "Second-Order Subsonic Airfoil Theory Including Edge Effects." NACA Report 1274.

Wegener, Peter P. 1991. What Makes Airplanes Fly? New York: Springer-Verlag.

Werle, M.J. & Davis, R.T. 1972. "Incompressible Laminar Boundary Layers on a Parabola at Angle of Attack: A Study of the Separation Point." Trans. ASME, Ser. E, J. Applied Mech. Vol. 39, pp. 7-12.

APPENDIX A
NUMERICAL METHODS

A.1 FACTORED ADI NUMERICAL METHOD

This section is a brief description of the derivations in Peridier & Walker (1988) and Peridier (1989). These sources may be consulted for more details.

An ADI (alternating-direction-implicit) numerical scheme is used in this study to solve the two-dimensional boundary-layer equations. It is based upon the Crank-Nicholson approach and Doligalski & Walker's (1984) "upwind-downwind" differencing method. The latter algorithm replaces the former for the first order spatial derivatives. This produces a totally second order accurate (in time and space) implicit finite differencing scheme that involves the solution of diagonally dominant matrices.

Recall the general form of the boundary-layer equation which holds for both the Eulerian and Lagrangian cases:

$$\frac{\partial U}{\partial t} = P\frac{\partial^2 U}{\partial \xi^2} + Q\frac{\partial^2 U}{\partial \xi \partial \eta} + R\frac{\partial^2 U}{\partial \eta^2} + S\frac{\partial U}{\partial \xi} + T\frac{\partial U}{\partial \eta} + WU + \Gamma \qquad (A.1)$$

where $P \geq 0$, $R \geq 0$. The definition of U in equation (A.1) depends upon the variables used. If the problem is formulated in conventional Eulerian variables, then the general form is

$$U = \frac{\partial \psi}{\partial \eta}, \qquad (A.2)$$

where ψ is the two-dimensional streamfunction. Also, it is found that P=Q=0. Thus, the coefficients (R, S, T, W) in (A.1) are functions of ξ, η, t, U and ψ.

When the problem is cast in Lagrangian variables,

$$U = \frac{\partial s}{\partial t}, \tag{A.3}$$

where s is a particle's streamwise position, and U is the time-rate of change of the particle's streamwise position. Here, the coefficients (P, Q, R, S, T, W) are functions of ξ, η, t, s and U.

The momentum equation (A.1) is evaluated at the average time plane, $\bar{t} = t - \Delta t/2$, using the known values at the previous time plane t^*. This step is necessary to advance the solution for U to the current time plane, $t = t^* + \Delta t$. The averaged quantities are denoted by an overbar ($\bar{}$). For example, the average coefficient $\bar{P}$ is

$$\bar{P} = \frac{1}{2}(P + P^*), \tag{A.4}$$

where P and P^* are the values in the current and previous time planes, respectively. Similarly,

$$\bar{U} = \frac{1}{2}(U + U^*). \tag{A.5}$$

The conventional Crank-Nicholson representation of equation (A.1) is

$$\frac{U - U^*}{\Delta t} = \left(\bar{P}\frac{\partial^2}{\partial \xi^2} + \bar{Q}\frac{\partial^2}{\partial \xi \partial \eta} + \bar{R}\frac{\partial^2}{\partial \eta^2} + \bar{S}\frac{\partial}{\partial \xi} + \bar{T}\frac{\partial}{\partial \eta} + \bar{W}\right)\bar{U} + \bar{\Gamma}, \tag{A.6}$$

which is accurate to $O(\Delta t)^2$.

For the second derivative and cross derivative terms in (A.4), the Crank-Nicholson (central difference) approximations are used to calculate the average values at a typical mesh point (i, j) at $\bar{t}$, i.e.

$$\bar{P}\frac{\partial^2 \bar{U}}{\partial \xi^2} = \frac{\bar{P}_{i,j}}{2(\Delta \xi)^2}\left(U_{i+1,j} - 2U_{i,j} + U_{i-1,j} + U^*_{i+1,j} - 2U^*_{i,j} + U^*_{i-1,j}\right) + O(\Delta \xi)^2, \tag{A.7}$$

$$\bar{Q}\frac{\partial^2 \bar{U}}{\partial\xi\partial\eta} = \frac{\bar{Q}_{i,j}}{8(\Delta\xi)(\Delta\eta)}\,(U_{i+1,j+1}-U_{i+1,j-1}+U_{i-1,j-1}-U_{i-1,j+1} \tag{A.8}$$

$$+U^*_{i+1,j+1}-U^*_{i+1,j-1}+U^*_{i-1,j-1}-U^*_{i-1,j+1}) + O(\Delta\xi\Delta\eta),$$

$$\bar{R}\frac{\partial^2 \bar{U}}{\partial\eta^2} = \frac{\bar{R}_{i,j}}{2(\Delta\eta)^2}\,(U_{i,j+1}-2U_{i,j}+U_{i,j-1}+U^*_{i,j+1}-2U^*_{i,j}+U^*_{i,j-1}) + (\Delta\eta)^2. \tag{A.9}$$

Recall that after the problem is transformed from parabolic to computational coordinates in sections 2.3 and 2.5, the resulting mesh is a rectangular grid. The mesh spacings in the horizontal (ξ) and vertical (η) directions are denoted by $\Delta\xi$ and $\Delta\eta$, respectively.

Figure A.1 (from Peridier & Walker, 1988) shows the averaging path for the Crank-Nicholson method. The spatial distribution consists of a typical mesh point and its four adjacent points in the rectangular grid. The dashed line represents the averaging path between two consecutive time planes and $\bar{U}_{i,j}$ is approximated at the average time $\bar{t}$.

The conventional Crank-Nicholson approximations for the first derivative terms in (A.6) do not necessarily produce a diagonally dominant matrix problem, and the solution may fail to converge. Therefore, the "upwind-downwind" differencing scheme is used instead for the $S\cdot\partial U/\partial\xi$ and $T\cdot\partial U/\partial\eta$ terms. This method is based upon the fact that a second order accurate solution is possible along any averaged path that passes through the central (approximation) point (Peridier & Walker, 1988). For instance, in figure A.2(b), path (d) is used when $\bar{S}_{i,j} \geq 0$ at a typical mesh point. In the current time plane, path (b) intersects the point halfway between points (i,j) and (i+1,j). In the previous time plane, path (b) intersects the midpoint

between points (i,j) and (i-1,j). Likewise for $\bar{S}_{i,j} < 0$, path (e) is the averaging path. Therefore, the upwind-downwind differencing equations for $S \cdot \partial U/\partial \xi$ at a typical mesh point (i,j) at $\bar{t}$ are

$$\bar{S}\frac{\partial \bar{U}}{\partial \xi} = \left\{ \begin{array}{ll} \dfrac{\bar{S}_{i,j}}{2\Delta\xi}\,(U_{i+1,j}-U_{i,j}+U^*_{i,j}-U^*_{i-1,j}), & \bar{S}_{i,j} \geq 0 \\ \\ \dfrac{\bar{S}_{i,j}}{2\Delta\xi}\,(U_{i,j}-U_{i-1,j}+U^*_{i+1,j}-U^*_{i,j}), & \bar{S}_{i,j} < 0 \end{array} \right\} \qquad (A.10)$$

Similarly, figure A.2(a) illustrates the averaging paths for $T \cdot \partial U/\partial \eta$ and

$$\bar{T}\frac{\partial \bar{U}}{\partial \eta} = \left\{ \begin{array}{ll} \dfrac{\bar{T}_{i,j}}{2\Delta\eta}\,(U_{i,j+1}-U_{i,j}+U^*_{i,j}-U^*_{i,j-1}), & \bar{T}_{i,j} \geq 0 \\ \\ \dfrac{\bar{T}_{i,j}}{2\Delta\eta}\,(U_{i,j}-U_{i,j-1}+U^*_{i,j+1}-U^*_{i,j}), & \bar{T}_{i,j} < 0 \end{array} \right\} \qquad (A.11)$$

The generalized equation (A.6) can be factored into two operators, one for each independent spatial variable (ξ,η). The purpose of this factorization is to produce a sequence of tridiagonal matrix problems for lines of constant ξ and η at each time step Δt. Thus, at a typical mesh point (i,j) at $\bar{t}$,

$$\left(1 - \alpha_{i,j}\bar{P}_{i,j}\frac{\partial^2}{\partial\xi^2} - \alpha_{i,j}\bar{S}_{i,j}\frac{\partial}{\partial\xi}\right)\left(1 - \alpha_{i,j}\bar{R}_{i,j}\frac{\partial^2}{\partial\eta^2} - \alpha_{i,j}\bar{T}_{i,j}\frac{\partial}{\partial\eta}\right) U_{i,j} = D_{i,j} \qquad (A.12)$$

where

$$\alpha_{i,j} = \frac{\Delta t}{2 - \bar{W}_{i,j}\cdot\Delta t}, \qquad (A.13)$$

and

$$D_{i,j} = \alpha_{i,j}\left(\bar{P}_{i,j}\frac{\partial^2}{\partial\xi^2} + \bar{R}_{i,j}\frac{\partial^2}{\partial\eta^2} + \bar{S}_{i,j}\frac{\partial}{\partial\xi} + \bar{T}_{i,j}\frac{\partial}{\partial\eta} + \bar{W}_{i,j}\right) U^*_{i,j} \qquad (A.14)$$

$$+ \alpha_{i,j}\bar{Q}_{i,j}\frac{\partial^2}{\partial\xi\partial\eta}\left(U_{i,j} + U^*_{i,j}\right) + \frac{2\alpha_{i,j}}{\Delta t}U^*_{i,j} + 2\alpha_{i,j}\bar{\Gamma}.$$

The term $D_{i,j}$ contains all the known values at the previous time plane (*). It also contains the second order cross derivative for the current and previous time planes because this term is difficult to factorize.

The factorization process is concluded by defining an intermediate dependent variable $\tilde{U}_{i,j}$ yields

$$\tilde{U}_{i,j} = \left(1 - \alpha_{i,j}\bar{P}_{i,j}\frac{\partial^2}{\partial\xi^2} - \alpha_{i,j}\bar{S}_{i,j}\frac{\partial}{\partial\xi}\right)U_{i,j}, \qquad (A.15)$$

and substituting it into (A.12), viz.

$$\left(1 - \alpha_{i,j}\bar{R}_{i,j}\frac{\partial^2}{\partial\eta^2} - \alpha_{i,j}\bar{T}_{i,j}\frac{\partial}{\partial\eta}\right)\tilde{U}_{i,j} = D_{i,j}. \qquad (A.16)$$

Now, two phases of calculation are required for the solution of $U_{i,j}$. First, equation (A.16) is solved by a point by point sweeping of the rectangular mesh along all lines of constant ξ. After each sweep of a line of constant ξ, the non-iterative Thomas algorithm directly solves the tridiagonal matrix problem. This first phase calculates the current values of the intermediate variable $\tilde{U}_{i,j}$ at all internal, spatial mesh points.

Second, a sequence of tridiagonal matrix problems for $U_{i,j}$ is solved by substituting the current approximations of $\tilde{U}_{i,j}$ into the left side of expression (A.15) and sweeping the rectangular mesh along all interior lines of constant η. Again, the Thomas algorithm calculates the current estimates for $U_{i,j}$.

Both phases are part of an implicit (iterative) process. After the

completion of both phases, a convergence check is performed to indicate whether the values of $U_{i,j}$ satisfy the convergence tolerance or whether more iterations are required.

A.2 THOMAS ALGORITHM

The Thomas algorithm is a direct and non-iterative method of solving tridiagonal matrix problems.

The number of mesh points are (M+1) × (N+1), where i=1 to (M+1) and j=1 to (N+1) define the mesh nodes.

Equation (A.16) has the general form

$$b_j\tilde{U}_{i,j+1} + a_j\tilde{U}_{i,j} + c_j\tilde{U}_{i,j-1} = D_{i,j} \quad \text{for j=2 to N,} \tag{A.17}$$

and equation (A.15) has the form

$$b_iU_{i+1,j} + a_iU_{i,j} + c_iU_{i-1,j} = \tilde{U}_{i,j} \quad \text{for i=2 to M.} \tag{A.18}$$

The upper and lower boundary conditions for U are

$$U_{i,1} = 0, \qquad U_{i,N+1} = U_\infty(\xi,t). \tag{A.19}$$

The upper and lower boundary conditions for $\tilde{U}$ are found from equation (A.15). Since the general coefficients a,b,c and d are known (d represents the right side of equation A.17 or A.18), it is possible to define the variables

$$F_{k+1} = \frac{-b_{k+1}}{(a_{k+1}+c_{k+1}F_k)}, \qquad \delta_{k+1} = \frac{(d_{k+1}-c_{k+1}\delta_k)}{(a_{k+1}+c_{k+1}F_k)}, \tag{A.20}$$

where $F_1=0$ and $\delta_1= U_{i,1}$ or $\widetilde{U}_{1,j}$ depending on which phase is being calculated. Then, $U_{i,j}$ or $\widetilde{U}_{i,j}$ is calculated by backward substitution according to

$$U_k = F_n U_{k+1} + \delta_k \quad \text{for k=K, K-1, ...} \tag{A.21}$$

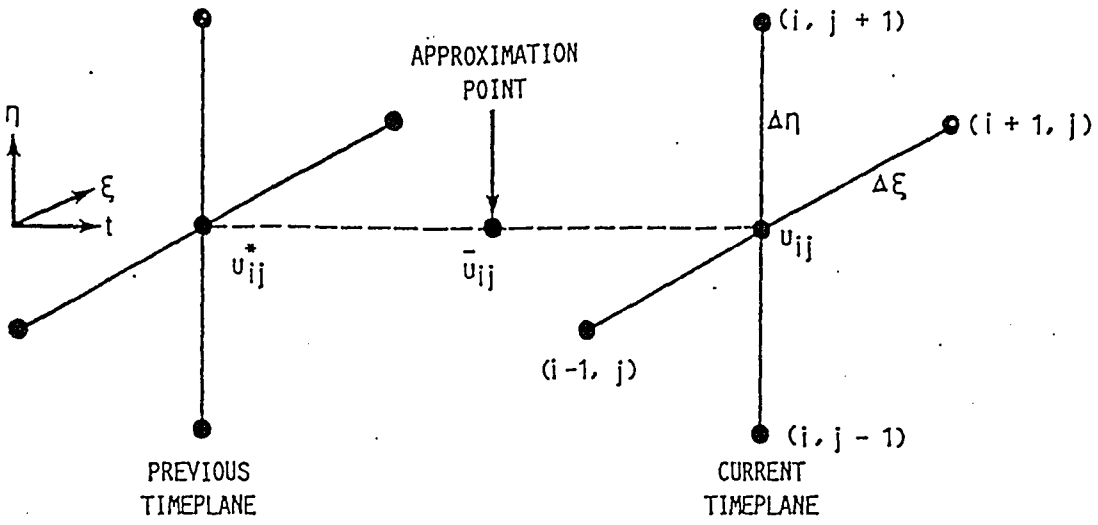

Figure A.1 — Grid structure and notation for conventional Crank-Nicholson method

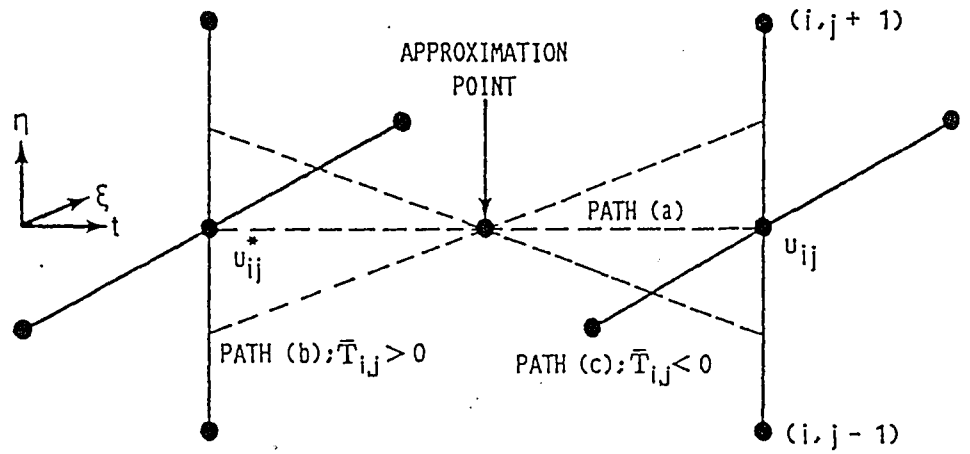

(a) $T\,\partial u/\partial\eta$.

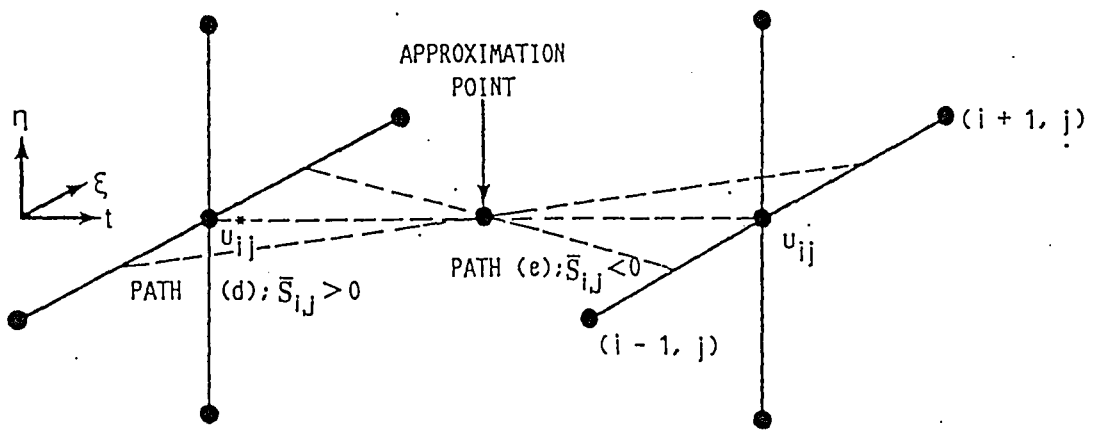

(b) $S\,\partial u/\partial\xi$.

Figure A.2 — Averaging paths for first derivative terms [Peridier et al. (1988)]

APPENDIX B
FORMULATION OF LAGRANGIAN EQUATIONS

This section contains a brief derivation (one that parallels the derivation in Peridier 1989) of the boundary-layer and continuity equations in Lagrangian variables. As derived in section 2.3, these equations in Eulerian variables are, respectively,

$$\frac{\partial u}{\partial t} + u\frac{\partial u}{\partial s} + v\frac{\partial u}{\partial n} = \frac{\partial U_\infty}{\partial t} + \frac{U_\infty}{\sqrt{\xi^2+1}}\frac{\partial U_\infty}{\partial \xi} + \frac{\partial^2 u}{\partial n^2}, \tag{B.1}$$

$$\frac{\partial u}{\partial s} + \frac{\partial v}{\partial n} = 0. \tag{B.2}$$

The position of a fluid particle in Lagrangian variables is found by knowing its initial position and the amount of time elapsed for the particle to travel along its path and reach its current position. The dependent variables are

$$s=s(\chi,\rho,t), \qquad n=n(\chi,\rho,t), \tag{B.3}$$

where the independent variables, χ and ρ, are the initial positions of the fluid particles defined at time $t=t_0$ according to

$$s=s(\chi,\rho,t_0)=\chi, \qquad n=n(\chi,\rho,t_0)=\rho, \tag{B.4}$$

As in the Eulerian case, χ and ρ are also orthogonal curvilinear coordinates.

The left side of equation (B.1) is also known as the material derivative which represents the total acceleration (local and convective) of a fluid particle in Eulerian variables; thus (B.1) becomes

$$\frac{Du}{Dt} = \frac{\partial U_\infty}{\partial t} + \frac{U_\infty}{\sqrt{\xi^2+1}}\frac{\partial U_\infty}{\partial \xi} + \frac{\partial^2 u}{\partial n^2}. \tag{B.5}$$

In Lagrangian variables, the acceleration of a fluid particle is the local acceleration only, i.e.

$$\frac{Du(\chi,\rho,t)}{Dt} = \frac{\partial u}{\partial t}, \tag{B.6}$$

where $u = \partial s/\partial t$ is the time-rate of change of the fluid particle's streamwise position.

The first two terms on the right of (B.1) represent the external pressure gradient that was calculated in section 2.2. The last term is the viscous term and must be transformed into Lagrangian variables.

First, the partial derivatives of the functional relationships (B.3) are

$$\frac{\partial}{\partial s} = \frac{\partial \chi}{\partial s}\frac{\partial}{\partial \chi} + \frac{\partial \rho}{\partial s}\frac{\partial}{\partial \rho}, \qquad \frac{\partial}{\partial n} = \frac{\partial \chi}{\partial n}\frac{\partial}{\partial \chi} + \frac{\partial \rho}{\partial n}\frac{\partial}{\partial \rho}. \tag{B.7}$$

When expressions (B.7) act upon the functions s and n, a system of four linear equations is produced for the four unknown partial derivatives χ_s, χ_n, ρ_s and ρ_n, viz.

$$\frac{\partial}{\partial s}(s) = 1 = \frac{\partial \chi}{\partial s}\frac{\partial s}{\partial \chi} + \frac{\partial \rho}{\partial s}\frac{\partial s}{\partial \rho}, \tag{B.8}$$

$$\frac{\partial}{\partial n}(n) = 1 = \frac{\partial \chi}{\partial n}\frac{\partial n}{\partial \chi} + \frac{\partial \rho}{\partial n}\frac{\partial n}{\partial \rho},$$

$$\frac{\partial}{\partial s}(n) = 0 = \frac{\partial \chi}{\partial s}\frac{\partial n}{\partial \chi} + \frac{\partial \rho}{\partial s}\frac{\partial n}{\partial \rho},$$

$$\frac{\partial}{\partial n}(s) = 0 = \frac{\partial \chi}{\partial n}\frac{\partial s}{\partial \chi} + \frac{\partial \rho}{\partial n}\frac{\partial s}{\partial \rho}.$$

A factor, called the Jacobian, must be introduced for the change of variables. Therefore, to change s and n to χ and ρ, the Jacobian of the transformation (Mizrahi & Sullivan 1990) is

$$J(s,n;\chi,\rho) = \frac{\partial(s,n)}{\partial(\chi,\rho)} = \det\begin{bmatrix} s_\chi & s_\rho \\ n_\chi & n_\rho \end{bmatrix} = \left(\frac{\partial s}{\partial \chi}\frac{\partial n}{\partial \rho} - \frac{\partial s}{\partial \rho}\frac{\partial n}{\partial \chi}\right). \tag{B.9}$$

The solution of the system of linear equations is

$$\left.\begin{aligned} \frac{\partial \chi}{\partial s} &= \frac{1}{J}\frac{\partial n}{\partial \rho}, \qquad \frac{\partial \chi}{\partial n} = -\frac{1}{J}\frac{\partial s}{\partial \rho}, \\ \frac{\partial \rho}{\partial s} &= \frac{1}{J}\frac{\partial n}{\partial \rho}, \qquad \frac{\partial \rho}{\partial s} = -\frac{1}{J}\frac{\partial n}{\partial \chi}. \end{aligned}\right\} \tag{B.10}$$

Thus, the partial derivatives (B.7) become

$$\left.\begin{aligned} \frac{\partial}{\partial s} &= \frac{1}{J}\left(\frac{\partial n}{\partial \rho}\frac{\partial}{\partial \chi} - \frac{\partial n}{\partial \chi}\frac{\partial}{\partial \rho}\right), \\ \frac{\partial}{\partial n} &= \frac{1}{J}\left(\frac{\partial s}{\partial \chi}\frac{\partial}{\partial \rho} - \frac{\partial s}{\partial \rho}\frac{\partial}{\partial \chi}\right). \end{aligned}\right\} \tag{B.11}$$

Now, the substitution of expressions (B.11) into the continuity equation (B.2) yields

$$\frac{1}{J}\cdot\left(\frac{\partial n}{\partial \rho}\frac{\partial u}{\partial \chi} - \frac{\partial n}{\partial \chi}\frac{\partial u}{\partial \rho} + \frac{\partial s}{\partial \chi}\frac{\partial v}{\partial \rho} - \frac{\partial s}{\partial \rho}\frac{\partial v}{\partial \chi}\right) = 0, \tag{B.12}$$

and, in two-dimensional Lagrangian coordinates, the velocities (u,v) are the

time rates of change of an individual fluid particle's position, viz.

$$u = \frac{\partial s}{\partial t}, \qquad v = \frac{\partial n}{\partial t}. \tag{B.13}$$

Substitution of (B.13) into (B.12) results in

$$\frac{1}{J}\frac{\partial}{\partial t}\left(\frac{\partial s}{\partial \chi}\frac{\partial n}{\partial \rho} - \frac{\partial s}{\partial \rho}\frac{\partial n}{\partial \chi}\right) = \frac{1}{J}\frac{\partial J}{\partial t} = 0. \tag{B.14}$$

Expression (B.14) illustrates that the Jacobian is invariant in time. Therefore, using the initial conditions (B.4), the Jacobian is

$$J = 1. \tag{B.15}$$

Now, expressions (B.11) are totally defined and can be substituted into (B.1) to obtain a system of two coupled, unsteady equations in Lagrangian variables according to

$$\left.\begin{aligned} \frac{\partial s}{\partial t} &= u, \\ \frac{\partial u}{\partial t} &= \frac{\partial U_\infty}{\partial t} + \frac{U_\infty}{\sqrt{\xi^2+1}}\frac{\partial U_\infty}{\partial \xi} + \left(\frac{\partial s}{\partial \chi}\frac{\partial}{\partial \rho} - \frac{\partial s}{\partial \rho}\frac{\partial}{\partial \chi}\right)^2 u. \end{aligned}\right\} \tag{B.16}$$

VITA

Michael P. Johnson, son of Paul F. and Judy E. Johnson, was born in Glens Falls, New York on December 10, 1969. He attended the South Glens Falls School District and graduated in 1988 with a Regents Diploma With Honors.

Johnson attended Clarkson University and received his Bachelor of Science degree with Great Distinction in May 1992. He majored in Interdisciplinary Engineering and Management (E&M) and completed a concentration in Mathematics. While at Clarkson, he was a member of the Phi Kappa Phi national honorary society, the Pi Mu Epsilon national mathematics honorary society, and the Sigma Tau Iota E&M honorary society. Also, he received the Presidential and Clarkson Trustees Scholarships and received the Outstanding Junior Award in E&M in 1991.

In the fall of 1992, Johnson commenced graduate studies in the Department of Mechanical Engineering and Mechanics at Lehigh University. He was the recipient of the Packard Fellowship during 1992-1993 and was a teaching assistant for heat transfer courses during 1993-1994. In 1993, he received honorable mention for a fellowship sponsored by the National Science Foundation. He received his Master of Science degree in Mechanical Engineering in May 1994.

END

OF

TITLE